Mesoscopic quantum oscillations of the resistance in the intermediate state of type-I superconductors

Yu. N. Chiang* and O. G. Shevchenko

B. Verkin Institute for Low Temperature Physics and Engineering, National Academy of Sciences of Ukraine, pr. Lenina 47, 61103 Kharkov, Ukraine

Quantum interference effects in the conductance of *SNS* systems formed in type-I superconductors in the intermediate state are investigated. The investigation is extended to the *SNS* system of the intermediate state of indium in a macroscopic hybrid sample with single-crystal copper, for a sample configuration corresponding to a doubly connected "Andreev interferometer." Quantum oscillations of the resistance are detected in ultrapure samples of Pb, Sn, and In of various geometries and are investigated as a function of temperature, or of critical magnetic field, in the normal regions of domains of the intermediate state. It is shown that the nature of the oscillations observed is analogous to that of the Aharonov–Bohm dissipative oscillations for the ballistic trajectories of coherent excitations near an *NS* boundary. © *2001 American Institute of Physics.* [DOI: 10.1063/1.1430842]

1. INTRODUCTION

Since the discovery of an unusual increase in the resistance of normal conductors upon the appearance of an *NS* boundary,[1] a finding which pointed to the need for a deeper understanding of the properties of systems with *NS* boundaries, the study of the unconventional behavior of the electron transport in such systems has taken on a broader scope, and that has led and continues to lead to the acquisition of fundamentally new information about the role of coherent excitations in *NS* systems.[2]

It is known that the early experiments detecting the phase-coherent contribution of quasiparticles to the kinetic properties of normal metals for $\omega\tau \ll 1$ (ω is the cyclotron frequency in the magnetic field, and τ is the relaxation time) were done on samples that did not contain *NS* boundaries. In that situation this contribution, due solely to the mechanism of weak localization of electrons, is manifested as a small quantum interference correction to the diffusional contribution.[3] Nevertheless, the existence of coherent transport under those conditions was proved by the observation of quantum interference oscillations in the field of the magnetic vector potential for metallic samples with a doubly connected geometry, which selected for transport along closed self-intersecting trajectories whose coherent character was manifested in oscillations.[4,5]

In systems with *NS* boundaries the contribution of the coherent transport in the normal metal can turn out to be dominant, since it arises in a natural way (and is independent of the probability of realization of trajectories of a special form) as a result of Andreev reflection. This circumstance to a certain extent relaxes the requirements on the size and geometry of the samples for investigating this contribution. For example, it makes it realistic to do experiments on the study of quantum interference effects in the normal near-interfacial regions of *NS* systems on the scale of the elastic mean free path of the electrons, i.e., in the poorly studied "clean" limit of three-dimensional transport, which is pertinent to many

fundamental theoretical treatments. However, the most widely studied case is that of coherent transport in the dirty limit (e.g., corresponding to the situation in mesoscopic samples with an elastic mean free path of the order of a fraction of a micron) or in a non-three-dimensional ballistic regime (in microcontacts, two-dimensional systems, etc.).

In this paper we present research results on quantum interference effects due to the dissipative transport of coherent excitations in *NS* systems in the clean limit and under conditions such that there is an insignificant contribution from the mechanisms of decoherence due to inelastic scattering.

In pure metals at temperatures for which scattering occurs mainly on elastic centers (below 4 K), the spatial scale over which conditions of the clean limit can be realized is macroscopically large, corresponding to the macroscopic values of the elastic mean free paths of the electrons. Because of this, the use of pure metals in *NS* structures is one of the most accessible means of realizing conditions for the experimental study of coherent transport in the clean limit. The first studies of three-dimensional phase-coherent transport at distances from the *NS* boundary of the order of the macroscopic elastic mean free path of the electrons ($\sim 100\,\mu$m) revealed a number of previously unknown features in the scattering of coherent excitations in metals interfacing with a superconductor.[6–9] In particular, it was confirmed that, as predicted by the theory,[10,11] enhancement of dissipation can occur near the boundary in an *N* layer with a thickness of the order of the thermal coherence length,[7] and a resistive contribution, oscillatory with respect to the magnetic field, from coherent excitations in the *NS* structure of the intermediate state of superconductors, is also observed.[9]

In this paper we enlarge the group of superconductors whose critical temperatures permit investigation of the aforementioned effects in the *NS* structure of the intermediate state at helium temperatures. We present experimental results on the observation of oscillations of the resistance with re-

spect to temperature, which corresponds to the value of the critical magnetic field in the normal regions of the *NS* structure of the intermediate state, in ultrapure samples of the type-I superconductors Pb, Sn, and In, with an elastic mean free path of the electrons of the order of 0.1 mm, for three radically different configurations of the samples. This value of the mean free path, which is greater than the dimensions of the normal regions of the structure and is comparable to the distance between probes, ensured a clean-limit transport regime within the boundaries of the measuring probes. We show that the nature of the observed oscillations can be explained by the existence, in these regions, of a closed (impurity–*NS* boundary) dissipative coherent trajectory of a certain length, the extremal value of which is determined by a criterion of coherence that depends on the value of the magnetic field.

2. SAMPLES AND EXPERIMENT

The objects of study were *NS* structures arising at the temperature of the transition of the type-I superconductors to an intermediate state in the presence of a magnetic field, either an external field or the self-field of the measuring current. The temperature dependence of the potential difference in slabs of pure lead, across a neck of pure tin, and in a doubly connected hybrid system with a normal metal (copper) and an indium slab, was investigated at constant measuring currents. The geometry of the samples and the position of the potential probes are shown schematically in Fig. 1.

The lead slabs (Fig. 1a), rolled from a pure material, had a length (along x) $L=3$ mm, a width (along y) $W=0.23$–1.5 mm, and a thickness (along z) $t\approx 20\,\mu$m. The distance between the measuring probes a and b, mounted along x in the middle part of the slab, was $L_m\approx 250\,\mu$m. The samples were placed in a transversely oriented external magnetic field B_e, which was applied along $[z]$ at values of the induction equal to 520 and 550 G and along $[-z]$ at 480 G.

The tin neck (Fig. 1b) was prepared by touching a copper tip having a curvature of 50 μm to a massive drop of pure molten tin and had final dimensions not larger than 20 μm in diameter and around 50 μm in length, with a distance between measuring probes $L_m\approx 100\,\mu$m. The potential probe b was soldered to the edge of the neck on the side with the tin mass, while probe a was soldered to the copper at a distance of approximately 50 μm from the other edge of the neck. The intermediate state of the tin neck was brought on by the self-magnetic field of the measuring current I. Its value at the surface of the neck was around 100 G at $I\approx 1$ A.

The configuration of the hybrid Cu–In sample is shown in Fig. 1c. A rolled indium slab with dimensions $L\times W\times t = 1.5$ mm $\times 0.5$ mm $\times 50\,\mu$m was soldered at its ends to one of the faces of a copper single crystal and was separated from this face by an insulating spacer around 70 μm thick. The potential probe a was mounted on the copper and probe b on the In slab, at distances from the soldering sites $l_1 = l_2\approx 0.6L$ and $l_3 = l_4\approx 0.4L$. Thus the indium slab and a part (of length L) of the copper single crystal formed a doubly connected hybrid *SNS* system acting as an Andreev interferometer with "strong" coupling (with a transmittance at
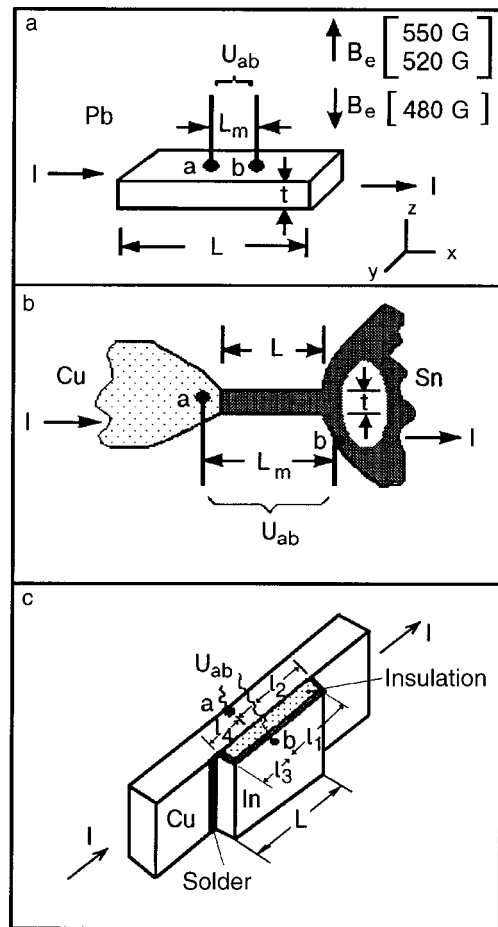

FIG. 1. Configuration of the samples and the position of the potential probes: a—lead slab; b—tin neck; c—doubly connected copper–indium system. See text for explanation.

the end boundaries close to 1). The length L was chosen so that it did not exceed the phase coherence length in the copper. Of the interesting properties of such an interferometer in this paper we shall address only those that are observed in the small self-magnetic field $B_I\approx 5$ G of a measuring current $I=0.7$ A.

In all the systems studied the initial stocks of the metals in the normal state had a ratio of resistances at room and helium temperatures *RRR* not less than 10^4, which corresponds to an average bulk elastic mean free path $l_{el} \sim 100\,\mu$m. In comparison with this value the effective elastic mean free path in the samples studied had decreased by not more than a factor of two in the Pb and In slabs and by an order of magnitude in the Sn neck; these findings agree with estimates taking size and magnetoresistance effects into account.

In the normal state the resistance of a layer of metal with $l_{el}\sim 100\,\mu$m and a volume of the order of l_{el}^3 lies in the range 10^{-8}–$10^{-9}\,\Omega$. For resolution of mesoscopic resistive effects in such a layer at reasonable values of the measuring current ($\lesssim 1$ A) it is necessary to measure the potential difference U with a resolution of $\delta U = 10^{-11}$–10^{-12} V or better. In the experiment this requirement was met by using a null method of measuring the potential differences with the use of a thermomagnetic superconducting modulator[12] with an enhanced sensitivity of $\delta U \sim 5\times 10^{-13}$ V. It was taken into account

that the deviation of the potential difference ΔU from the (monotonic) mean $\bar{U}$ can be taken seriously only in that region of temperatures where the maximum relative deviation $\Delta U_{max}/\bar{U}(T)$ is at least an order of magnitude greater than the measurement error $\delta_m = \delta U/U(T) + \delta_\Sigma$. Here $\delta U/U$ and δ_Σ are, respectively, the relative errors of measurement of the potential differences and of all the remaining parameters (temperature, currents, and values of the magnetic field). Since the ratio of $\delta U/U$ to δ_Σ depends on temperature, the condition for reliable identification of the deviations ΔU as a manifestation of some effect which is regular in temperature can be satisfied only in limited temperature intervals: below about 3 K for the Pb slabs, and below 3.5 K for the Sn neck and the system with In. Indeed, for $I = 1$ A we have for a lead slab:

at 3 K

$\Delta U_{max}/\bar{U}(T) = 2\%$; $\delta_m \approx \delta U/U(T) \approx 0.2\%$;

$\delta_\Sigma \approx 0.03\%$; $\bar{U} = 5.87 \times 10^{-8}$ V;

at 2 K

$\Delta U_{max}/\bar{U}(T) = 200\%$; $\delta_m \approx \delta U/U(T) \approx 10\%$;

$\delta_\Sigma \ll \delta_m$; $\bar{U} = 3.24 \times 10^{-10}$ V;

For a tin neck:

at 3.5 K

$\Delta U_{max}/\bar{U}(T) = 0.1\%$; $\delta_m \leq 0.03\%$;

$\delta_\Sigma = \delta U/U(T) \approx 0.01\%$; $\bar{U} = 4.3402 \times 10^{-6}$ V;

at 2 K

$\Delta U_{max}/\bar{U}(T) = 1\%$; $\delta_m \approx \delta_\Sigma \approx 0.1\%$; $\delta U/U(T) \approx 0.01\%$;

$\bar{U} = 4.0029 \times 10^{-6}$ V.

We see that it is only in the temperature intervals considered that the condition $\Delta U_{max}/\bar{U}(T) \gtrsim 10\delta_m$ is satisfied, and it is only in those temperature intervals that it is meaningful to discuss the deviations of ΔU from $\bar{U}$, which are (at least) greater than $2\delta_m$ there. We will not consider the deviations of ΔU for the lead slabs at higher temperatures, since $\Delta U_{max}/\bar{U}(T) \sim \delta_m \sim \delta_\Sigma$ in the interval 3–4.2 K.

3. EXPERIMENTAL RESULTS

Figure 2 shows the behavior of the temperature derivative of the current-normalized potential difference, $d[U(T)/I]/dT \equiv dR(T)/dT$, for one of the Pb slabs ($W = 0.23$ mm) when the temperature is an appreciable distance from the point of transition of Pb to the superconducting state; the curves indicate the existence of an oscillatory component. We do not show the temperature dependence of $U(T)/I$ for the Pb samples, since it does not reflect the presence of resistive anomalies ΔU because of the large difference between ΔU and $\bar{U}$.

The $U(T)/I$ curve for the Sn neck, shown in Fig. 3, does reflect these anomalies, because of the smaller difference between ΔU and $\bar{U}(T)$.

Although for the hybrid Cu–In sample, as for the Pb samples, the oscillatory anomaly cannot be discerned against the background of the total temperature dependence of $U(T)/I$, in view of the nonstandard form of the latter, which is due to the special arrangement of the measuring probes (Fig. 1c), we show a complete plot of this dependence in Fig. 4. The curve spans both temperature intervals: before and after the formation of the *NS* system (respectively above and
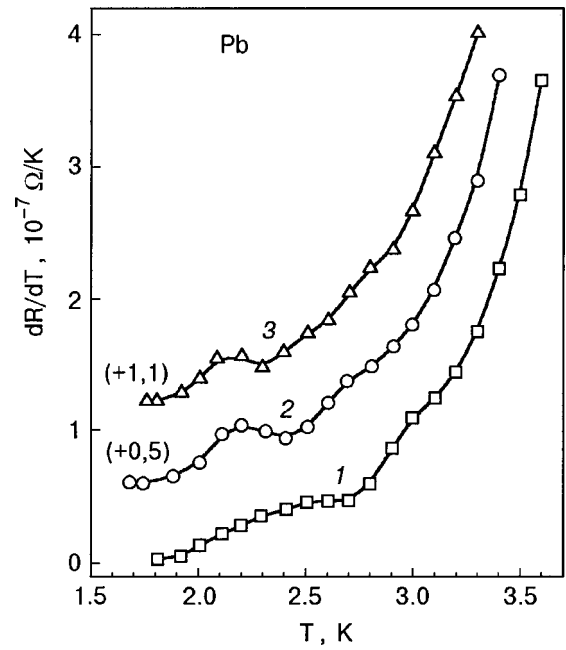

FIG. 2. Temperature derivative of the effective resistance $R = U(T)/I$ of a lead slab in the intermediate state in an external magnetic field $B_e = 480$ (*1*), 520 (*2*), and 550 G (*3*). Curves *2* and *3* have been shifted along the vertical axis relative to curve *1*.

below the critical temperature of In, $T_c^{In} \approx 3.4$ K). The form of the curve, which seems unusual at first glance, actually does not contain anything out of the ordinary and is due entirely to the choice of the arrangement for mounting the probes for measuring the potential difference, in a geometry in which the Cu and In are connected in parallel. One can easily see this by solving the corresponding system of Kirchhoff's equations for the voltage across probes mounted at points a and b in Fig. 1c, with coordinates l_2, l_4 and l_1, l_3. The solution has the form
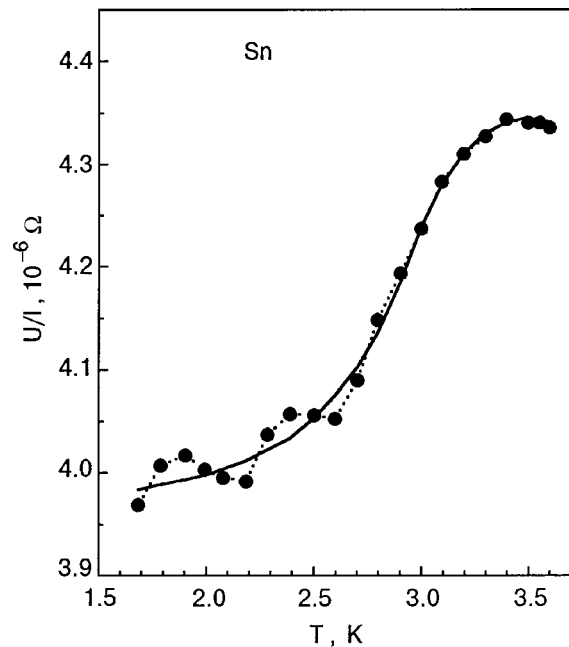

FIG. 3. Temperature dependence of the effective resistance $R = U(T)/I$ for the tin neck in the self-magnetic field of the measuring current $I = 1$ A.
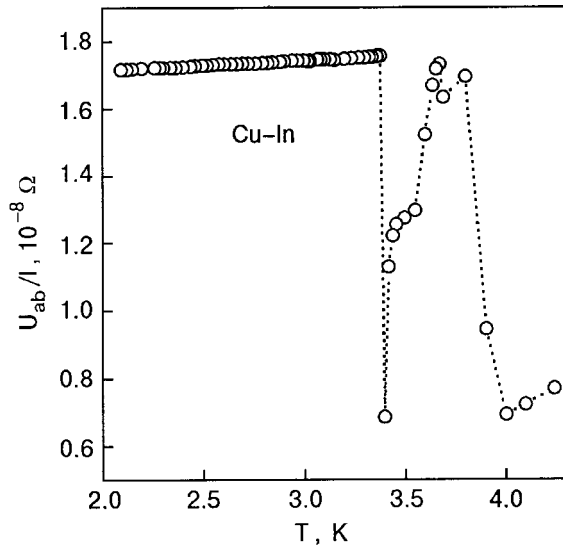
FIG. 4. Temperature dependence of the effective resistance $U(T)/I$ for the Cu–In hybrid system.

FIG. 5. Temperature dependence of the effective resistance $U(T)/I$ for the Cu–In hybrid system at temperatures below T_c^{In} in an enlarged scale.

$$U_{ab}/I = \frac{\alpha R_{Cu}^2 - (\beta - \gamma)R_{Cu}R_{In}}{R_{Cu} + R_{In}}; \qquad (1)$$

$$\alpha = l_2 l_4/(l_2 + l_4)^2; \quad \beta = l_2 l_3/(l_1 + l_3)(l_2 + l_4);$$

$$\gamma = l_1 l_4/(l_1 + l_3)(l_2 + l_4).$$

Here we have taken into account that, according to Matthiessen's rule, the total resistance R of the metal can be written as the sum of the residual resistance R^{el} and a part with a power-law dependence on temperature:

$$R_{Cu} = R_{Cu}^{el} + C_{Cu}T^m; \quad R_{In} = R_{In}^{el} + C_{In}T^n.$$

Expression (1) describes precisely the nonmonotonic behavior of the curve in Fig. 4 under the inequalities $R_{Cu}^{el} < R_{In}^{el}$ and $m > n$, which held in the experiment as a result of the difference in the cross sections and purity of the Cu and In. Analysis of the part of the curve in the NN state of the system is rather trivial, although it might be of some interest. However, that part of the curve is not relevant to the problem addressed in this paper.

In the limit $R_{In} \ll R_{Cu}$, corresponding to an SNS configuration of the system, expression (1) goes over to

$$|U_{ab}|/I = R_{Cu}^{el} + \Delta R_{Cu} - \Delta R_{In}, \qquad (2)$$

where ΔR_{Cu} and ΔR_{In} are the effects we are seeking. If they exist, then, in accordance with (2), they should appear additively.

This leads to some characteristic features of the method of measuring the potential difference in a doubly connected NS system, employed in the case of the Cu–In sample. The chosen arrangement of the probes confers the following advantages: first, it permits simultaneous observation of the temperature dependence of the conductance of both metals in the normal state; second, it enables one to clearly identify the point in temperature at which the transition of the system from the NN to the SNS state occurs; and, most importantly, using a single pair of probes, one in each arm, one can study the anomalous low-temperature resistive effects in both the superconductor and in the normal metal at the same time,
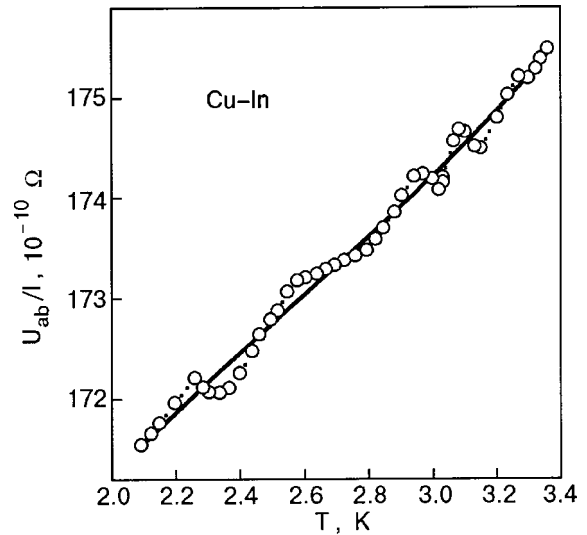
realizing, in particular, either a diffusive or a ballistic regime of electron transport in the normal metal, depending on the position of the probe on it (the values of l_2 and l_4 in Fig. 1c). Here we describe an experiment in which the position of the probe a corresponds to the first of these regimes, with $l_2, l_4 \gg l_{Cu}^{el}$.

The oscillatory temperature dependence of $U(T)/I$ below T_c^{In} is shown separately on an enlarged scale in Fig. 5.

The data presented in Figs. 2, 3, and 5 indicate that in a certain temperature interval the measured potential difference $U(T)$ for all the samples has an oscillatory component, which indicates that the dissipation is of an oscillatory character. The fact that the accuracy of the measurements on Sn and In samples permits resolution of the oscillations even at temperatures above the superconducting transition point but that none were observed allows us to conclude with certainty that the appearance of oscillations is directly due to a transition of the superconductors to an intermediate state.

Figures 6, 7, and 8 show the oscillatory parts of the current-normalized potential difference, $(U - \bar{U}_{mon})/I$ (we will refer to these as U oscillations), obtained by subtracting the corresponding mean monotonic part for each of the samples. We note that for samples with probes mounted directly on the superconductor (the Pb slabs) the monotonic part does not contain a "residual resistance," whereas for samples with one of the potential probes placed on the normal metal the monotonic part of the resistance does contain such a residual component. A comparison of the temperature behavior of the U oscillations and the corresponding monotonic parts permits the conclusion that the oscillations and the temperature-dependent component of the monotonic part are of different natures. While the amplitude of the oscillations $\Delta U_{osc}/I$ for all the samples is weakly temperature dependent (except in the immediate vicinity of the point where the intermediate state arises), the temperature-dependent components of the monotonic parts vary independently over wide limits (not less than two orders of magnitude in the temperature interval in which the oscillations are exhibited). The amplitude of the oscillations in the Sn neck are an order
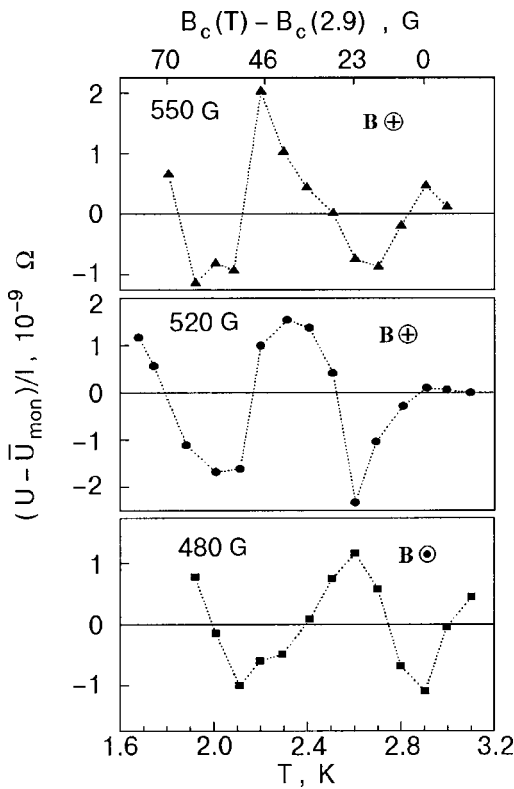
FIG. 6. Oscillatory part $(U-\bar{U}_{mon})/I$ of the effective resistance of a Pb slab in the intermediate state in an external magnetic field $B_e=480$, 520, and 550 G, as a function of temperature. At the top is the corresponding scale of the critical magnetic field.

of magnitude higher, and that in the Cu–In system an order of magnitude lower, than in the Pb slab. The character of the oscillations in the Pb slab for different B_e (Fig. 6) indicates that the phase φ of the oscillations depends on the magnitude and direction of the external magnetic field: in a field of 480 G the phase of the oscillations is shifted relative to the phase
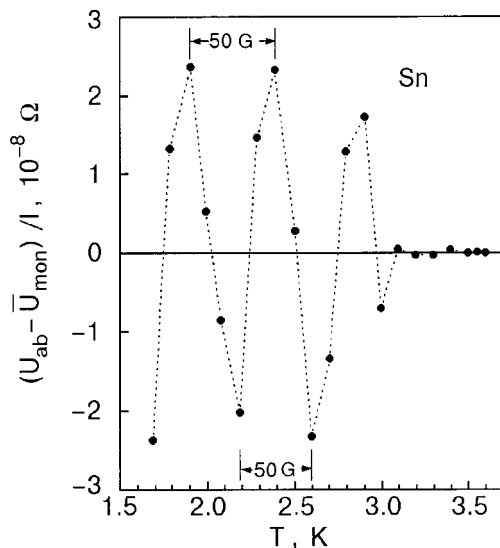

FIG. 7. Oscillatory part $(U-\bar{U}_{mon})/I$ of the effective resistance of the tin neck in the intermediate state in the magnetic field of the measuring current $I=1$ A, as a function of temperature. The period of the oscillations is indicated in units of the critical magnetic field.
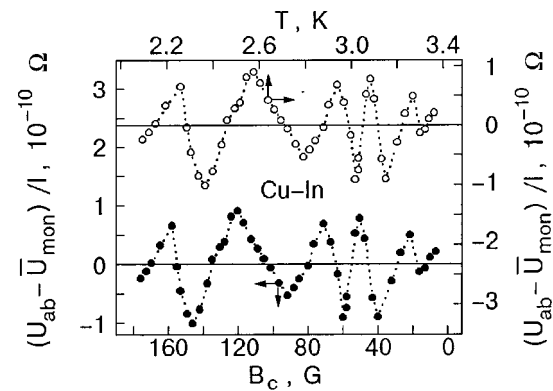

FIG. 8. U oscillations for the doubly connected Cu–In system as a function of temperature (upper curve) and of the critical magnetic field (lower curve) at temperatures below T_c^{In} in the self-magnetic field (~ 5 G) of the measuring current.

in a 550 G field by approximately π, while the phases in fields of 520 and 550 G coincide.

4. DISCUSSION OF THE RESULTS

4.1. Theory

It is known that in the intermediate state of a type-I superconductor in a magnetic field, a laminar domain structure arises, with alternating normal and superconducting regions. In normal regions of this structure the magnetic field is always equal to the critical field of the superconductor, $B_c(T)\cong B_c(0)\{1-[T/T_c(0)]^2\}$, independently of the value of the external field B_e (Ref. 13). Let us use this expression to construct the scales of the critical fields for Pb and In in the temperature regions of the U oscillations (taking the values of $B_c(0)$ and $T_c(0)$ from Ref. 14) and consider the oscillations in terms of the new coordinates (Figs. 6 and 8). For the Sn sample (Fig. 7) instead of the scales of the critical fields we show the scale of variations of the critical field at several characteristic points. Let us make it clear that the difference of the absolute values of the critical field Δ_{B_c} for any pair of points separated by one oscillation period will vary only slightly as the value of the critical field changes considerably over a range of one or two oscillation periods (for the Pb and Sn samples). This is characteristic of a functional dependence of the phase of the oscillations on the field rather than on the inverse field. This can be seen particularly well in the case of a large number of oscillation periods and a large scale of variation of the critical field, as for the Cu–In sample, for which the oscillations are shown in Fig. 9 both as a function of the field itself and as a function of the inverse field.

Thus the period of the observed resistance oscillations is directly related to the value of the critical magnetic field, and the oscillations themselves, showing no connection with the geometry of the samples, appear only after the transition of a simply connected superconductor or of a superconductor in a closed hybrid system to the superconducting state. All of these facts, and also the very existence of resistance oscillations, indicate that after such a transition a laminar SNS domain structure of the intermediate state is formed, the normal regions of which would be a likely place to look for the mechanism responsible for the dissipative oscillations. As
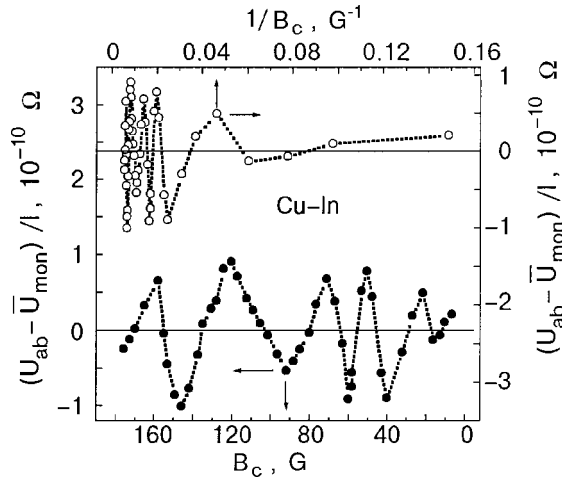
FIG. 9. Oscillations of the effective resistance of the Cu–In system as a function of the direct (lower curve) and inverse (upper curve) critical magnetic field at temperatures below T_c^{In}.
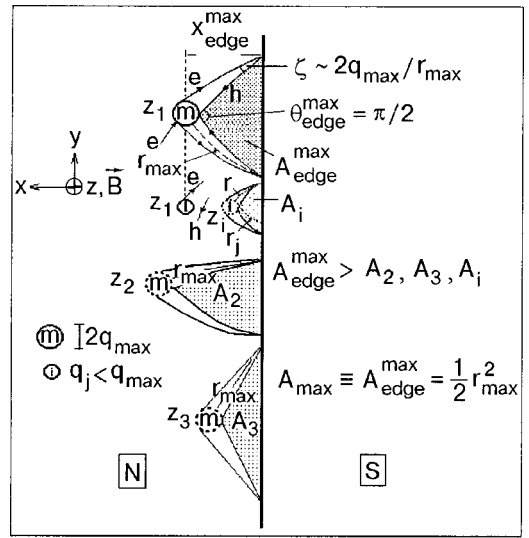

FIG. 10. The criterion of coherent interaction of an electron e and an Andreev hole h with the same elastic scattering center (expression (3) in the text) establishes a distribution of areas A of quantization of the flux of the magnetic vector potential. The maximum admissible area A_{edge}^{max}, bounded by ballistic trajectories passing through the imparities m of maximum cross section $\sim q_{max}^2$ at the positions $[x_{edge}^{max}, y, z]$ for $\theta_{edge}^{max} = \pi/2$ is selected.

will be shown below, the conditions for the appearance of this mechanism in all of the samples correspond to the "clean" limit, i.e., the ballistic transport situation, for which the elastic mean free path l_{el} is greater than or comparable to the size d_N of the normal region.

Having just this situation in mind, we propose below a quasiclassical mechanism for describing the observed U oscillations in the normal regions of the domains of the intermediate state.

The fact that the fields at which the oscillations occur are small and the characteristic features of the oscillations suggest that the origin of the observed oscillations lies in a quantum-interference mechanism of interaction between the coherent excitations and the elastic scattering centers of the normal regions of the domains of the NS structure of the intermediate state. Indeed, only one type of U oscillations is known in which the phase varies directly with the magnetic field while the amplitude depends relatively weakly on temperature. These are oscillations due to the interference of coherent excitations having a direction of motion counter to the magnetic vector potential on closed dissipative trajectories of a rigid configuration.[15,16] Near an NS boundary the largest contribution should be from impurity–boundary ballistic trajectories containing elastic scattering centers, in a normal layer with a thickness of the order of the thermal coherence length $\lambda_T \approx \hbar v_F / k_B T$ (v_F is the Fermi velocity, and k_B is Boltzmann's constant) for $l_{el} \gg \lambda_T$, i.e., at distance from the boundary such that the e- and h-type excitations with energy $\varepsilon \sim k_B T < \Delta_0$ (Δ_0 is the energy gap in the superconductor) can still interact simultaneously with the same impurity (Fig. 10). As we know, on the given trajectories elastic scattering of coherent excitations will lead to an almost twofold increase in the cross section σ for scattering on an impurity,[10] while the change in the conditions of interference of coherent excitations, as might be supposed, will lead to oscillations of the corresponding resistive contribution.

It is not hard to understand that the distribution of lengths of the ballistic coherent trajectories with impurities in the thermal layer is nonuniform. Indeed, upon Andreev reflection the momentum **p** acquires an additional part $\Delta \mathbf{p}$

$= 2(\varepsilon/v_F)\mathbf{n}$ (where $\mathbf{n}$ is a directional unit vector, and ε is the excitation energy measured from the Fermi energy ε_F),[17] so that there is an angular divergence between the directions of the momenta of the e excitation and the h excitation corresponding to it at the point of reflection at the NS boundary; this divergence is $\zeta \sim dp/p_F$, with a lower bound on dp set by the indeterminacy of the momentum, $\Delta p \sim (h/\lambda_\varepsilon)$, $\lambda_\varepsilon = \hbar v_F / \varepsilon$ (λ_ε is the coherence length). It follows that the length of the trajectories under consideration in the thermal layer depends on σ, being the same for trajectories with impurities of equal cross section. In the absence of magnetic field the distribution of lengths does not play a role, and upon averaging over all impurities the region selected by the thermal coherence length turns out to be the entire layer of normal metal, with a decreased conductance on the whole.[10,18] In a magnetic field, however, the features of this distribution should be manifested immediately (including in the self-magnetic field of the measuring current). The reason, of course, is that in the presence of a magnetic vector potential the main role in the change of phase of the wave functions is played not so much by the length of the closed trajectory as by a quantity related to the magnetic flux Φ (Ref. 15), i.e., the area bounded by the trajectory, and, accordingly, it is not the length distribution but the more highly differentiated area distribution that is important. The aforementioned angular divergence ζ of the momenta of the e and h excitations in a magnetic field is additionally enhanced by the Larmor divergence, which alters the ballistic criterion of coherence. An elementary calculation shows that the distance r from an impurity to the most remote point on the boundary at which the particle after Andreev reflection can still return to the same impurity in a magnetic field under the stated conditions of angular divergence of the e and h excitations decreases to a value

$$r = 2\sqrt{qR_L(B_c(T))}. \qquad (3)$$

Here $q=\sqrt{\sigma}$; $R_L=|cp_\perp/eB_c|$ is the Larmor radius, and c is the speed of light.

Thus for each impurity in the plane $z=$ const the magnetic field selects a finite region of coherent e and h trajectories originating at points of Andreev reflection at the NS boundary and terminating at an impurity. The size of this region is bounded by the position of the two extreme points of reflection, the distance of which from the impurity is specified by criterion (3). Figure 10 shows an example of coherent trajectory regions of different area for impurities of identical cross section at the positions $z_{1,2,3}$. Because the cross sections of the impurities are identical, so is the length of the extreme trajectories determined by criterion (3). Also shown is one of the regions bounded by an extreme coherent trajectory of shorter length, corresponding to impurities of smaller cross section at the positions z_i.

As we know, because of the presence of quantum-mechanically dependent (coherent) excitations on the dissipative trajectories, the total scattering amplitude $|f_e+f_h|^2$ ($f_{e,h}$ are the scattering amplitudes) acquires an interference correction $2\,\mathrm{Re}(f_e f_h^*)$, which determines the interference correction to the conductance, and the change of the phase of the wave functions on these trajectories leads to oscillations of this correction with respect to the parameter responsible for the change of phase.[3,10,15,16]

The total change of the phase φ_j of the wave functions on closed superconducting dissipative ballistic trajectories of length $\Lambda_j=2r_j$ in a magnetic field B with allowance for both types of excitations, with energy $E=eU$, is given by the expression[10,11]

$$\varphi_j=\varphi_e+\varphi_h=2\,\pi\left[\frac{1}{\pi}\frac{E\Lambda_j}{\hbar v_F}+\frac{BA_j(x,r_j)}{\Phi_0/2}\right], \qquad (4)$$

where

$$A_j(x,r_j)=x\sqrt{r_j^2-x^2}=\frac{1}{2}r_j^2\sin\theta$$

is the area bounded by the coherent trajectory, with a vertex angle θ in the z plane passing through the impurity, which has coordinates $[x,y,z]$ (see Fig. 10); $\Phi_0=hc/e=4.14\times10^{-7}\,\mathrm{G\cdot cm^2}$.

The contribution of the first term can be neglected, since at the characteristic values of the potential difference for our experiment, $U\leqslant10^{-8}$ V, it does not exceed 10^{-5} of a complete period of variation of the phase in the temperature interval in which several oscillation periods are observed in the experiment. Consequently, the behavior of the interference correction to the scattering amplitude in the interval of changes of the magnetic flux $\Delta\Phi>\Phi_0/2$ for any of the coherent trajectories of length $\Lambda_j\leqslant2r$ (see Fig. 10) will depend mainly on the change of the second term. The latter also governs the behavior of the interference contribution to the scattering cross section and to the resistance, ΔR_j:[3,10,15,16]

$$\Delta R_j\sim\cos\left(2\,\pi\frac{\Phi_j}{\Phi_0/2}\right)-\cos\left(2\,\pi\frac{BA_j(x,r_j)}{\Phi_0/2}\right). \qquad (5)$$

The net result is obtained by averaging over all coherent trajectories for each impurity and over all impurities:

$$\overline{\Delta R}=\Delta U_{\mathrm{osc}}/I-\sum_{x=0}^{\infty}\int_{r_j=x}^{r}\cos\left(2\,\pi\frac{BA_j(x,r_j)}{\Phi_0/2}\right)dr_j$$

$$\sim\int_0^r dx\int_x^r\cos\left(2\,\pi\frac{BA_j(x,r_j)}{\Phi_0/2}\right)dr_j. \qquad (6)$$

Since even for $l_{\mathrm{el}}\sim0.1$ mm an arbitrary layer parallel to the boundary, with a thickness of the order of the size of the impurity and an area $\sim l_{\mathrm{el}}^2$, can contain, according to the usual estimate of the concentration $c_i\sim(l\sigma)^{-1}$, not less than 10^6 impurities, including impurities of maximum cross section, the summation can be replaced by integration. The calculation reduces to the evaluation of integrals of the Fresnel type (see, e.g., Ref. 19). For the coherent trajectories connected to an impurity with coordinate x, the integration over r_j determines the uncompensated contribution of the cross sections $A_{\mathrm{edge}}(x)$ at the edge of the integration for $r_j=r$, where the phase is stationary, i.e., where

$$\frac{\partial A_j(x,r_j)}{\partial r_j}=\frac{xr}{\sqrt{r^2-x^2}},$$

while the integration over x determines the uncompensated contribution of the extremal area $A_{\mathrm{edge}}^{\mathrm{max}}$ under the trajectory with an impurity of maximum cross section, $\sigma_{\mathrm{max}}\sim q_{\mathrm{max}}^2$, for the maximum value allowed by criterion (3), $r_{q_{\mathrm{max}}}$, at which

$$\frac{\partial A_{\mathrm{edge}}(x)}{\partial x}=0.$$

This condition corresponds to an area

$$A_{\mathrm{max}}=A_{\mathrm{edge}}^{\mathrm{max}}=\frac{1}{2}r_{q_{\mathrm{max}}}^2,$$

which is realized at $\theta=\pi/2$ for an impurity of maximum cross section lying a distance $x_{\mathrm{max}}=(\sqrt{2}/2)r_{\mathrm{max}}$ from the NS boundary.

Thus the calculations show that in the system of coherent trajectories under consideration there exists one trajectory, bounding by the extremal (maximum in magnitude) area of quantization, which can bring about an uncompensated change of phase upon a change in the magnetic vector potential.

The value of A_{max} is determined to an accuracy $\delta A_{\mathrm{edge}}/A_{\mathrm{edge}}\sim q_{\mathrm{max}}/r_{\mathrm{max}}$. In metals $q\approx2-5$ Å, so that $\delta A_{\mathrm{edge}}/A_{\mathrm{edge}}\ll1$ and the change of φ, which determines the number of oscillation periods, can, in a certain region of B_c values, depend mainly on just the change in flux of the magnetic vector potential through the uncompensated extremal area bounded by the coherent trajectory of extremal length. Thus the quantum character of the interaction of interfering coherent excitations with elastic scattering centers in the normal layers of the domains of the intermediate state upon a change in temperature, which specifies a change in the (critical) magnetic field in these layers, should lead to dissipative oscillations of the charge transport through the SNS structure:

$$\Delta U_{\mathrm{osc}}/I\propto c_{q_{\mathrm{max}}}\sin\left(2\,\pi\frac{BA_{\mathrm{max}}}{\Phi_0/2}\right) \qquad (7)$$

($c_{q_{\mathrm{max}}}$ is the concentration of impurities of maximal cross section).

The maximum number of oscillation periods Δ_{B_c} that can be observed upon a change in temperature clearly depends on the scale of the variation of B_c, from the value $B_c(T_0) = B_{e,I}$ at the temperature T_0 at which the SNS structure of the intermediate state arises, to the value $B_c(T)$ at the given temperature. Therefore, the phase of the oscillations at a given temperature should depend on the values of $B_{e,I}$:

$$\varphi = 2\pi \frac{[B_c(T) - B_{e,I}]A_{\max}}{\Phi_0/2}. \tag{8}$$

Estimating the interval of B_c values in which one can neglect the change of A_{edge} with a change in B_c, we find on the basis of (8) and the differential of the parameter r from expression (3) that this interval is $\Delta B_c \approx 3\Delta_{B_c}$, where Δ_{B_c} is the oscillation period. Furthermore, this order of magnitude of ΔB_c corresponds to the value of B_c at which the oscillations begin to be observable, and it differs from the value corresponding to the point at which the NS structure appears, $B_c(T_0) = B_{e,I}$. It is useful to take this feature into account when identifying the temperature region of the oscillations. Since the interference of coherent excitations can alter the dissipative contribution of an impurity interacting with them,[10] one expects that the amplitude of the oscillations, $\Delta U_{\text{osc}}/I$, will be determined solely by the concentration of elastic scattering centers of maximal cross section, which is proportional to the total concentration c in the case of a more or less uniform distribution of scattering centers, and is independent of temperature, as is reflected in expression (7).

It is appropriate here to compare (although qualitatively) the order of the interference contributions to the conductance in the absence of an NS boundary, in the approximation of a weak-localization mechanism, and in the presence of an NS boundary, in the framework of the mechanism considered in this paper, since such a comparison has not been done previously (except in the case of a narrow SNS contact in the diffusional limit[20]). Using a qualitative method of estimating the probability of formation of coherent trajectories[21] (or of self-crossing trajectories in the weak-localization theory), we find that the probability that coherent trajectories will arise in the case of an NS boundary in a layer with a characteristic size of the order of the mean free path is larger by a factor of $(r/\lambda)^2 \sim 10^8$ ($\lambda \sim \sqrt{\sigma}$ is the de Broglie wavelength) than the probability of formation of self-crossing trajectories, since it is determined by the area of the base of the cone formed by accessible coherent trajectories arising as a result of Andreev reflection, the base of the cone resting on the superconductor and the vertex at an impurity. Hence the expected relative interference contribution to the resistance for an NS system is

$$\frac{\Delta\rho}{\rho} \sim (r/\lambda)^2 (\lambda/l_{\text{el}})^2, \tag{9}$$

where the second factor is the main quantum correction of the weak-localization theory in the absence of NS boundaries. As will be seen from the exposition below, this agrees completely with the value of the amplitude of the oscillations which we observed in a Pb slab if the estimate (9) is done for the specific relationship of the parameters corresponding to the experimental conditions.

4.2. Comparison with experiment

Estimates of the characteristics of an SNS structure of the intermediate state of type-I superconductors according to the phenomenological theory of superconductivity[13,22] for our samples give the following results. The change of the values of B_c in the normal regions of the domains for the lead slabs corresponded to a change in the characteristic parameter of the theory, $h = B_e/B_c(T)$, in the range $0.5 \leqslant h \leqslant 1$ for temperatures in the interval 1.5–4.2 K and in the range $0.65 \leqslant h \leqslant 0.83$ for the interval 2–3 K (shown on the upper scale in Fig. 6 are the changes of B_e from the value of B_c at $T = 2.9$ K). For the Sn neck at a value of the self-magnetic field $B_I \approx 100$ G the temperature interval in which oscillations are exhibited corresponds to a variation of h in the range $0.5 \leqslant h \leqslant 1$. Finally, the widest range of variation of h on account of a small B_I in the analogous temperature interval is realized for an In slab in the Cu–In system: $0.03 \leqslant h \leqslant 1$. According to Refs. 13 and 22, the expression for the domain size has the form

$$d = [AW/f(h)]^{1/2}.$$

Here A is a dimensional constant of the surface tension at the NS boundary, and W is the width of the Pb slab in the case of an external field or the effective width, equal to the thickness of Sn or In, in the case of the self-field of the current. Taking into account that $f(h) = (\ln 2/\pi)(1-h)^2$ at $h \to 1$ and $f(h) = (h^2/\pi)(0.56/h)$ at $h \to 0$,[23] we find that the number of domains within the boundaries of the measuring probes for our samples in the intermediate state can range from about 12 at 3 K to 26 at 1.5 K for a Pb slab, from one to two in the entire interval of oscillations for the Sn neck, and from 3 to 10 for an In slab below 3.3 K. These values correspond to a variation of the width d_N of the normal layers in the domains between NS boundaries in the range 5–22 μm for Pb and Sn and 6–70 μm for In, which is less than or comparable to l_{el} for the investigated metals and permits treating the regime in which dissipative oscillations are manifested as being the "clean" limit for all the samples.

Expression (9) gives an estimate of the amplitude of the oscillations for a region of normal metal with a volume of the order of l_{el}^3. A more or less concrete estimate for our experiment can be made only for a Pb slab, where the probes are placed directly on the superconductor:

$$\frac{\Delta R_{\text{osc}}}{R} \sim \int_0^{l_e/v_F} v_F r^2 (d_N t W)^{-1} d\tau \sim 10^{-2} - 1$$

for $d_N \sim 20$–1 μm, $W \sim l_{\text{el}}$ ($t < l_{\text{el}}$ is the thickness of the slab). This estimate agrees with experiment.

For the magnetic fields used to study the Pb slabs, $T_0 \approx 5.5$ K lies outside the helium temperature interval, but for reasons having to do with the measurement error (see Sec. 2) the oscillations below this point, down to 3.2 K, are not being taken into consideration here, and we are restricting discussion to approximately two oscillation periods (Fig. 6). Comparing the amplitude of the latter with the amplitude of the oscillations observed in the Sn neck, we find
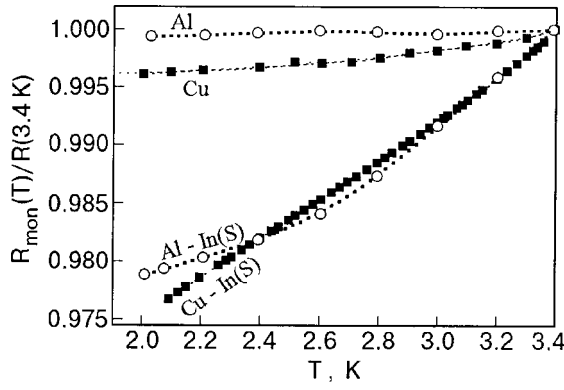
FIG. 11. Temperature dependence of the monotonic component of the resistance of doubly connected *NS* systems Al–In (Ref. 5) and Cu–In (lower curves), measured when the probe in the normal metal (Al, Cu) is withdrawn to distance from the contact with the superconductor of the order of the inelastic mean free path. The upper curves show the temperature behavior of the resistance of the same metals in the absence of an *NS* boundary. For comparison of the curves the data are presented on a single scale in relative units.

$$\frac{(\Delta U_{osc}/I)_{Sn}}{(\Delta U_{osc}/I)_{Pb}} \sim \frac{RRR_{Pb}}{RRR_{Sn}}\frac{c_{Sn}}{c_{Pb}} = 10$$

($c_{Sn, Pb}$ are the impurity concentrations), and this result also corresponds to the features of the oscillation mechanism under consideration. It explains the relationship of the phases of the oscillations for a Pb slab in various fields (Fig. 6), which follows directly from expression (6): $\varphi_{550\,G} - \varphi_{480\,G} \approx \pi$; $\varphi_{520\,G} - \varphi_{480\,G} + \pi \approx 3\pi$ [here we have taken into account that $\mathbf{B}(520\,G) = -\mathbf{B}(480\,G)$].

In the sample containing In, because of the small $B_I \approx 5$ G, the values of T_0 and $T_c(0)$ are extremely close, so that in the same temperature interval as for Sn and Pb one can observe more than 3 oscillation periods (Fig. 8), i.e., a number for which, as was estimated above, the change of A_{max} and, hence, of the oscillation period, is hardly noticeable. It follows from the data presented in Fig. 8 that for a large enough number of oscillation periods a certain dependence of the period on B_c appears. In the interval of variation of B_c indicated in Fig. 8 the period doubles, a finding that agrees completely with the features of the oscillation mechanism under study. The decrease of the oscillation amplitude in the Cu–In system by another order of magnitude in comparison with $\Delta U_{osc}/I$ for Pb is due to the fact that the probe in the normal region is at a considerable distance ($\approx 600\,\mu$m) from the Cu–In *NS* boundary, although this distance is only a few times larger than the mean free path in the Cu single crystal. For this position of the probe there is another independently manifested quantum dissipation mechanism, which is due to relaxation of the phase within the inelastic mean free path[11] and has been considered in detail in our previous paper.[6] It is responsible for the increase in the temperature-dependent contribution of inelastic scattering to the conductance of the normal metal as a whole upon the appearance of an *NS* boundary and is manifested as an enhanced temperature dependence of the monotonic component in comparison with that in the absence of an *NS* boundary (Fig. 11).

The significant distortions of the shape of the oscillations in the Pb sample is most likely due to variations of the value of q_{max} when the number of domains in this sample in the investigated temperature interval changes, altering the position of the *NS* boundaries. Upon such a change the whole interval of possible variations of $q_{max} = 2$–5 Å is apparently realized for metals, the scale of which, however, can only distort the shape of the oscillations without eliminating the overall picture of their periodicity.

Finally, the most important features of the behavior of the oscillations, which agree with the fundamental properties of the proposed quantum mechanism, are those which are inherent to all the metals and sample configurations considered. These are that the oscillation period is of the order of same order of magnitude (≈ 50 G) for a comparable order of magnitude of the critical field in the normal regions of the domains of the intermediate state, and that the oscillation amplitude is temperature independent. From the condition $\Delta_{B_c} A_{max} = \Phi_0/2$ we find that this period corresponds to the interaction of coherent excitations with impurities found at a distance of the order of 1 μm from the *NS* boundaries, which accords with the theoretical treatment. The absence of temperature dependence of the amplitude of the oscillations indicates that they are not connected with the temperature-dependent parameters of decoherence, such as the inelastic electron–phonon and electron–electron mean free path and the thermal coherence length. This means that the dissipative oscillations can be due to only those closed trajectories of the coherent excitations which lie in a layer adjacent to the *NS* boundary, with a thickness less than the indicated decoherence lengths. The indicated layer thickness and the experimental conditions corresponded to these requirements.

5. CONCLUSION

We have investigated experimentally the conductance of *NS* structures of the intermediate state of type-I superconductors in simply connected (Pb and Sn) and doubly connected (Cu–In) configurations of the samples, with large elastic mean free paths of the electrons. Dissipative oscillations as a function of temperature and critical magnetic field, which are oscillations of the Aharonov–Bohm type, are observed. The phase and period of the oscillations vary in a direct relation with the value of the magnetic field. The oscillation period corresponds to a change in the magnetic flux by one flux quantum $hc/2e$ within an area of the order of 1 μm^2. The phase of the oscillations is sensitive to the orientation and magnitude of the external magnetic field. The amplitude of the oscillations is a weak function of temperature in comparison with the monotonic component, which varies by several orders of magnitude. A quantum-interference mechanism is proposed for the scattering of coherent excitations on elastic centers in a magnetic field, which explains the nature and features of the observed resistance oscillations. It is based on allowance for the criterion of spatial limitation of the interaction of coherent excitations with elastic scattering centers under conditions of Andreev reflection.

*E-mail: chiang@ilt.kharkov.ua

[1] Yu. N. Tszyan (Chiang) and O. G. Shevchenko, Fiz. Nizk. Temp. **14**, 543 (1988) [Sov. J. Low Temp. Phys. **14**, 299 (1988)].

[2] C. J. Lambert and R. Raimondi, J. Phys.: Condens. Matter **10**, 901 (1998).

[3] B. L. Altshuler, D. E. Khmelnitsky, A. I. Larkin, and P. A. Lee, Phys. Rev. B **20**, 5142 (1980).

[4] S. Washburn and R. A. Webb, Adv. Phys. **35**, 375 (1986).

[5] A. G. Aronov and Yu. V. Sharvin, Rev. Mod. Phys. **59**, 755 (1987).

[6] Yu. N. Tszyan (Chiang), S. N. Gritsenko, and O. G. Shevchenko, Zh. Éksp. Teor. Fiz. **118**, 1426 (2000) [JETP **91**, 1235 (2000)].

[7] Yu. N. Tszyan (Chiang) and O. G. Shevchenko, Zh. Éksp. Teor. Fiz. **113**, 1064 (1998) [JETP **86**, 582 (1998)].

[8] Yu. N. Chiang and O. G. Shevchenko, Fiz. Nizk. Temp. **25**, 432 (1999) [Low Temp. Phys. **25**, 314 (1999)].

[9] Yu. N. Tsyan (Chiang), JETP Lett. **71**, 334 (2000).

[10] J. Herath and D. Rainer, Physica C **161**, 209 (1989).

[11] B. J. van Wees, P. de Vries, P. Magnic, and T. M. Klapwijk, Phys. Rev. Lett. **69**, 510 (1992).

[12] Yu. N. Tszyan, Prib. Tekh. Éksp., No. 1, 202 (1981).

[13] P. G. de Gennes, *Superconductivity of Metals and Alloys* [Benjamin, New York-Amsterdam (1966); Mir, Moscow (1968)].

[14] *Handbook of Chemistry and Physics*, Chemical Rubber Co., Cleveland, Ohio (1974–1975).

[15] Y. Aharonov and D. Bohm, Phys. Rev. **115**, 485 (1959).

[16] B. L. Al'tshuler, A. G. Aronov, and B. Z. Spivak, JETP Lett. **33**, 94 (1981).

[17] A. F. Andreev, Zh. Éksp. Teor. Fiz. **46**, 1823 (1964) [Sov. Phys. JETP **19**, 1228 (1964)]; Zh. Éksp. Teor. Fiz. **49**, 655 (1965) [Sov. Phys. JETP **22**, 455 (1966)].

[18] A. M. Kadigrobov, Fiz. Nizk. Temp. **19**, 943 (1993) [Low Temp. Phys. **19**, 671 (1993)]; A. Kadigrobov, R. Shekhter, and M. Jonson, Physica B: Condens. Matter **218**, 134 (1996).

[19] J. M. Ziman, *Principles of the Theory of Solids* [Cambridge University Press (1964); Mir, Moscow (1966)].

[20] B. L. Al'tshuler and B. Z. Spivak, Zh. Éksp. Teor. Fiz. **92**, 607 (1987) [Sov. Phys. JETP **65**, 343 (1987)].

[21] A. A. Abrikosov, *Fundamentals of the Theory of Metals* [North-Holland, Amsterdam (1988); Nauka, Moscow (1987)].

[22] L. D. Landau and E. M. Lifshitz, *Electrodynamics of Continuous Media* [Pergamon Press, Oxford (1960); Goslitizdat, Moscow (1957)].

[23] E. M. Lifshits and Yu. V. Sharvin, Dokl. Akad. Nauk **79**, 783 (1951).

Translated by Steve Torstveit

ELECTRONIC PROPERTIES OF METALS AND ALLOYS

Influence of temperature, magnetic field, and high hydrostatic pressure on the resistivity and magnetoresistance in $La_{0.9}Mn_{1.1}O_{3\pm\delta}$ ceramics and laser-deposited films

V. P. Pashchenko, S. S. Kucherenko, P. I. Polyakov,* A. A. Shemyakov, and V. P. Dyakonov

A. A. Galkin Donetsk Physico-Technical Institute, National Academy of Sciences of Ukraine, ul. Rozy Lyuksemburg 72, 83114 Donetsk, Ukraine

The influence of the magnetic field strength ($H = 0$, 2, 4, 6, 8 kOe), high hydrostatic pressures ($P = 0 - 1.8$ GPa), and temperature ($T = 77 - 300$ K) on the resistivity ρ, magnetoresistance ($\Delta R/R_0$), and phase transition temperatures in ceramic and thin-film samples of the lanthanum manganite $La_{0.9}Mn_{1.1}O_{3\pm\delta}$ is investigated by x-ray-diffraction, magnetic, and resistive methods. It is found that with increasing H and P the resistivity decreases and the temperatures T_{ms} of the metal-semiconductor phase transition and T_p of the magnetoresistance peak increase. The differences in the resistivities, magnetoresistances, and phase transition temperatures in the ceramics and laser-deposited films are explained by their different nonstoichiometry and defect density. The observed linear dependence of ρ and T_{ms} on P suggests that lanthanum manganite ceramics and films could be used as pressure and temperature sensors. © *2001 American Institute of Physics.* [DOI: 10.1063/1.1430843]

INTRODUCTION

Rare-earth manganites with the perovskite structure, thanks to the colossal magnetoresistance effect,[1–4] are among the most interesting and intensively investigated functional materials. In spite of a large number of publications, including review articles,[5–8] the nature of the unique interrelation of the magnetic and electrical properties in these manganites remains in dispute. One of the promising thrusts for elucidating the physical nature and the creation of new magnetoresistive materials is to study their structure and properties near phase transitions under the influence of magnetic fields and high pressures over a wide temperature interval.

The influence of temperature and magnetic fields has been the subject of a rather large number of studies, while high isostatic pressures[9,10] and especially the combined influence of T, H, and P on the magnetoresistance have been studied considerably less.[11,12] There have been practically no such studies done simultaneously on ceramic targets and single-crystal thin films obtained from them. Therefore, the goal of this study was to solve a topical problem, viz., to establish the character and degree of influence of the temperature ($T = 77 - 350$ K), magnetic field strength ($H = 0 - 8$ kOe), and high hydrostatic pressures ($P = 0 - 2.1$ GPa) on the resistivity and magnetoresistance in ceramics and laser-deposited films.

Unlike the majority of studies done on doped lanthanum manganite perovskites without excess manganese, $La_{1-x}^{3+}Me_x^{2+}Mn_{1-x}^{3+}Mn_x^{4+}O_3^{2-}$ ($Me^{2+} = Ca^{2+}$, Sr^{2+}, Ba^{2+}, Pb^{2+},) here we have studied ceramic and film samples of the autodoped magnetoresistive metal oxide $La_{0.9}^{3+}Mn_{1.1}O_{3\pm\delta}^{2-}$ containing superstoichiometric manganese.[13,14]

METHODS OF SAMPLE PREPARATION AND STUDY

The ceramic samples used as targets for laser sputtering were obtained after a 20-hour two-stage (900 and 950 °C) synthesizing anneal of the powders and a sintering of the pressed ($P = 0.5$ MPa) samples at 1150 °C for 24 hours in a metal press form. From a ceramic target 24 mm in diameter we laser deposited a single-crystal film of $La_{0.9}Mn_{1.1}O_{3\pm\delta}$ with a thickness $d \approx 1000$ Å on a $LaSrGaO_4$ substrate having a lattice parameter $a = 3.84$ Å and oriented in the (100) plane.

The phase composition of the samples and the type and parameters of the crystal structure were determined by an x-ray diffraction method on a DRON-2 diffractometer in Cu radiation. The resistance was measured in direct current by the four-probe method at magnetic fields $H = 0$, 2, 4, 6, and 8 kOe. The temperature was determined from the resistance of a bifilarly wound copper coil. High hydrostatic pressures $P = 0 - 2.2$ GPa were produced in the high-pressure chamber described in Ref. 15 and were measured by the method indicated in Ref. 16.

The errors of measurement of the parameters did not exceed 3% for the phase composition, 1% for the crystal lattice parameters, 0.7% and 1.5% for the resistance and resistivity, respectively, 0.1% for the temperature, 1.5% for the magnetic field, and 3% for the hydrostatic pressure.

EXPERIMENTAL RESULTS AND DISCUSSION

According to the x-ray diffraction data, the ceramic samples are single-phase with a perovskitelike $Pnma$ structure. The lattice parameters of this structure are $a = 5.505$ Å, $b = 5.552$ Å, $c = 7.796$ Å. According to the NMR
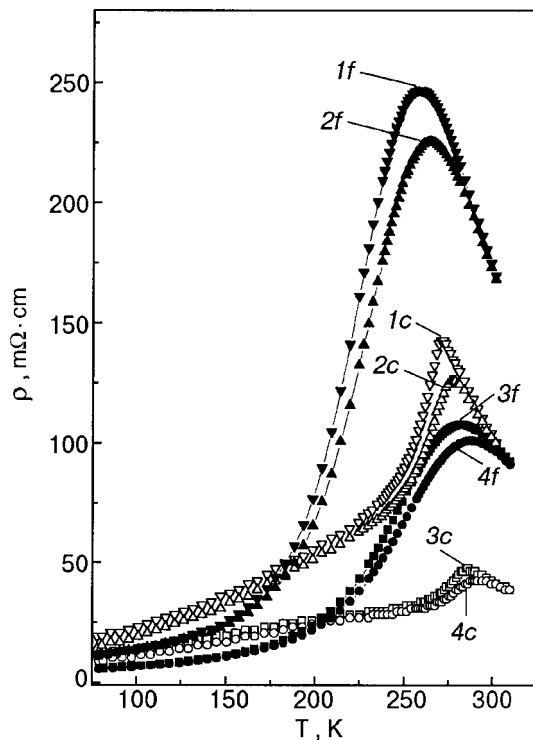
FIG. 1. Temperature dependence of the resistivity of ceramic (c) and film (f) samples of $La_{0.9}Mn_{1.1}O_{3\pm\delta}$: 1—$P=0$, $H=0$; 2—$P=0$, $H=8$ kOe; 3—$P=1.8$ GPa, $H=0$; 4—$P=1.8$ GPa, $H=8$ kOe.

data, for ^{55}Mn the frequency for Mn^{3+} and Mn^{4+} ions in the octahedral B positions in rf electron exchange was $F=375$ MHz. This, together with the frequency of Mn^{3+} ($F_1=420$ MHz) and Mn^{4+} ($F_2=310$ MHz)[17,18] made it possible to determine the averaged intermediate valence of the manganese ions in the B positions: $\bar{\omega}\approx3.5$. The NMR of ^{55}Mn in the film could not be determined by of its too-small mass and ^{55}Mn content. The crystal structure of the film was close to cubic with a lattice parameter $a=3.906$ Å.

The temperature dependence of the resistivity ρ of the ceramic target (c) and laser film (f) at the lowest and highest values of the magnetic field ($H=0$ and 8 kOe) and at high hydrostatic pressures ($P=0$ and 1.8 GPa) are shown in Fig. 1. The resistivity of the ceramic is much smaller than that of the film, possibly because of their different porosity, the presence or absence of intercrystallite zones, and, most importantly, the different nonstoichiometry δ of the $La_{0.9}Mn_{1.1}O_{3-\delta}$. According to Refs. 19 and 20, the resistance decreases with decreasing nonstoichiometry. It must therefore be assumed that in the films, which were not additionally annealed and were therefore underoxidized, the oxygen content is lower than in the ceramic ($\delta_f > \delta_c$) and, hence, its resistance is higher. Increasing H to 8 kOe or increasing P to 1.8 GPa causes the resistance of the ceramic to decrease by a factor of 1.1 or 3.0, respectively, and that of the film by a factor of 1.1 or 2.3. This indicates that the influence of H is comparable in the ceramic and film and that the influence of P is greater in the ceramic than in the film. The temperature of the metal-semiconductor transition at $H=0$ and $P=0$ is $^cT_{ms}=270$ for the ceramic and considerably lower for the film: $^fT_{ms}=258$ K.

Using our data and published data on the interrelation of the phase transition temperatures and the oxygen nonstoichiometry, we can determine the value of $\Delta\delta$ between the ceramic and film. According to Refs. 19 and 20, $\Delta\delta/\Delta T=4\times10^{-4}$ for $La_{0.7}Sr_{0.3}MnO_{3-\delta}$ and, according to Ref. 20, $\Delta\delta/\Delta T=6\times10^{-4}$ for $La_{1-\delta}Mn_{1-\delta}O_3$. Then for the ceramic and film in our case $\Delta\delta\approx6\times10^{-4}\times12\approx0.007$, since $\Delta T_{ms}={}^cT_{ms}-{}^fT_{ms}=12$K. It is noteworthy that the sensitivity of the phase transition temperatures to the nonstoichiometry in magnetoresistive manganites is substantially larger than in cuprate high-T_c superconductors. For example, $\Delta\delta/\Delta T\approx6\times10^{-3}$ for $YBa_2Cu_3O_{7-\delta}$ (Refs. 21 and 22).

The sensitivity of the phase transition temperatures to the oxygen nonstoichiometry in manganites is an order of magnitude higher than in ferrites. In magnetite,[23] for example, on going from Fe_3O_4 to $Fe^{3+}_{2.67}V^{(c)}_{0.33}O^{2-}_4$ ($\Delta\delta=0.5$) the Curie temperature increases from 858 to 948 K, i.e., $\Delta\delta/\Delta T=5\times10^{-3}$, which differs from the value for our manganites by an order of magnitude.

According to our results,[13,21] the real structure of autodoped lanthanum manganite perovskites $La_{1-x}Mn_{1+x}O_{3\pm\delta}$ has deficiencies in both the cation and anion sublattices and contains more complex defects of the cluster type. The composition and structure of the clusters is close to Mn_3O_4 and/or γ-Mn_2O_3 with a superposition of heterovalent manganese ions and with cation $V^{(c)}$ and anion $V^{(a)}$ vacancies: $Mn^{3+}_1 Mn^{4+}_{0.5} Mn^{2+}_{0.5} V^{(c)}_{0.2} O^{2-}_3 V^{(a)}_{0.3}$. In the x-ray diffraction studies these clusters are manifested in the form a halo at angles $\theta_1=50$–$55°$ and $\theta_2=60$–$65°$ (Cr radiation) for the (134) and (233) planes and for the (420) and (413) planes, respectively.

The magnetism of these planar clusters can be represented as antiferromagnetic formations with a slightly canted structure, with a Néel temperature $T_N=42$-45 K. It is remarkable that the total magnetic moment of the samples decreases in low fields and increases in high fields, and by practically the same amount. This behavior can be explained by a three-sublattice structure of the clusters containing heterovalent manganese ions and cation and anion vacancies. Here the magnetic moments of Mn^{3+}, Mn^{4+} and Mn^{2+} in the cluster are apparently directed oppositely (an analogous situation occurs in Cr-doped manganites[25]).

It is natural to suppose that the influence of temperature, magnetic field, and high hydrostatic pressure on the properties, including the phase transition temperatures and the magnetoresistance, should depend strongly on the structural quality and, primarily, on complex defects of the cluster type.

When H is increased to 8 kOe or P is increased to 1.8 GPa the temperature T_{ms} increases: by 6 or 15 K for the ceramic and by 6 or 24 K for the film, respectively. These data show that, first, the high hydrostatic pressure has the greater influence on the resistance and metal-semiconductor phase transition temperature, and, second, while the influence of the magnetic field strength on T_{ms} is about the same in the ceramic and film, the effect of pressure is more pronounced for the film.

The influence of the magnetic field strength on the magnetoresistance in the ceramic and film at $P=0$ is shown in Fig. 2. The magnetoresistance increases substantially with increasing H. It should be noted that the temperature dependence of $\Delta R/R_0$ is of a different character for the ceramic
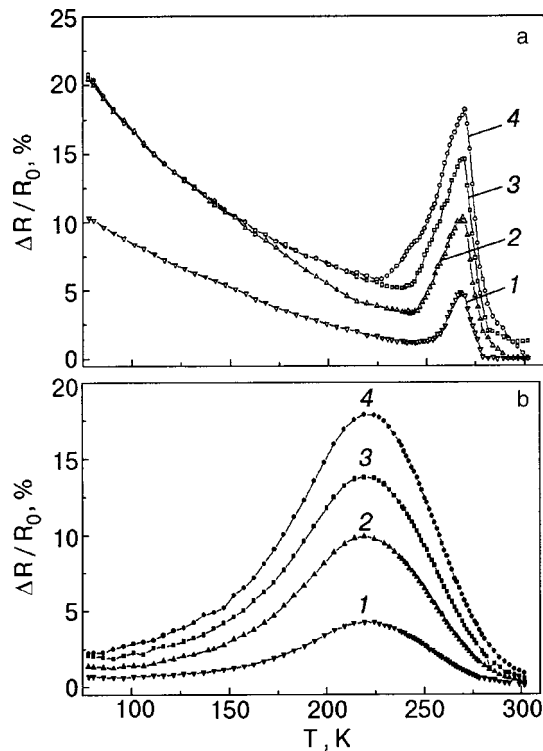
FIG. 2. Temperature dependence of the magnetoresistance in ceramic (a) and film (b) samples of $La_{0.9}Mn_{1.1}O_{3\pm\delta}$ at $P=0$ for various values of the magnetic field H [kOe]: 2 (*1*), 4 (*2*), 6 (*3*), 8 (*4*).

FIG. 3. Temperature dependence of the magnetoresistance of ceramic (a) and film (b) samples of $La_{0.9}Mn_{1.1}O_{3\pm\delta}$ at $P=1.8$ GPa for various values of the magnetic field H [kOe]: 2 (*1*), 4 (*2*), 6 (*3*), 8 (*4*).

and film in the temperature interval 77–200 K, i.e., below T_{ms}. One also notices that the peak of the magnetoresistance is substantially higher for the ceramic ($^cT_p=269$ K) than for the film ($^fT_p=210$ K). Thus for $P=0$ and $H=8$ kOe one has $^cT_p=269$ K and $^fT_p=219$ K. In our opinion, this is also due to the different nonstoichiometry on account of the higher oxygen content in the ceramic, which is slowly oxidized after sintering. Here T_p is practically independent of H. The temperature interval of the phase transitions, ΔT_p, like ΔT_{ms}, is substantially wider for the film (see Figs. 1–3), which is unusual but may also be due to its larger oxygen nonstoichiometry. Figure 3 shows the temperature dependence of the magnetoresistance of the ceramic and film at $P=1.8$ GPa for different values of the magnetic field ($H=2, 4, 6, 8$ kOe). At $P=1.8$ GPa (Fig. 3) the magnetoresistance in a field $H=8$ kOe has decreased in comparison with $P=0$ (Fig. 2) by 4.3% for the ceramic and by 4.7% for the film. The temperature T_p has increased: by 14 K for the ceramic and by 24 K for the film. Thus the pressure has a greater effect on the magnetoresistance and T_p for the film, in which the oxygen nonstoichiometry of the real structure is higher.

The influence of high hydrostatic pressures on the resistivity of the ceramic (curve *1*) and film (curve *2*) at $H=0$ is illustrated by Fig. 4. Increasing the pressure from 0 to 1.8 GPa decreases the resistivity by a factor of 2.6 for the ceramic and by a factor of 2 for the film. This decrease amounts to 61% for the ceramic and 51% for the film. It is particularly noteworthy that the resistivities of the ceramic and film have a practically linear dependence on the high hydrostatic pressure, making these materials promising for use as pressure sensors. This dependence has the form $^c\rho$
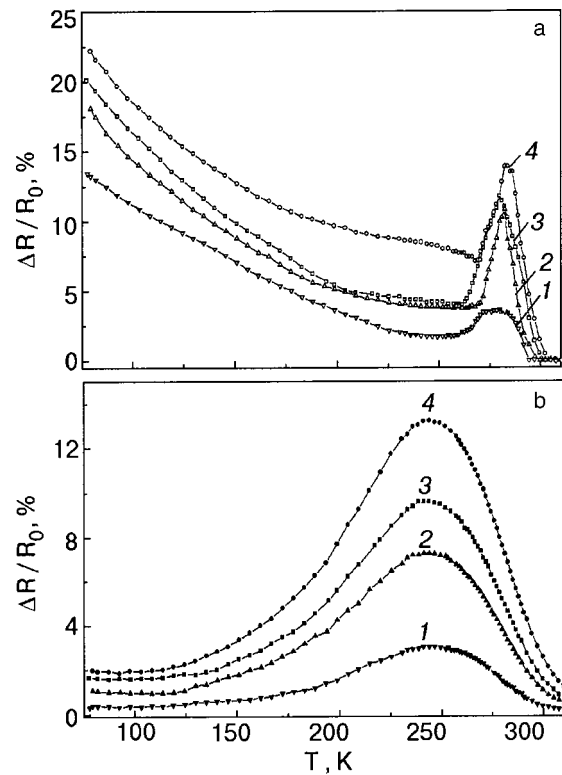
$=97.82-31.06P$ for the ceramic and $^f\rho=198.25-55.62P$ for the film.

The effect of high hydrostatic pressure on the metal-semiconductor phase transition temperature T_{ms} of the ceramic (unfilled symbols) and film (filled symbols) is shown in Fig. 5. In contrast to Ref. 24, where strong variations of the temperature of the thermopower peak in the $La_{0.875}Sr_{0.125}MnO_3$ single crystal were observed at $P>0.9$ GPa, in our case T_{ms} and T_p increased noticeably over the entire pressure interval ($P=0-0.18$ GPa). T_{ms} increases practically linearly with P in both the ceramic and film. The maximum values of these phase transition temperatures are associated with the maximum values of the magnetic field ($H=8$ kOe) and of the high hydrostatic pressure ($P=1.8$ GPa). The linear trends of $\rho(P)$, $T_{ms}(P)$, and $T_p(P)$

FIG. 4. Influence of high hydrostatic pressures on the resistivity of lanthanum manganite ceramic (*1*) and film (*2*) samples at $H=0$.

FIG. 5. Influence of high hydrostatic pressures on the temperature T_{ms} of ceramic (c) and film (f) samples of the magnetoresistive lanthanum manganite perovskites $La_{0.9}Mn_{1.1}O_{3 \pm \delta}$ at $H=0$ (I) and $H=8$ kOe (2).

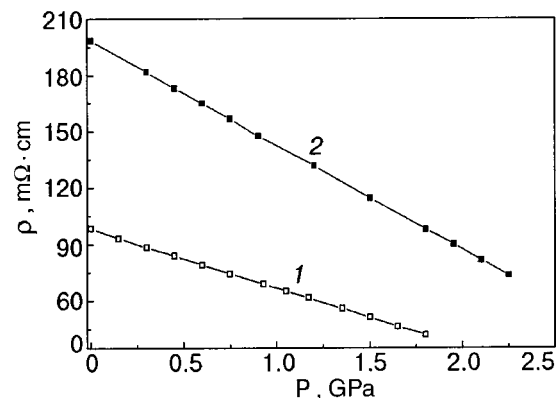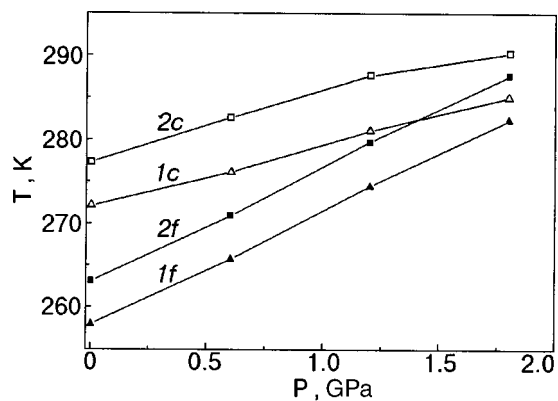remain linear to 1.8 GPa and even to 2.2 GPa, as we have shown for the film. The high sensitivity of the phase transition temperatures to the nonstoichiometry presents an opportunity for determining these temperatures, and the high sensitivity to the pressure might make these materials useful as sensors for the measurement of high hydrostatic pressures.

CONCLUSIONS

1. With increasing magnetic field the resistivity decreases substantially, the phase transition temperature T_{ms} increases weakly, and the magnetoresistance increases strongly in the ceramic and in the film.

2. With increasing high hydrostatic pressure the resistivity and magnetoresistance decrease, while the phase transition temperature T_{ms} increases, and this effect is larger in the film.

3. We have found that the influence of high hydrostatic pressure on the resistivity is stronger for the ceramic, while its effect on the magnetoresistance and phase transition temperatures is stronger for the film.

4. The differences in the resonances, magnetoresistance, and phase transition temperatures and also the degree of influence of H and P on the properties of the ceramic and film are explained by their different nonstoichiometry and defect density.

5. The linear relations observed between ρ and P and between T and P could be exploited to use ceramic and film samples of this compound as combined pressure and temperature sensors.

The authors thank A. V. Klimov for providing the film samples and H. Szymczak for interest in this study. This

*E-mail: poljakov@host.dipt.donetsk.ua

[1] J. Fontcuberta, B. Martínez, A. Seffar, S. Piñol, J. L. García-Múñoz, and X. Obradors, Phys. Rev. Lett. **76**, 1122 (1996).
[2] G. H. Rao, J. R. Sun, J. K. Liang, W. Y. Zhou, and X. R. Cheng, Appl. Phys. Lett. **69**, 424 (1996).
[3] J. E. Mitchell, D. N. Argyrion, C. D. Potter, D. G. Hinks, J. D. Jorgensen, and S. D. Bader, Phys. Rev. B **54**, 6172 (1996).
[4] N. D. Mathur, G. Burnell, S. P. Isaac, T. J. Jackson, B.-S. Teo, J. L. MacManus-Driscoll, L. F. Cohen, J. E. Evetts, and M. G. Blamive, Nature (London) **387**, A15, 266 (1997).
[5] É. L. Nagaev, Usp. Fiz. Nauk **166**, 833 (1996).
[6] A. P. Ramirez, J. Phys.: Condens. Matter **9**, 8171 (1997).
[7] V. M. Loktev and Yu. G. Pogorelov, Fiz. Nizk. Temp. **26**, 231 (2000) [Low Temp. Phys. **26**, 171 (2000)].
[8] S. I. Khartsev, V. N. Krivoruchko, and V. P. Pashchenko, Fiz. Nizk. Temp. **23**, 840 (1997) [Low Temp. Phys. **23**, 631 (1997)].
[9] K. Kamenev, G. Balakrishman, M. R. Lees, D. McK. Paul, Z. Arnold, and O. Mikulina, Phys. Rev. B **56**, 2285 (1997).
[10] V. E. Arkhipov, V. S. Gaviko, K. M. Demchuk, V. P. Dyakina, A. V. Korolev, Ya. M. Mukovskiǐ, É. A. Neǐfil'd, and R. V. Pomortsev, JETP Lett. **71**, 114 (2000).
[11] I. V. Medvedeva, K. Borner, G. H. Rao *et al.*, Physica B **292**, 250 (2000).
[12] V. Moshnyaga, S. Klimm, K. Samwer *et al.*, J. Appl. Phys. **88**, 5305 (2000).
[13] V. P. Pashchenko, S. I. Khartsev, O. P. Cherenkov, A. A. Shemyakov, Z. A. Samoǐlenko, A. D. Loǐko, and V. I. Kamenev, Neorg. Mater. **35**, 1509 (1999).
[14] V. Dyakonov, A. Prohorov, V. Shapovalov, S. Khartsev, V. Krivoruchko, V. Mihailov, V. Pashchenko, T. Zubov, P. Alekseevych, K. Dyakonov, S. Piechota, and H. Szym-czak, Phys. Lett. A **268**, 202 (2000).
[15] A. V. Oleǐnik, P. I. Polyakov, and V. G. Synkov, Fiz. Tekh. Vysokikh Davlenii **4**, 88 (1994).
[16] L. Yu. Vereshchagin, *Solid State at High Pressure* [in Russian], Nauka, Moscow (1981).
[17] A. A. Shemyakov and V. A. Klochan, Zh. Éksp. Teor. Fiz. **101**, 1014 (1992) [JETP **74**, 544 (1992)].
[18] A. A. Shemyakov, V. P. Pashchenko, and A. D. Loyko, Appl. Magn. Reson. **16**, 403 (1999).
[19] R. Mahendiran, S. K. Tiwary, A. K. Raychaudhuri, T. V. Ramakrishnan, R. Mahesh, R. Rangavittal, and C. N. R. Rao, Phys. Rev. B **53**, 3348 (1996).
[20] N. Abdelmoula, K. Guidare, A. Cheikh-Rouhou, *et al.*, Solid State Chem. **151**, 139 (2000).
[21] V. P. Pashchenko, V. S. Abramov, A. V. Pashchenko, Z. A. Samoilenko, and O. P. Cherenkov, Funct. Mater. **3**, 12 (1996).
[22] V. N. Zverev and D. V. Shovkun, JETP Lett. **72**, 73 (2000).
[23] M. T. Varshavskiǐ, V. P. Pashchenko, A. N. Men,' N. V. Suptsov, and A. G. Miloslavskiǐ, *Structural Quality and the Physico-Chemical Properties of Ferrospinels* [in Russian], Nauka, Moscow (1988).
[24] E. S. Itskevich and V. F. Kraǐdenov, Fiz. Tverd. Tela (St. Petersburg) **43**, 1220 (2001) [Phys. Solid State **43**, 1267 (2001)].
[25] I. O. Troyanchuk, D. A. Efimov, V. V. Eremenko, V. A. Sirenko, G. Shim-chak (H. Szymczak), and A. Nabyalek, Fiz. Nizk. Temp. **26**, 39 (2000) [Low Temp. Phys. **26**, 28 (2000)].

Translated by Steve Torstveit

LOW-DIMENSIONAL AND DISORDERED SYSTEMS

Bound states of spatially separated electrons in crossed electric and magnetic fields

E. D. Vol and S. I. Shevchenko*

B. Verkin Institute for Low Temperature Physics and Engineering, National Academy of Sciences of Ukraine, pr. Lenina 47, 61103 Kharkov, Ukraine
(Submitted June 15, 2001)
Fiz. Nizk. Temp. **27**, 1376–1381 (December 2001)

A new mechanism is proposed for the binding of two carriers of the same sign in a two-layer system in crossed electric **E** and magnetic **B** fields of a special form. A field configuration for which the electric and magnetic fields in the layers are equal in magnitude and opposite in direction is considered. In this geometry of the fields an additional integral of the motion arises: the pair momentum **P**. For the case when the masses of the carriers in the layers are considerably different, a method is proposed for calculation the states of a pair without making use of the assumption that the Coulomb interaction between carriers is small. The character of the dependence of the energy of a pair on its momentum, $E(\mathbf{P})$, is determined by the ratio of the fields $|E/B|$. For $|E/B| \gtrsim \Lambda_{cr} \propto e^2/\hbar c$ the energy of a pair is a monotonic function of $|\mathbf{P}|$ and there are no bound states in the system. For $\Lambda \lesssim \Lambda_{cr}$, however, the function $E(\mathbf{P})$ is nonmonotonic. A local maximum and local minimum appear on this function, indicating the appearance of bound states of two carriers of the same sign. The physical mechanism leading to the appearance of bound states in crossed fields is investigated, and their main characteristics are calculated. Ways of realizing these bound states in concrete systems and their possible experimental manifestations are discussed. © *2001 American Institute of Physics.*
[DOI: 10.1063/1.1430844]

By now quite a few mechanisms for the pairing of electrons in metals and semiconductors have been proposed. The overwhelming majority of these mechanisms are based on the attraction between electrons due to the exchange of quanta of some boson field (e.g., a phonon or plasmon field). After the discovery of high-T_c superconductivity a number of new pairing mechanisms were proposed.[1,2] The question of whether superconductivity can arise in systems in which the interaction between electrons is of a purely repulsive character has also been addressed in the literature.[3,4] Later other mechanisms for the appearance of superconductivity in systems with repulsion between electrons were also proposed (see, in particular, Refs. 5 and 6), but all of these mechanisms have been based on analysis of the behavior of a many-particle system. In the present paper we consider a two-particle problem and propose a mechanism for the binding of carriers of the same sign; to our knowledge this mechanism has not been discussed in the literature. We show that in a two-layer system placed in crossed electric and magnetic fields of a special form, there can arise metastable bound states (MBSs) of carriers of the same sign. Let us emphasize from the start the important circumstance that makes the appearance of MBSs possible despite the repulsion between particles: the presence of an additional integral of the motion, viz., the pair momentum **P**. This integral of the motion arises for a special configuration of the external fields applied to a pair of carriers. The mechanism of formation of the MBSs will be discussed later, after we have given a description of the system considered.

We consider two two-dimensional semiconducting layers, separated by a narrow insulating layer of thickness d. We assume that the current carriers in layers 1 and 2 are particles with effective masses m_1 and m_2, respectively. The charges of the carriers are the same in both layers (both in magnitude and in sign). We place this two-layer system in crossed electric and magnetic fields of a special configuration. We shall assume that the magnetic field is applied perpendicular to the layers (the field direction coincides with the z axis), uniformly in each layer, but the fields $\mathbf{B}_1$ and $\mathbf{B}_2$ in the two layers have the same magnitude but opposite orientation, i.e., $\mathbf{B}_1 = -\mathbf{B}_2$. The electric fields are uniform over the layers and lie in the plane of the layers, and for them we also propose the relation $\mathbf{E}_1 = -\mathbf{E}_2 = \mathbf{E}$. The possibility of implementing such a field configuration will be discussed below.

Under the assumptions adopted, the Hamiltonian of the system is written in standard form:

$$H = H_1 + H_2 + V_c + H_E, \tag{1}$$

where

$$H_1 = \frac{[P_{1x} + (eB/2c)y_1]^2}{2m_1} + \frac{[P_{1y} - (eB/2c)x_1]^2}{2m_1}, \tag{2}$$

$$H_2 = \frac{[P_{2x} - (eB/2c)y_2]^2}{2m_2} + \frac{[P_{2y} + (eB/2c)x_2]^2}{2m_2}, \tag{3}$$

$$V_c = \frac{e^2}{|\mathbf{r}_1 - \mathbf{r}_2|} = \frac{e^2}{\sqrt{(x_1 - x_2)^2 + (y_1 - y_2)^2 + d^2}}, \quad (4)$$

$$H_E = e\mathbf{E}\cdot(\mathbf{r}_1 - \mathbf{r}_2). \quad (5)$$

The charge of the carriers in layers 1 and 2 is assumed, for the the sake of definiteness, to be equal to e (electrons). Between the layers the dielectric constant ε is assumed to be unity. For the vector potential in layers 1 and 2 we choose the symmetric gauge

$$\mathbf{A}_1 = \left(-\frac{By}{2}, \frac{Bx}{2}, 0\right) \quad \text{and} \quad \mathbf{A}_2 = \left(\frac{By}{2}, -\frac{Bx}{2}, 0\right).$$

As we shall see, the effect of MBS formation arises in a wide range of parameters of the problem and is determined mainly by the ratio of the fields applied to the system, $|E/B|$. Therefore, we make the additional assumption, which will substantially simplify the calculation, that the masses of the carriers in the layers are very different ($m_2 \gg m_1$). As we have shown previously,[7] for calculating the characteristics of the system in this case one can employ a method that does not make use of the assumption that the Coulomb interaction between carriers is small. In other words, instead of the assumptions usually used, $a_B^{(1)} \gg l_0$ and $a_B^{(2)} \gg l_0$, where $a_B^{(1),(2)} = \hbar^2/m_{1,2}e^2$ is the Bohr radius of the carriers in layers 1 and 2, respectively, and $l_0 = \sqrt{c\hbar/eB}$ is the magnetic length, we will use the less stringent restriction

$$a_B^{(1)} \gg a_B^{(2)} \cong l_0. \quad (6)$$

Let us briefly recall the key features of the method of calculation used (see Ref. 7 for details). It follows from Eq. (6) that the states of the light particle 1 can be assumed to belong to a specified Landau level (for simplicity, the lowest one, with $n=0$.) We project the pair Hamiltonian (1) onto this subspace of states. The result of the projection will be denoted by a bar over the operator. Clearly, $\bar{H}_2 = H_2$, while for H_1 the relation

$$H_1 = \frac{(\Pi_{1x})^2 + (\Pi_{1y})^2}{2m_1} = \hbar\omega_1\left(a^+ a + \frac{1}{2}\right) \quad (7)$$

implies that $\bar{H}_1 = \hbar\omega_1/2$ is a constant quantity, which will henceforth be dropped. In Eq. (7) we have used the following notation: $\omega_1 = eB/m_1 c$ is the cyclotron frequency of the carriers in layer 1, $\Pi_{1x} = P_{1x} + (eB/2c)y_1$ and $\Pi_{1y} = P_{1y} - (eB/2c)x_1$ are the components of the kinematic momentum of the light particle, and $a^+ = (l_0/\sqrt{2}\hbar)(\Pi_{1x} - i\Pi_{1y})$ and $a = (l_0/\sqrt{2}\hbar)(\Pi_{1x} + i\Pi_{1y})$ are the creation and annihilation operators of an electron at a specified Landau level. From the commutation relation for Π_{1x} and Π_{1y},

$$[\Pi_{1x}, \Pi_{1y}] = \frac{i\hbar^2}{l_0^2},$$

it follows that $[a, a^+] = 1$, as it should.

Projection of the Coulomb energy operator is conveniently done by going to the Fourier representation in (4):

$$V_c(\mathbf{r}_1 - \mathbf{r}_2) = \frac{e^2}{2\pi}\int d^2k \frac{e^{-|k|d}}{|k|} e^{-|k|^2 l_0^2/4} e^{ik_x(x_1 - x_2) + ik_y(y_1 - y_2)}, \quad (8)$$

where $|k| = \sqrt{k_x^2 + k_y^2}$.

Let us give the final result of the projection (see Ref. 7 for details):

$$\bar{V}_c = \frac{e^2}{2\pi}\int d^2k \frac{e^{-|k|d}}{|k|} e^{-|k|^2 l_0^2/4} e^{ik_x(X_1 - x_2) + ik_y(Y_1 - y_2)}, \quad (9)$$

where

$$X_1 = x_1 + \frac{l_0^2}{\hbar}\Pi_{1y} \quad \text{and} \quad Y_1 = y_1 - \frac{l_0^2}{\hbar}\Pi_{1x} \quad (10)$$

are the coordinates of the center of the orbit of the light particle. X_1 and Y_1 obey the commutation relation $[X_1, Y_1] = -il_0^2$ and commute with Π_{1x} and Π_{1y}. The result of the projection of H_E is also expressed in terms of $X_1 - x_2$ and $Y_1 - y_2$:

$$\bar{H}_E = eE_x(X_1 - x_2) + eE_y(Y_1 - y_2). \quad (11)$$

We now call attention to the similarity of this problem to that of the behavior of an electron-hole pair in uniform electric and magnetic fields. Gor'kov and Dzyaloshinskiĭ in their famous paper[8] first noted the existence in such a system of a vector integral of the motion, which plays the role of the momentum of a pair in the magnetic field. The presence of this integral simplified the classification of the states and allowed them to find an analytical solution of the problem. For a pair of particles with like sign of the charge in uniform crossed fields such a quantity does not exist. It turns out, however, that the vector integral of the motion reappears for our chosen configuration of the fields ($\mathbf{B}_2 = -\mathbf{B}_1$, $\mathbf{E}_2 = -\mathbf{E}_1$, and $\mathbf{B}_{1,2} \perp 2b\mathbf{E}_{1,2}$). The role of the conserved momentum in our case is played by the quantity

$$\mathbf{P} = \left[i\hbar\frac{\partial}{\partial\mathbf{r}_1} - \frac{e}{c}\mathbf{A}(\mathbf{r}_1)\right] + \left[i\hbar\frac{\partial}{\partial\mathbf{r}_2} - \frac{e}{c}\mathbf{A}(\mathbf{r}_2)\right]$$

$$- \frac{e}{c}[\mathbf{B}_1 \times \mathbf{r}_1] - \frac{e}{c}[\mathbf{B}_2 \times \mathbf{r}_2]. \quad (12)$$

The existence of the integral (12) makes it possible to reduce the number of independent variables of the problem. For this we express the kinematic momentum $\mathbf{\Pi}_2$ of the heavy particle in terms of the momentum $\mathbf{P}$ and the relative coordinates $x \equiv X_1 - x_2$ and $y \equiv Y_1 - y_2$. We note that $[x, y] = -il_0^2$.

Using expressions (12) and (10), we find

$$\Pi_{2x} = P_x + \frac{\hbar}{l_0^2}y \quad \text{and} \quad \Pi_{2y} = P_y - \frac{\hbar}{l_0^2}x. \quad (13)$$

Substituting (9), (11), and (13) into (1), we obtain the desired representation for the Hamiltonian of the system:

$$H = \frac{[P_x + (\hbar/l_0^2)y]^2}{2m_2} + \frac{[P_y - (\hbar/l_0^2)x]^2}{2m_2} + \frac{e^2}{2\pi}$$

$$\times \int d^2k \frac{e^{-|k|d}}{|k|} e^{-|k|^2 l_0^2/4} e^{ik_x x + ik_y y} + eE_x x + eE_y y. \quad (14)$$

Expression (14) is the starting point for studying the states of a pair of carriers of the same sign in a two-layer system in crossed fields of the given type under condition

(6). Equation (14) can be rewritten in a different form by introducing a pair of creation and annihilation operators b^+ and b, respectively:

$$b=\frac{x-iy}{\sqrt{2}l_0}; \quad b^+=\frac{x+iy}{\sqrt{2}l_0}; \quad [b,b^+]=1.$$

Using operators b and b^+, we can write Hamiltonian (14) in the form

$$H=H_0+\frac{P^2}{2m_2}+V_1(\mathbf{P},\ \mathbf{E}), \tag{15}$$

where

$$H_0=\hbar\omega_2\left(b^+b+\frac{1}{2}\right)+\frac{e^2}{2\pi}\int d^2k\,\frac{e^{-|k|d}}{|k|}$$

$$\times\exp\left(-\frac{|k|^2l_0^2}{2}\right)\exp\frac{il_0\bar{k}b^+}{\sqrt{2}}\exp\frac{il_0kb}{\sqrt{2}}$$

is the Hamiltonian of a pair for $\mathbf{P}=0$ and $\mathbf{E}=0$, the spectrum of which is known (see Ref. 7):

$$V_1(\mathbf{P},\ \mathbf{E})\equiv Zb+\bar{Z}b^+ \quad\text{and}\quad Z=\frac{eEl_0}{\sqrt{2}}+\frac{i\hbar P}{\sqrt{2}l_0m_2},$$

and $E=E_x+iE_y$, $P=P_x+iP_y$.

Before turning to a calculation of the characteristics of the states of the Hamiltonian (15), let us discuss on a qualitative level the physical mechanism that, despite the Coulomb repulsion, leads to the appearance of bound states. First let the Coulomb repulsion be "turned off." Then one can write the energy of the system exactly as a function of $\mathbf{P}$, $\mathbf{E}$, and $\mathbf{B}$. The corresponding expression for the energy has the form (cf. Ref. 8)

$$E(\mathbf{P})=-\frac{Mc^2E^2}{2B^2}-\frac{c}{B^2}\mathbf{P}(\mathbf{B}\times\mathbf{E})$$

($\mathbf{B}$ and $\mathbf{E}$ should be taken in the same layer). It follows from this expression that for a fixed configuration of $\mathbf{B}$ and $\mathbf{E}$ there always exists an orientation of $\mathbf{P}$ such that with increasing $|\mathbf{P}|$ the corresponding field contribution to the energy, $-(c/B^2)\mathbf{P}\cdot(\mathbf{B}\times\mathbf{E})$ will be positive. We now "turn on" the Coulomb interaction. It follows from relation (6) that for $\mathbf{P}=M\mathbf{V}-(e/c)[\mathbf{B}\times(\mathbf{r}_1-\mathbf{r}_2)]$, and therefore near the extrema of $E(\mathbf{P})$, where $\mathbf{V}=\partial E/\partial\mathbf{P}\cong0$, the growth of $\mathbf{P}$ means a growing average distance between particles in the pair, i.e., it is accompanied by a benefit in Coulomb energy. We see that a competition arises between the energy of Coulomb repulsion and the "field energy," and that can give rise to a local minimum in $E(\mathbf{P})$.

Let us now fortify this qualitative picture with a concrete calculation of the states of the Hamiltonian (15). Here, for simplicity, we consider only the case $d=0$ (this actually means that $d\ll l_0$). We seek the ground state of (15) by a variational method, using a space of coherent states $|z\rangle$. A basic property of the states $|z\rangle$ is expressed by the relation $b|z\rangle=z|z\rangle$. We consider the dimensionless energy of the system, $\mathcal{E}=\langle z|H|z\rangle/\hbar\omega_2$. Averaging (15) over the state $|z\rangle$, we get

$$\mathcal{E}=|p|^2+(e_1+p)z+(\bar{e}_1+\bar{p})z^*+|z|^2$$

$$+v_0e^{-|z|^2/2}I_0\left(\frac{|z|^2}{2}\right). \tag{16}$$

Here we have used the notation $v_0=\sqrt{\pi/2}(e^2/l_0)/\hbar\omega_2$; $I_0(x)$ is the zeroth-order Bessel function of imaginary argument, and we have introduced the dimensionless momentum of a pair

$$p=\frac{i\hbar P}{\sqrt{2}ml_0\hbar\omega_2}$$

and the dimensionless electric field

$$e_1=\frac{el_0E}{\sqrt{2}\hbar\omega_2}.$$

We seek a minimum of expression (16) in the space of states $|z\rangle$ with respect to z and with respect to the momentum p. It is convenient to do the minimization of (16) with respect to p first. The condition $\partial\mathcal{E}/\partial\bar{p}=0$ gives the relation $p_{\min}=-z^*$, and the energy $\tilde{E}(z,z^*)\equiv\min_p\mathcal{E}$ takes the form

$$\tilde{E}=ze_1+z^*\bar{e}_1+v_0\exp\left(-\frac{|z|^2}{2}\right)I_0\left(\frac{|z|^2}{2}\right). \tag{17}$$

Now we minimize $\tilde{E}$ with respect to z. The condition $\partial\tilde{E}/\partial z^*=0$ gives the equation

$$\frac{2|e|^2}{v_0^2}=\tilde{r}\left(\frac{\partial F}{\partial\tilde{r}}\right)^2. \tag{18}$$

In (18) we have introduced the notation $\tilde{r}=|\tilde{z}|^2/2$ and $F(r)\equiv e^{-r}I_0(r)$.

Let us examine expression (18). On the right-hand side in (18) is the function $r(\partial F/\partial r)^2$, which has a single maximum at $r=r_0$ and goes to zero at $r\to0$ and $r\to\infty$. It follows that for $2|e|^2/v_0^2>r_0(\pi F/\pi r_0)^2$ Eq. (18) does not have solutions, and therefore $\mathcal{E}(p)$ is monotonic and there are no bound states in this region of parameters. This condition for the absence of bound states can be rewritten in terms of the fields applied to the system:

$$\left|\frac{E}{B}\right|>c\cdot\alpha, \tag{19}$$

where c is a numerical factor ~1, and $\alpha\equiv e^2/\hbar c$ is the fine-structure constant.

In the case when $|E/B|\leqslant c\cdot\alpha$, Eq. (18) has two solutions: r_1 and r_2 ($r_1<r_0<r_2$). It is easy to show that r_1 corresponds to a maximum of $\tilde{E}$, and r_2 to a minimum. The characteristics of the bound states are easily calculated in the case of low electric fields, when the following condition holds:

$$\left|\frac{E}{B}\right|\ll c\cdot\alpha. \tag{20}$$

Using (18), we find $\tilde{E}$ as a function of the parameter r_2 alone:

$$E_0=\tilde{E}(r_2)=v_0\left[F(r_2)-2r_2\frac{\partial F}{\partial r_2}\right]. \tag{21}$$

Since $r_2 \gg 1$ when condition (20) holds, one can solve Eq. (18) explicitly for r_2 using an asymptotic expression for the function $I_0(r)$. Let us give the result of such a calculation. The minimum of the energy $\tilde{E}$ is reached for

$$r_2 \approx \frac{v_0}{4\sqrt{\pi}|e_1|}, \qquad (22)$$

and the corresponding energy is given by

$$E_0 = \frac{\sqrt{2v_0|e_1|}}{\pi^{1/4}} \ll v_0. \qquad (23)$$

In this same approximation we find the energy maximum, E_1, which corresponds to $r_1 : E_1 \equiv \tilde{E}(r_1) \cong v_0$. Thus in low electric fields the ratio of the energy of the metastable bound states E_0 to the barrier height E_1 is

$$\frac{E_0}{E_1} = \frac{|e_1|}{v_0} \ll 1.$$

From Eq. (22) it is easy to obtain an expression for the mean square distance between particles in the pair, $\langle R^2 \rangle$:

$$\langle R^2 \rangle = \langle \bar{z} | x^2 + y^2 | \bar{z} \rangle = 2l_0^2 \left(|z|^2 + \frac{1}{2} \right) \cong 4l_0^2 r_2 = \frac{v_0 l_0^2}{|e_1|\sqrt{\pi}}$$

$$= \frac{e}{|E|}. \qquad (24)$$

Curiously, if by analogy with the magnetic length $l_0 = \sqrt{c\hbar/e|B|}$ we introduce an electric length $l_E = \sqrt{c\hbar/e|E|}$, then $\langle R^2 \rangle$ can be written in the form

$$\langle R^2 \rangle = \alpha l_E^2, \qquad (25)$$

where $\alpha = e^2/\hbar c$ is the fine-structure constant.

We also note that the value of the momentum $\mathbf{P}_0$ corresponding to the minimum of $E(\mathbf{P})$ is given, under condition (20), by the expression

$$P_0 = \frac{eB}{c} \langle R^2 \rangle^{1/2}. \qquad (26)$$

We conclude this article with a discussion of two questions of importance for all of the above analysis. The first concerns the possibility of experimentally implementing the unusual configuration of electric and magnetic fields necessary for observation of the manifestations of MBSs. Since achieving the required configuration of low electric fields in the layers is not a particularly complicated problem, the question basically reduces to the creation of an antiparallel configuration of magnetic fields perpendicular to the layers. Here it is appropriate to mention as a precedent the experimental study reported in Ref. 9, in which the transport properties of a 2D electron gas were studied in a periodic magnetic field. The periodic magnetic field, with $B_{max} \sim 1$ T, in that study was produced by depositing magnetized strips of a magnetically hard material (dysprosium) on the surface of a conducting layer. We think that a similar method of creating magnetic fields of the required strength and orientation is promising for a two-layer system as well. However, the final answer to this question still remains open.

The final question is, how does one create a state of a pair with a specified momentum $\mathbf{P}_0$ corresponding to the minimum of $\mathcal{E}_0(\mathbf{P})$? A possible answer to this question is as follows. If the necessary field configuration is created in a bounded region, then pairs with the required values of the momentum $\mathbf{P}_0$ will accumulate in that region. Indeed, pairs for which $\mathbf{P}$ differs from $\mathbf{P}_0$ have a nonzero velocity and will therefore move out of the region of interest in a microscopic time. Thus the field configuration described, among other things, plays the role of a sort of selector of carrier pairs with respect to their momenta.

[*]E-mail: shevchenko@ilt.kharkov.ua

[1] C. C. Tsuei and J. R. Kirtley, Rev. Mod. Phys. **72**, 969 (2000).
[2] V. L. Ginzburg, Usp. Fiz. Nauk **170**, 619 (2000).
[3] W. Kohn and J. M. Luttinger, Phys. Rev. Lett. **15**, 524 (1995).
[4] H. Capellmann, JETP Lett. **62**, 745 (1992).
[5] É. A. Pashitskiĭ and V. I. Pentegov, JETP Lett. **72**, 439 (2000).
[6] V. I. Belyavskiĭ and Yu. V. Kopaev, JETP Lett. **72**, 511 (2000).
[7] E. D. Vol and S. I. Shevchenko, Fiz. Nizk. Temp. **26**, 787 (2000) [Low Temp. Phys. **26**, 577 (2000)].
[8] L. P. Gor'kov and I. E. Dzyaloshinskiĭ, Zh. Éksp. Teor. Fiz. **53**, 717 (1968) [Sov. Phys. JETP **26**, 449 (1969)].
[9] P. D. Ye, D. Weiss, R. R. Garhardts, M. Seeger, K. von Klitzing, K. Ebert, and H. Nickel, Phys. Rev. Lett. **74**, 3013 (1995).

Translated by Steve Torstveit

On the magnetoresistance of the organic complexes (BEDT−TTF)$_2$MHg(SCN)$_4$

V. G. Peschansky*

B. Verkin Institute for Low Temperature Physics and Engineering, National Academy of Sciences of Ukraine, pr. Lenina 47, 61103 Kharkov, Ukraine; Kharkov National University, pl. Svobody 4, 61077 Kharkov, Ukraine

R. Atalla

Physics Department of Bir-Zeit University, P.O. Box 28, Bir-Zeit, West Bank, Israel

According to band calculations of the electron energy spectrum of the organic complexes (BEDT−TTF)$_2$MHg(SCN)$_4$, where M is one of the metals of the group K, Rb, Tl, there should be, in addition to the main group of charge carriers with a quasi-two-dimensional spectrum, a group of charge carriers with a quasi-one-dimensional spectrum [R. Rossenau *et al.*, J. Phys. (Paris) **6**, 1527 (1996)]. We consider galvanomagnetic phenomena in quasi-two-dimensional conductors with a multisheet Fermi surface, and show that it is possible to determine the degree of quasi-one-dimensionality of an additional sheet of the Fermi surface having the form of corrugated planes. © *2001 American Institute of Physics.* [DOI: 10.1063/1.1430845]

Organic charge-transfer complexes based on tetrathiafulvalene are layered structures having a metallic type of conduction with a pronounced anisotropy. The conductivity transverse to the layers is several orders of magnitude lower than that along the layers, and there is every reason to assume that the electronic energy spectrum of these organic complexes is quasi-two-dimensional.

The energy of the charge carriers in a quasi-two-dimensional conductor,

$$\varepsilon(\mathbf{p}) = \sum_{n=0}^{\infty} \varepsilon_n(p_x, p_y) \cos\left[\frac{anp_z}{\hbar} + \alpha_n(p_x, p_y)\right],$$

$$\alpha_n(p_x, p_y) = -\alpha_n(-p_x, -p_y) \tag{1}$$

is weakly dependent on the momentum projection $p_z = \mathbf{p} \cdot \mathbf{n}$ on the normal $\mathbf{n}$ to the layers, and the Fermi surface $\varepsilon(\mathbf{p}) = \varepsilon_F$ is open, with a slight corrugation along the p_z axis. Here a is the distance between layers, $\hbar$ is Planck's constant, and the function $\varepsilon_n(p_x, p_y)$ falls off with increasing number n, so that the maximum value of the function $[\varepsilon(\mathbf{p}) - \varepsilon_0(p_x, p_y)]$, which is equal to $\eta\varepsilon_F$ on the Fermi surface, is much less than the Fermi energy ε_F.

After the Shubnikov–de Haas effect was observed[1,2] in rather perfect single-crystal samples of the organic conductors (BEDT−TTF)$_2$IBr$_2$ and (BEDT−TTF)$_2$I$_3$ at low temperatures in high magnetic fields **H** of the order of 10–20 T, it became clear that the mean free path l of the charge carriers in organic layered conductors of can significantly exceed the radius of curvature r_h of the trajectories of the conduction electrons in the magnetic fields now attainable.

Quantum oscillation effects[3,4] in such samples are extremely sensitive to the form of the electron energy spectrum, and their experimental study makes it possible to solve the inverse problem of determining from experimental data the extremal closed sections of the Fermi surface by a plane $p_H = \mathbf{p} \cdot \mathbf{H}/H = \text{const}$[5,6] In essence, all the kinetic characteristics of degenerate conductors in high magnetic fields ($r_H \ll l$) are sensitive to the form of the energy spectrum of the charge carriers, and by studying them experimentally one is able to completely recover the Fermi surface, the main characteristic of the spectrum of conduction electrons. The presence of open sections of the Fermi surface by a plane $p_H = \text{const}$ leads to pronounced anisotropy of the magnetoresistance in a high magnetic field. By studying this anisotropy one can completely recover the topology of the Fermi surface.[7–9]

In quasi-two-dimensional conductors an appreciable number of charge carriers with the Fermi energy are involved in the formation of quantum oscillation effects. At low temperatures, when the temperature smearing of the Fermi distribution function of the charge carriers is much less than the distance between their quantum energy levels, and the frequency of dissipative collisions of a conduction electron, $1/\tau$, is much higher than its gyration frequency in the magnetic field, $\Omega = eH/m^*c$, the amplitude of the magnetoresistance oscillations is comparable to the part of the magnetoresistance that varies monotonically with H. Here e is the charge of the electron, m^* is its cyclotron effective mass, and c is the speed of light.

The clear manifestation of the Shubnikov–de Haas effect in the magnetoresistance of a large family of ionic–radical salts based on tetrathiafulvalene in a magnetic field $\mathbf{H} = (0, H\sin\theta, H\cos\theta)$ over a wide interval of angles θ between the vectors $\mathbf{H}$ and $\mathbf{n}$ (see the review articels[10,11] and the literature cited therein) attests to the fact that at least one sheet of the Fermi surface is a slightly corrugated cylinder, the plane sections $p_H = \text{const}$ of which at θ not equal to $\pi/2$ are closed.

It is not hard to show that the contribution to the components of the conductivity tensor σ_{ik} (which in the Ohm's-law approximation relates the current density $\mathbf{j}$ to the electric field E_i) from a group of charge carriers whose states belong

to a sheet of the Fermi surface having the form of a slightly corrugated cylinder will, in the case $\gamma = 1/\Omega\tau \ll 1$ and $\eta\tan\theta \ll 1$ have the form

$$\sigma_{ik} = \begin{cases} \gamma^2 a_{xx} & \gamma a_{xy} & \gamma\eta^2 a_{xz} \\ \gamma a_{yx} & \gamma^2 a_{yy} + \sigma_{zz}\tan^2\theta & \gamma\eta^2 a_{yz} + \sigma_{zz}\tan\theta, \\ \gamma\eta^2 a_{zx} & \gamma\eta^2 a_{zy} + \sigma_{zz}\tan\theta & \sigma_{zz} \end{cases} \tag{2}$$

where the matrix components a_{ik} are of the same order of magnitude as σ_0, the conductivity along the layers in the absence of magnetic field.

The appreciable resistance to electrical current flowing transverse to the layers is due to the slow drift of charge carriers along the normal to the layers, with a velocity

$$v_z = -\sum_{n=1}^{\infty} \frac{an}{\hbar}\varepsilon_n(p_x,p_y)\sin\left[\frac{anp_z}{\hbar} + \alpha_n(p_x,p_y)\right], \tag{3}$$

so that σ_{zz} is proportional to η^2 at least.

The model of the Fermi surface in the form a slightly corrugated cylinder is in quite good agreement with the experimental results on the magnetoresistance of a large family of tetrathiafulvalene salts. However, the Fermi surface of layered conductors can also be of a multisheet character. Besides the corrugated cylinder there can also be sheets in the form of corrugated planes with a slight corrugation along the p_z axis. For example, the Fermi surface of the salts $(\text{BEDT}-\text{TTF})_2\text{MHg(SCN)}_4$, where M is one of the metals of the group K, Rb, Tl, according to band calculations of the electron energy spectrum,[12] contains two quasi-one-dimensional sheets in addition to the slightly corrugated cylinder. To ascertain how well these calculations agree with the experimentally observed dependence of the magnetoresistance on the strength of a high magnetic field $\mathbf{H} = (0, H\sin\theta, H\cos\theta)$, let us examine the galvanomagnetic effects in quasi-two-dimensional conductors whose Fermi surface consists of a slightly corrugated cylinder and two slightly corrugated planes, with the normal to their tangent plane deviating from the p_x axis by an angle φ. We will not specify the form of these planes but will assume that they have an arbitrary corrugation in the p_xp_y plane, while the corrugation along the p_z axis will be assumed to be of the same weakness as for the corrugated-cylinder sheet of the Fermi surface.

When there are several groups of charge carriers, they all contribute to the electrical current, so that the total conductivity is the sum of the conductivity of each group of conduction electrons:

$$\sigma_{jk} = \sigma_{jk}^{(1)} + \sigma_{ik}^{(2)}, \tag{4}$$

where $\sigma_{ik}^{(1)}$ is the contribution to the conductivity from charge carriers whose states belong to the slightly corrugated plane sheets of the Fermi surface, and $\sigma_{ik}^{(2)}$ is the contribution from conduction electrons belonging to the slightly corrugated cylinder.

Whereas open sections of the corrugated cylinder are possible only for $\theta = \pi/2$, in the presence of an additional sheet of the Fermi surface in the form of a corrugated plane

the open electron trajectories $\varepsilon = \text{const}$ and $p_H = \mathbf{p}\cdot\mathbf{H}/H = \text{const}$ appear for any direction of the magnetic field. The charge carriers whose state belongs to the corrugated-plane sheets of the Fermi surface undergo drift in the plane orthogonal to the magnetic field, and the transverse resistance, when the current density $\mathbf{j}$ and magnetic field $\mathbf{H}$ are mutually orthogonal, is sharply anisotropic. Thus if the resistance to current flow along the normal to the layers, for example, is observed to increase quadratically with $\mathbf{H}$ for different orientations of the magnetic field in the case $r_H \ll l$, it can be taken as evidence of the existence of a sheet of the Fermi surface in the form of a corrugated plane.

The conduction electrons along open trajectories in momentum space cannot be displaced a significant distance along the normal to the plane $p_x\cos\varphi + p_y\sin\varphi = 0$. After averaging the equation of motion of the charge

$$\partial\mathbf{p}/\partial t = \frac{e}{c}(\mathbf{v}\times\mathbf{H}) \tag{5}$$

over a sufficiently long time interval, greatly exceeding $T \cong r_H/v_F$, where v_F is the characteristic Fermi velocity of the electrons in the plane of the layers, we obtain the following relation:

$$(\bar{v}_x\cos\varphi + \bar{v}_y\sin\varphi)\cos\theta = \bar{v}_z\sin\varphi\sin\theta, \tag{6}$$

which specifies the plane of all possible drifts of the charge carriers in real space. In the coordinate system (x_1, x_2, x_3) with unit vectors

$$\mathbf{e}_1 = \frac{1}{[1-\cos^2\varphi\sin^2\theta]^{1/2}}(\cos\varphi\cos\theta, \sin\varphi\cos\theta,$$
$$-\sin\varphi\sin\theta),$$

$$\mathbf{e}_2 = (\mathbf{e}_3\times\mathbf{e}_1), \quad \mathbf{e}_3 = \mathbf{H}/H \tag{7}$$

the matrix $\sigma_{ik}^{(1)}$ has the following asymptotic expression for $\gamma \ll 1$ and $\eta \ll \cos\theta$:

$$\sigma_{ik}^{(1)} = \begin{pmatrix} \gamma^2 a_{11}' & \gamma a_{12}' & \gamma a_{13}' \\ \gamma a_{21}' & a_{22}' & a_{23}' \\ \gamma a_{31}' & a_{32}' & a_{33}' \end{pmatrix}, \tag{8}$$

where the matrix components a_{ik}' in an extremely high magnetic field, when γ approaches zero, does not depend on γ, while $(a_{22}'a_{33}' - a_{23}'a_{32}')$ is always greater than zero by virtue of the Schwarz inequality.

In this same coordinate system the matrix $\sigma_{ik}^{(2)}$ at θ substantially different from $\pi/2$ will have only one nonzero component, $\sigma_{33}^{(2)}$, as γ approaches zero.

Straightforward calculations for $\eta \ll \cos\theta$ and $\gamma_0 \ll \cos\theta$ yield the asymptotic expressions for the resistance along and transverse to the layers:

$$\rho_{xx} = \frac{\sigma_1\sin^2\varphi + \gamma_0^2\sigma_0}{\gamma_0^2\sigma_0(\sigma_0 + \sigma_1)}; \tag{9}$$

$$\rho_{yy} = \frac{\sigma_1\cos^2\varphi + \gamma_0^2\sigma_0}{\gamma_0^2\sigma_0(\sigma_0 + \sigma_1)}; $$

$$\rho_{zz} = \frac{1}{\sigma_{zz}} + \frac{\sigma_1\cos^2\varphi\sin^2\theta}{\sigma_0\gamma_0^2}, \tag{10}$$

where σ_1 is the largest contribution to the conductivity along the layers at $H=0$ from the charge carriers whose states lie on an open sheet of the Fermi surface having the form of a corrugated plane; $\sigma_{zz} = \sigma_{zz}^{(1)} + \sigma_{zz}^{(2)}$; $\gamma_0 = 1/\Omega_0\tau$, and Ω_0 is the gyration frequency of an electron in the magnetic field for $\theta=0$. In formula (9), which describes the anisotropy of the resistance in the plane of the layers, and in the last term of formula (10), we have dropped numerical factors of the order of unity which depend on the specific form of the electron energy spectrum. It is easy to see that for $\gamma_0 \cong \eta$ it is extremely important to take the second term in formula (10) into account.

The resistance to current transverse to the layers, ρ_{zz}, increases without bound as H increases, even when the magnetic field deviates from the plane of the layers, and only for $\varphi = \pi/2$ and θ quite different from $\pi/2$ does ρ_{zz} reach saturation in a high magnetic field and become equal to $1/\sigma_{zz}$ to good accuracy. In this case, for certain orientations of the magnetic field not only $\sigma_{zz}^{(2)}$ but also $\sigma_{zz}^{(1)}$ will decrease sharply. Here the positions of the sharp peaks in the angle dependence of $\sigma_{zz}^{(1)}$ and $\sigma_{zz}^{(2)}$, as a rule, do not coincide.

For φ much different from $\pi/2$, when $|\varphi - \pi/2| \gg \gamma$, sharp peaks in the dependence of ρ_{zz} on θ occur against the background of a rather large growth of the magnetoresistance of the organic conductors $(BEDT-TTF)_2MHg(SCN)_4$, but they can nevertheless be brought out by differentiating the function $\rho_{zz}(\theta)$ with respect to θ.

In the case of a quasi-one-dimensional character of the energy spectrum of an additional group of charge carriers, the sharp peaks in the angle dependence of the resistivity transverse to the layers are due mainly to conduction electrons having a quasi-two-dimensional energy spectrum, whose states belong to the corrugated-cylinder sheet of the Fermi surface. This is because in a magnetic field satisfying the condition $\max\{\eta, \eta_1\} \ll \gamma_0 \ll 1$, where η_1 is the degree of corrugation of the quasi-one-dimensional sheet of the Fermi surface in the plane $p_x p_y$, the motion of the electrons with the quasi-one-dimensional energy spectrum in momentum space takes place at an almost constant velocity, and $\sigma_{zz}^{(1)}$ in the leading approximation in the parameter η^2 is proportional to $\sin^2\theta$, while the terms that oscillate with $\tan\theta$ appear in the next-higher approximations in the low-dimensionality parameters of their energy spectrum, η and η_1, only in the region of higher magnetic fields, when $\gamma_0 \lesssim \max\{\eta, \eta_1\}$. In this case $\sigma_{zz}^{(1)}$ is a small correction to $\sigma_{zz}^{(2)}$

except for those orientations of the magnetic field for which $\sigma_{zz}^{(2)}(\sigma_c)$ takes a minimal value. The angular oscillations of $\sigma_{zz}^{(2)}$ have been studied in detail theoretically in the case of an extremely simple model of the Fermi surface[13] and also under the most general assumptions about the form of the quasi-two-dimensional electron energy spectrum.[14–19]

Thus by studying the angle dependence of the resistance to current transverse to the layers in the organic charge-transfer complexes $(BEDT-TTF)_2MHg(SCN)_4$ over a wide range of magnetic fields, one can reliably determine the degree of quasi-one-dimensionality of the additional, corrugated-plane sheets of the Fermi surface.

*E-mail: vpeschansky@ilt.kharkov.ua

[1] M. V. Kartsovnik, V. N. Laukhin, V. I. Nizhankovskiǐ, and A. A. Ignat'ev, JETP Lett. **47**, 363 (1988).
[2] M. V. Kartsovnik, P. A. Kononovich, V. N. Laukhin, and I. F. Shchegolev, JETP Lett. **48**, 541 (1988).
[3] L. V. Schubnikov and W. J. de Haas, Leiden Commun. **207**, 210 (1930).
[4] W. J. de Haas and P. M. van Alphen, Proc. Acad. Sci. (Amsterdam) **33**, 1106 (1930).
[5] L. Onsager, Philos. Mag. **43**, 1006 (1952).
[6] I. M. Lifshits and A. M. Kosevich, Zh. Éksp. Teor. Fiz. **29**, 730 (1955) [Sov. Phys. JETP **2**, 636 (1956)].
[7] I. M. Lifshits and V. G. Peschanskiǐ, Zh. Éksp. Teor. Fiz. **35**, 1251 (1958) [Sov. Phys. JETP **8**, 875 (1959)].
[8] I. M. Lifshits and V. G. Peschanskiǐ, Zh. Éksp. Teor. Fiz. **38**, 188 (1960) [Sov. Phys. JETP **11**, 137 (1960)].
[9] S. P. Novikov and A. Ya. Mal'tsev, Usp. Fiz. Nauk **168**, 249 (1998).
[10] J. Wosnitza, *Fermi Surfaces of Low-Dimensional Organic Metals and Superconductors*, Vol. 134 of Springer Tracts in Modern Physics (Springer-Verlag, New York, 1996).
[11] J. Singelton, "Studies of quasi-two-dimensional organic conductors based on BEDT–TTF using high magnetic fields," Rep. Prog. Phys. **63**, 1111 (2000).
[12] R. Rossenau, M. L. Doublet, E. Canadell, R. P. Shibaeva, R. P. Rozenberg, N. D. Kushch, and E. B. Jagubskii, J. Phys. (France) **6**, 1527 (1996).
[13] K. Yamagji, J. Phys. Soc. Jpn. **58**, 1520 (1989).
[14] V. G. Peschansky, J. A. Roldán López, and Toji Gnado Yao, J. Phys. (France) **1**, 1469 (1991).
[15] V. G. Peschansky, Phys. Rep. **288**, 305 (1997).
[16] V. G. Peschansky, Fiz. Nizk. Temp. **23**, 47 (1997) [Low Temp. Phys. **23**, 35 (1997)].
[17] V. G. Peschanskiǐ, Zh. Éksp. Teor. Fiz. **112**, 618 (1997) [JETP **85**, 337, 447 (1997)].
[18] V. G. Peschansky and M. V. Kartsovnik, Phys. Rev. B **60**, 11207 (1999).
[19] V. G. Peschansky and M. V. Kartsovnik, J. Low Temp. Phys. **117**, 1717 (1999).

Translated by Steve Torstveit

Microwave second-harmonic generation and point-contact spectroscopy of Ni−Nb metallic glasses

O. P. Balkashin* and I. K. Yanson

B. Verkin Institute for Low Temperature Physics and Engineering National Academy of Sciences of Ukraine, pr. Lenina 47, 61103 Kharkov, Ukraine

A. Halbritter and G. Mihály

Institute of Physics, Budapest University of Technology and Economics, Budafoki út 8, H-1111 Budapest, Hungary

The point-contact spectra (the energy dependence of the amplitude of the second harmonic of the modulation current) of contacts of Ni_xNb_{1-x} metallic glasses are measured at audio (3726 Hz) and microwave (9.5 GHz) frequencies. It is established for the first time in rf dynamic experiments that the low-energy spectral feature due the scattering of electrons on two-level systems (TLSs) in the contact is observed at microwave frequencies as well. This is direct evidence of the existence of a fast relaxation process in the contacts, with a characteristic time $\tau \ll 10^{-10}$ s. There is also a small contribution from slower scattering processes. It is found that the videodetection signal contains a component due to a steady-state nonequilibrium occupation of the states of the TLSs under microwave irradiation. The coupling efficiency of the contact with the waveguide and rf receiver is estimated to be 5–7%. A slight minimum of the resistance at zero voltage observed for some of the contacts is attributed to superconducting fluctuations of the order parameter at a temperature $T \sim 2.3 T_c$. © *2001 American Institute of Physics.* [DOI: 10.1063/1.1430846]

INTRODUCTION

The spatial disorder in the arrangement of atoms in metallic glasses, which are now used in many important technical applications, gives them some specific thermodynamic and kinetic properties in the both the normal and superconducting states at low temperatures. These properties are explained by the presence of a special kind of structural defects in amorphous materials—tunneling two-level systems (TLSs), which are modeled for an individual atom or group of atoms by a double-well potential.[1] Under the influence of an external perturbation, a tunneling transition occurs in the TLSs between the two possible configurations, with characteristic energies $\delta \sim 0.1 - 1$ meV. The scattering of electrons on TLSs in bulk samples leads to a logarithmic temperature dependence of the resistivity, with a negative temperature coefficient.[2] In point contacts such scattering gives rise to features on the conductivity at low biases $eV \to 0$.[3,4] There are two existing theoretical models describing the interaction of conduction electrons with TLSs which are capable of explaining the the appearance of low-energy anomalies in the point-contact spectra. In Refs. 5 and 6 an almost symmetric double-well potential of the TLSs was used in developing a mechanism of nonmagnetic two-channel Kondo scattering; this mechanism leads to a logarithmic energy (temperature) dependence of the resistivity of the metal. In Refs. 7 and 8 an alternative model was proposed that considered both inelastic and elastic scattering of electrons on asymmetric TLSs in point contacts. As was shown in Ref. 8, because of the difference in the elastic scattering cross sections of electrons on TLSs found in two different configurations, it is possible to

do elastic point-contact spectroscopy of the occupations of the TLSs. Both of these scattering mechanisms give rise to low-energy features in the point-contact spectra. However, the proposed electron scattering mechanisms have substantially different characteristic relaxation times: $\tau \sim 10^{-11}$ s for the nonmagnetic Kondo scattering, and $10^{-3} - 10^{-8}$ s for the TLS occupation spectroscopy. This difference in characteristic times makes it possible to distinguish the contributions to the point-contact spectrum from the different scattering mechanisms by doing rf experiments.

In Refs. 9 and 10 the energy dependence of the videoresponse signal upon rectification of an alternating microwave modulation current by point contacts of metallic glasses of various compositions, including Ni_xNb_{1-x}. However, in quasistatic measurements of this sort there is a noticeable contribution to the measured signal from the steady-state modification of the current-voltage (I–V) characteristic by the microwave radiation. More-correct results can be obtained in dynamic experiments investigating the generation of the second harmonic of rf pump radiation.

The goal of the present study was to compare directly the energy dependence of the second-harmonic amplitudes in the case of pumping at audio ($\omega_1/2\pi = 1863$ Hz) and microwave ($\omega_2/2\pi = 4.75$ GHz) frequencies.

The energy of the microwave photons used in the experiments, $\hbar \omega_2 = 0.02$ meV, was much less than the energy smearing ($\Delta \sim 5$ meV) of the investigated spectral feature of the I–V characteristic in the region of low voltages across the contact. Therefore, for interpreting the results one can use the formulas for the classical low-frequency limit.[11] If

the contact is placed in a microwave field of frequency ω, then an rf alternating current is induced between the massive "banks" of the contact. Then the total current through the contact will be $I = I_0 + i_\omega \cos \omega t$, where I_0 is a dc bias transport current. In the small-signal limit $i_\omega \ll I_0$ the dependence of the amplitude of the second harmonic of the modulation current on the dc voltage V_0 across the contact is proportional to the second derivative of the I–V characteristic:[12,13]

$$V_{2\omega}(V_0) = \frac{1}{4\sqrt{2}} \frac{d^2 V}{dI^2}(V_0) i_\omega^2. \tag{1}$$

The amplitude V_d of the videodetection signal in the case of rectification of an rf alternating current at a nonlinear feature of the I–V characteristic is determined in an analogous way.[14]

Thus the signal amplitudes in both the rf and audiofrequency experiments are determined by the second derivatives d^2V/dI^2 measured at the corresponding frequencies (see Eq. (1)). A direct comparison of the signals gives direct information about possible changes of the degree of nonlinearity of the I–V characteristics at different frequencies and thereby permits identification of the electron scattering processes occurring in the point contact.

EXPERIMENTAL METHODS

Point contacts were made directly in liquid helium by touching the ends of segments of 20-μm thick ribbons of Ni–Nb metallic glasses of various compositions. The electrodes could be moved in two mutually perpendicular directions by means of differential screws. The sample holder was a length of rectangular waveguide with a cross section of 23×10 mm with two holes 6 mm in diameter into which the electrodes of the point contact were inserted. A movable short-circuiting plunger in the lower part of the holder permitted changing the electrodynamic coupling of the contact with the waveguide. Several different constructions of the holder, with different orientations of the electrodes relative to the walls of the waveguide, were used in different experiments, but the amplitudes of the measured signals of the microwave second harmonic were practically the same for all of the orientations.

Pump radiation from a klystron oscillator at a frequency $\omega_2/2\pi = 4.75$ GHz was fed to the contact via a coaxial cable with a coupling loop placed close to one of the electrodes of the point contact. A ferrite isolator (a rejection filter with an overall attenuation of ~ 30 dB) was placed in the coaxial line, preventing the klystron radiation at the second harmonic frequency from reaching the contact. The pump power level P_0 was monitored by a thermoelectric wattmeter mounted at the output of the klystron oscillator. The radiation generated by the contact at the second harmonic frequency $2\omega_2/2\pi = 9.5$ GHz was fed via a standard three-centimeter waveguide to a superheterodyne receiver having a sensitivity of about 0.5×10^{-14} W/Hz. The waveguide, which was a cutoff waveguide for frequency ω_2, prevented radiation at the pump frequency from reaching the input of the receiver. A cavity filter and a ferrite low-pass filter at the input of the superheterodyne receiver selected a pure monochromatic signal at the frequency $2\omega_2$, which was fed to a balanced

mixer, where the intermediate-frequency signal $\omega_{\mathrm{if}} = 2\omega_2 - \omega_{l_0} = 60$ MHz was produced upon mixing of the input radiation with the heterodyne signal. After amplification, the intermediate-frequency signal was sent to a videodetector. The voltage at the output of the detector was directly proportional (with an error of $\sim 1\%$) to the power of the rf radiation from the point contact at the input of the receiver. The pump radiation fed to the point contact was amplitude-modulated at a frequency of 2433 Hz. The signal at this same frequency 2433 Hz at the output of the videodetector was amplified by a low-frequency selective amplifier with a phase detector and was registered by an XY recorder as a function of the voltage across the point contact. A typical value of the registered power of the microwave second harmonic signal radiated by the contact was $(1-5) \times 10^{-14}$ W. The second-harmonic signal vanished completely when contact was broken by separating the electrodes or when the pump radiation was turned off.

In experiments on videodetection (rectification) the high-frequency radiation of the rf pump field incident on the contact was interrupted at a frequency of 2433 Hz. The change in the dc voltage across the contact, the videoresponse signal V_d (the difference between the voltages across the contact in the presence and absence of irradiation), was recorded in a synchronous detection scheme as a function of the dc bias voltage applied to the contact.

The point-contact spectra (the amplitudes of the second derivative of the I–V characteristic) at the audiofrequency $2\omega_1/2\pi = 3726$ Hz was measured in a standard synchronous detection scheme.[13] All of the measurements were made at a temperature of 4.2 K.

PRESENTATION AND DISCUSSION OF THE MAIN EXPERIMENTAL RESULTS

Ni$_{59}$Nb$_{41}$ point contacts

A typical point-contact spectrum measured at the audiofrequency 3726 Hz in the absence of the rf pump radiation for contacts of metallic glass of this composition is shown by curve *1* in Fig. 1. The negative values of the second-
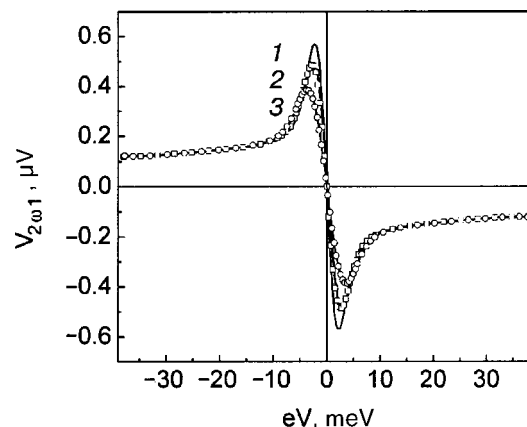
FIG. 1. Point-contact spectra of Ni$_{59}$Nb$_{41}$, measured at audiofrequency (3726 Hz) without microwave irradiation (*1*) and under irradiation by a pump power $P_0 = 2.4 \times 10^{-5}$ (*2*) and 5.5×10^{-5} W (*3*). The discrete symbols show the values calculated according to formula (2) for low-frequency modulation amplitudes $V_{\omega 1} = 2.6$ ($\square$) and 4.2 mV ($\bigcirc$). The contact resistance $R = 28$ Ω.

harmonic voltage $V_{2\omega}$ and, hence, the negative value of the second derivative of the I–V characteristic at low voltages ($V>0$) attest to the growth of the contact resistance with decreasing excess energy of the conduction electrons, which is set by the dc voltage source. This sort of behavior of the resistance is typical for electron scattering on TLSs. The amplitude of the low-frequency modulation in these measurements, $V_{\omega 1}=0.35$ mV, was an order of magnitude less than the half-width of the feature in the point-contact spectrum at energies $eV\sim 2$ meV. Consequently, one can neglect the modulational broadening of the spectral feature and assume that curve *1* in Fig. 1 is the spectral line with its natural width.

In making the measurements of this contact at high frequencies it was found that for reliable and accurate detection of the radiation of the point contact at the second harmonic it is necessary to irradiate the contact at a much higher level of microwave pump power. This is because, unlike the case of the low-frequency circuit, here the coupling coefficient of the contact with the waveguide is substantially less than unity, and only a small fraction of the rf radiation of the contact is registered by the receiver. The cause of the mismatch may be the holes in the walls of the waveguide with the electrodes passing through them; these may act as antennas to extract radiation to the outside of the waveguide. In addition, it must be considered that a certain fraction of the radiation from the contact is reflected from irregularities of the waveguide section and is not registered by the receiver. The necessary increase in the rf pump power caused the recorded spectral feature to be smeared and shifted to higher energies. An estimate of the coupling coefficient will be given below.

In order to get a more correct comparison of the results of the low- and high-frequency experiments, we measured the amplitude of the second-harmonic signal at low frequency with the contact irradiated at the same levels of rf pumping as was used when recording the second-harmonic amplitude at high frequency. In Fig. 1 the continuous curves *2* and *3* show the two low-frequency curves $V_{2\omega 1}(eV_0)$ measured under microwave irradiation of the contact at a frequency of 4.75 GHz for two values of the rf power P_0: 2.4×10^{-5} (*2*) and 5.5×10^{-5} W (*3*). The decrease of the amplitude and the broadening of the feature of the point-contact spectrum with increasing power of the high-frequency irradiation are clearly discernable in the figure.

The value of the alternating voltage $V_{\omega 2}$ induced across the contact by the rf radiation can be estimated by comparing the experimental curves with the dependence of the modulational smearing calculated according to the theory of point-contact spectroscopy, with the optimal values chosen for the modulation amplitude. These calculation were done using the formula

$$F''(V_0)=\int_{-V_\omega}^{V_\omega} f''(V_0+v_\omega)\Phi(v_\omega)dv_\omega, \tag{2}$$

where f'' is the true second derivative of the I–V characteristic, F'' is the second derivative at a finite value of the modulation amplitude V_ω, and V_0 and v_ω are the dc and ac voltages across the contact. The modulational smearing function $\Phi(v_\omega)$ is given by the expression

$$\Phi(v_\omega)=\frac{8}{3\pi}\frac{1}{v_\omega^4}(V_\omega^2-v_\omega^2). \tag{3}$$

The results of the calculation for two values of the modulation amplitude V_ω (2.6 and 4.7 mV) are shown by the discrete symbols in Fig. 1 and are in good agreement with the experimental curves *2* and *3*.

Knowing the value of the pump power and the amplitude of the alternating voltage induced across the contact, one can estimate the coupling coefficient of the contact with the co-axial line. The average power absorbed by the contact at 100% coupling with the transmission line is given by $P_0=V_{\omega 2}^2/2R$, where $V_{\omega 2}$ is the value of the ac voltage induced by the rf field, and R is the contact resistance. Using the experimental parameters for this contact and the effective calculated values of V_ω, we obtain a value of around 6% for the coupling coefficient of the contact with the coaxial line.

Figure 2 shows the second-harmonic voltage for the cases of low-frequency (solid curves *1* and *2*) and microwave (dashed curves *3* and *4*) modulation for two levels of the rf pump power.[1] These voltages were calculated according to the formula $P_{rf}=V_{2\omega 2}^2/2R$ from the experimental curves of $P_{2\omega 2}(eV)$ of the output signal of the rf receiver as a function of the bias across the contact (see the inset in Fig. 2). The error of measurement of the rf power shown in the inset is determined from the width of the noise trace at the output of the receiver. We emphasize once again that the low-frequency curves were measured at the same pump power as was used when recording the microwave second harmonic. The dotted curves in Fig. 2 show the empirical curves of the background signal which were chosen so as to agree with the experimental curves in the high-energy region. As we see from the figure, the curves of the energy dependence of the
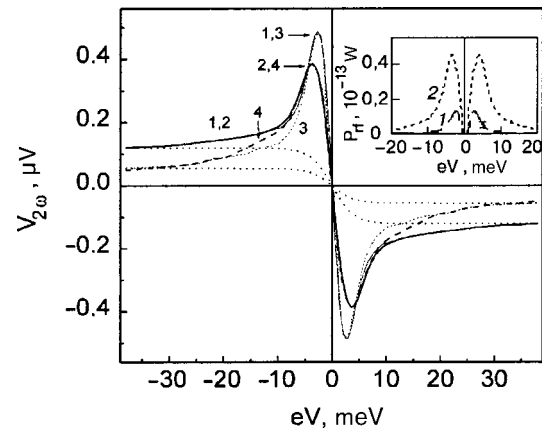
FIG. 2. Energy dependence of the amplitude of the second-harmonic signal of a $Ni_{59}Nb_{41}$ contact, measured at audio (3726 Hz) and microwave (9.5 GHz) frequencies. The measurement regimes were as follows: *1* (the light solid curve)–modulation frequency $\omega_1/2\pi=1863$ Hz, modulation amplitude $V_{\omega 1}=0.35$ μV, the power of the microwave pump radiation $P_0=2.4\times10^{-5}$ W; *2* (heavy solid curve)—$\omega_1/2\pi=1863$ Hz, $P_0=5.5\times10^{-5}$ W; *3*—(light dashed curve)—modulation frequency $\omega_2/2\pi=4.75$ GHz, $P_0=2.4\times10^{-5}$ W; *4*—(heavy dashed curve) $\omega_2/2\pi=4.75$ GHz, $P_0=5.5\times10^{-5}$ W. The dotted curves show the empirically chosen background level for the two values of the microwave pump power. Inset: The energy dependence of the output signal of the microwave receiver for two levels of the pump power, $P_0=2.4\times10^{-5}$ (*1*) and 5.5×10^{-5} W (*2*). The indicated error shows the width of the noise trace at the output of the microwave receiver. The resistance of the point contact was $R=28$ Ω.

1024   Low Temp. Phys. **27** (12), December 2001

Balkashin *et al.*

second-harmonic voltages $V_{2\omega}(eV)$ for the low and high frequencies have practically the same shape and intensity. This similarity of the curves suggests that the relaxation processes occurring in the point contact through the interaction of electrons with TLSs are quite fast even at a frequency of 9.5 GHz and have a characteristic relaxation time $\tau \ll 10^{-10}$ s.

It should be noted that the level of the background signal is reduced by nearly one-half for the high-frequency measurements. This cannot be due to thermal effects, since the background was not observed to depend on the bias voltage. The lowering of the background in the high-frequency measurements attests to the presence of a slow relaxation mechanism in the contact. This process could be the relaxation of asymmetric TLSs, which was considered in Ref. 8. Of course, in the high-frequency measurements at frequencies $\omega\tau \gg 1$ this mechanism will not contribute to the measured signal.

Figure 3 shows the curves of the contribution to the differential resistance of a point contact from processes of electron scattering on TLSs. The curves were obtained by numerically integrating curves *1* and *3* in Fig. 2 after subtraction of the background signal. The discrete symbols show the functional dependence of the calculated resistance for the given contact:

$$R^*(eV) \propto A - B \ln\left[\left(\frac{eV}{\delta}\right)^2 + 1\right] A, \quad B = \text{const.} \quad (4)$$

This form of the energy (temperature) dependence of the resistance is typical of metallic glasses.[2,15] The good agreement between the experimental curves in Fig. 3 and the calculated dependence of the form $R(eV) \propto -\ln(eV)$ allows us to identify the resistance feature at low biases across the contact unambiguously as being a manifestation of the scattering of electrons on two-level systems.

It is important to analyze how the measured characteristics in the high-frequency measurements would be affected by the possible heating of the contact by the transport current and rf irradiation. It was established experimentally in Ref. 16 that point contacts of pure nickel, Ni–Ni, with a diameter $d \approx 25$ nm have a characteristic thermal relaxation frequency $\omega_T/2\pi \sim 10^9$ Hz. Consequently, the thermal relaxation frequency ω_T can be estimated as $\sim 10^8$ Hz for a contact of the
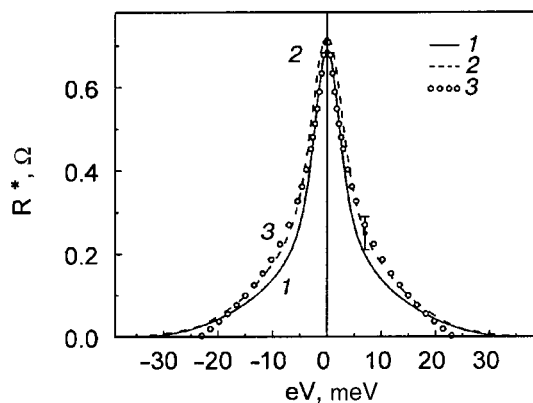

FIG. 3. The contribution R^* to the differential resistance of a point contact due to the scattering of electrons on TLSs, measured at audio (*1*) and microwave (*2*) frequencies. The dashed curve *3* was calculated according to formula (4).

metallic glass $Ni_{59}Nb_{41}$ with a diameter $d \approx 57$ nm [$d = \rho/R$ (Ref. 13), where $\rho = 160 \mu\Omega \cdot$cm is the resistivity of the material,[4] and $R = 28 \Omega$ is the resistance of the given contact]. It follows from this estimate that the microwave second-harmonic frequency $2\omega_2$ at which the measurements were made is much greater than ω_T. In that case, for $\omega \gg \omega_T$ the second-harmonic signal should vanish, and the amplitude of the videodetection signal of the rf radiation incident on the contact should be proportional to the first derivative and not to the second derivative of the I–V characteristic.[16] This is contradicted by the picture seen in Fig. 2, where the measured curves of $V_{2\omega2}(eV)$ practically coincide for the low- and high-frequency measurements, attesting to the absence of heating of the contact in our experiments.

To estimate the matching coefficient of the contact with the waveguide and the rf receiver we introduce a nonlinearity parameter of the I–V characteristics: $S = (d^2V/dI^2)/(dV/dI)^2$ or, in terms of the corresponding harmonic voltages,[13] $S = 2\sqrt{2}V_{2\omega}/V_\omega^2$. For low-frequency modulation the nonlinearity parameter at the extremal points at $eV \sim 2$ meV (Fig. 1) is estimated as $S = 10$ V^{-1} for that contact in the absence of the rf pump radiation. As the irradiation intensity increases, the value of S decreases to 8.5 and 6.7 V^{-1} for the two power levels used in the experiments. These values of S are close to those for point contacts of pure metals.[17] The overall form of the curves of the first- and second-harmonic amplitudes change only slightly for the high-frequency measurements (see Figs. 2 and 3), and we can therefore assume that $S = 8.5$ and 6.7 V^{-1} at high frequencies as well. Then, using the values of V_ω calculated above and the experimental data for $V_{2\omega2}(eV)$, we can estimate the ratio of the experimental and calculated amplitudes of the microwave second harmonic. This ratio comes out to be ~ 0.07, i.e., the coupling coefficient of the contact with the waveguide section has a value of around 7%. An alternative estimate of the coupling constant, using expression (1) with the experimental results in Figs. 1 and 2 and the amplitudes of the low- and high-frequency modulations, gives a value of 5%. This weak coupling of the contact with the rf receiver justifies the need for applying relatively high pump powers in our experiments when recording the signals of the microwave second harmonic. Here, as was established in a special experiment, the general features of the energy dependence of the output signal of the rf receiver are preserved as the pump power is increased (see Fig. 4). Only at very high power levels does some asymmetry of the signal appear (the upper two curves in Fig. 4), apparently due to the contribution from nonlinear processes in the massive electrodes, which have a high resistivity, and to their asymmetric position in the rf field. The sharp decrease in the amplitude at large biases (shown by the arrows in Fig. 4) is due to the fact that the rf irradiation was turned off in order to accurately fix the zero level of the signal.

$Ni_{44}Nb_{56}$ point contacts

The experimental results for the majority of the metallic-glass contacts of this composition were similar to the data presented above for $Ni_{59}Nb_{41}$. The curves for one of the contacts, with a resistance $R = 11 \Omega$, are shown in Fig. 5.
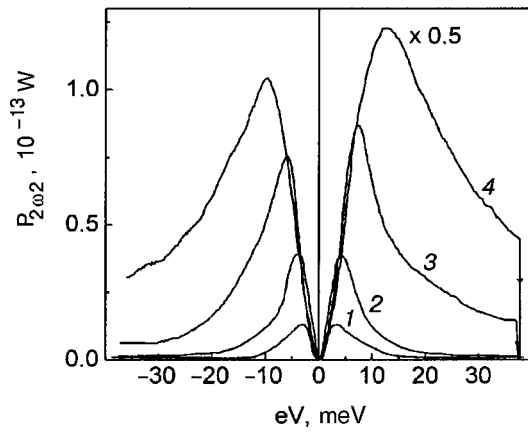
FIG. 4. Dependence of the output signal amplitude of the rf detector on the bias voltage across the contact for different pump powers P_0, 10^{-5} W: 2.5 (*1*), 7.1 (*2*), 16 (*3*), 45 (*4*). The contact resistance $R = 26\,\Omega$.

The nonlinearity of the I–V characteristic of this particular contact was less than for the samples in Figs. 1, 2, and 3, and therefore the curves in Fig. 5 were measured at a high level of both the low-frequency modulation and the rf pump power. All three of the experimental curves $V_{2\omega 1}(eV)$, $V_d(eV)$, and $V_{2\omega 2}(eV)$ were obtained at the same rf pump power $P_0 = 10^{-4}$ W. The high-frequency curves for the videodetection signal $V_d(eV)$ and the microwave second-harmonic voltage $V_{2\omega 2}(eV)$ were matched by a suitable choice of scale factor to the low-frequency curve at the maximum at $eV \sim 4.4$ meV. In Fig. 5 we see a noticeable difference between the amplitudes of the signals in the background region at high energies. This difference increases monotonically with increasing bias across the contact, at least up to $eV \sim 25$ meV for the two high-frequency curves. To explain this difference in the signal amplitudes we can conjecture that there are asymmetric slowly relaxing TLSs in the contact in addition to the fast TLSs. The total number of TLSs in the contact can be estimated as $N \sim cd^3$, where c $\sim 10^{-2} - 10^{-4}\,\text{nm}^{-3}$ is the typical concentration of TLSs in amorphous materials (see p. 835 of Ref. 6). For contacts with a diameter $d \sim 50 - 100$ nm the number of TLSs is N $\sim 10^2 - 10^4$. Therefore, one expects that the nonlinear con-

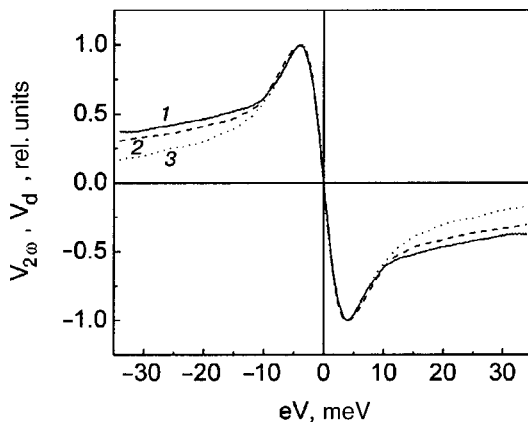ductance of a point contact at low energies will be determined by the scattering of electrons on structural defects of various natures, with a whole set of characteristic relaxation times.

By analogy with the high-frequency response of dirty contacts (the thermal regime of point-contact spectroscopy) to optical radiation[14] one expects that an additional quasibolometric contribution to the videodetection signal will be present (the difference of two I–V characteristics measured in the presence and absence of rf irradiation) under the condition $\omega\tau > 1$:

$$V_d(I_0) = \overline{V(I)} - V_0(I_0) = \frac{1}{4\sqrt{2}} \frac{d^2V}{dI^2}(I_0) i_\omega^2 + I_0 \frac{\partial R}{\partial P_{\text{rf}}} P_{\text{rf}},$$

$$(5)$$

where $\partial R / \partial P_{\text{rf}}$ is the rate of change of the steady-state quasiequilibrium occupation of the excited states of the TLSs under the influence of irradiation. Thus the videodetection signal has two components of different natures. One of them is due to rectification of the high-frequency alternating current at nonlinearities of the I–V characteristic, and its amplitude is proportional to the second derivative of the I–V characteristic. The second component is due to the steady-state occupation of the upper levels of the TLSs under the rf irradiation. This nonequilibrium occupation of the states of the TLSs causes a steady-state change in the contact resistance. The amplitude of the quasibolometric contribution to the signal [the second term in Eq. (5)] increases linearly with increasing transport current through the contact. In the dynamic measurements of $V_{2\omega 2}(eV)$ this steady-state contribution in the high-energy region decreases substantially, as is confirmed by the experimental curves in Fig. 5. It should be noted that the low- and high-frequency curves in Fig. 5 have been matched up in an arbitrary way, and, moreover, the origin and intensity of the background in the videodetection signal are not fully explained. It will therefore be necessary to conduct further experimental studies for different materials in different frequency ranges. It is also of fundamental importance to do a theoretical analysis of the dynamics of electron scattering on TLSs in point contacts, much as the analysis done for the electron–phonon interaction in Refs. 18 and 19, for example.

For some of the $Ni_{44}Nb_{56}$ contacts a slight minimum of the resistance was observed at biases near zero, both in the low-frequency and high-frequency measurements (Fig. 6). The scale of the high-frequency curves $V_d(eV)$ and $V_{2\omega 2}(eV)$ for 9.5 GHz in Fig. 6 has been modified so as to match with the low-frequency curve *1* for 3.7 kHz in the high-energy region $eV > 20$ meV. The second-harmonic voltage at the audiofrequency was recorded in the absence of the rf pump. The high-frequency curves *2* and *3* basically repeat the low-frequency dependence (*1*) except for some smearing of the singularities due to the rf irradiation. The complete similarity of the low- and high-frequency curves lets us rule out possible thermal effects in the point contacts under the influence of the transport current and rf irradiation. The energy dependence of the differential resistance of this contact, calculated by numerical integration of the data in Fig. 6, is shown in Fig. 7. A minimum of the resistance at $eV \rightarrow 0$ is observed against the background of the broad maximum on

FIG. 5. Energy dependence of the second-harmonic amplitudes (curves *1* and *3*) and of the videodetection signal (*2*), measured at audio (*1*) and microwave (*2,3*) frequencies for a $Ni_{44}Nb_{56}$ point contact. The experiment was done for $V_{\omega 1} = 0.6$ mV, $P_0 = 10^{-4}$ W, and $R = 11\,\Omega$.
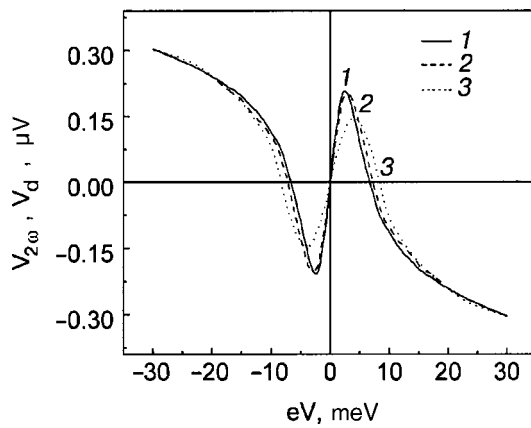
FIG. 6. Amplitudes of the second harmonic (*1,3*) and of the videoresponse signal (*2*) for a $Ni_{44}Nb_{56}$ contact containing residual superconductivity for measurements at frequencies of 3726 Hz (*1*), 4.75 GHz (*2*), and 9.5 GHz (*3*).

all three of the curves. The nature of this minimum may be related to residual superconductivity in a certain volume of the contact at the temperature of the measurements $T/T_c = 2.3$ (the transition temperature of $Ni_{44}Nb_{56}$ to the superconducting state is 1.8 K[4]). It is well known[20] that superconducting fluctuations of the order parameter are readily observed in metallic glasses up to temperatures of several times T_c. This is because of the small coherence length ξ and, hence, the smallness of the characteristic volume of the free-energy fluctuations in these materials, and their high resistivity in the normal state. In addition, the superconducting fluctuations should be manifested more strongly in a point-contact geometry than in a bulk sample. The superconductivity of a small part ($\sim \xi^3$) of the volume of the contact is responsible for the minimum appearing on the $R(eV)$ curve at $eV \rightarrow 0$, as shown in Fig. 7. The value of the ratio $(\xi/d)^3$ for this contact amounts to $\sim 10^{-2}$, which is comparable to the decrease of its resistance seen in Fig. 7.[2)]

The temperature of the transition of $Ni_{59}Nb_{41}$ to the superconducting state is very low, $T_c = 0.3$ K, 4 and we therefore did not observe any decrease of the contact resistance in the region $eV \rightarrow 0$ for that material at a temperature of 4.2 K.
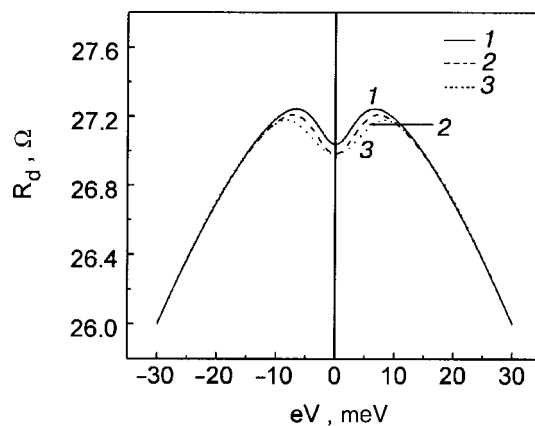

FIG. 7. Differential resistance of a $Ni_{44}Nb_{56}$ point contact, calculated according to the data of Fig. 5, for different methods of measurement. The numbering of the curves is the same as in Fig. 5.

CONCLUSION

In this study we have investigated the nonlinear frequency-dependent features of the conductance of point contacts of metallic glasses. We have measured the energy dependence of the amplitudes of the second harmonic at frequencies of 3726 Hz and 9.5 GHz with low-frequency and microwave modulation for the metallic glasses $Ni_{59}Nb_{41}$ and $Ni_{44}Nb_{56}$. The results of these experiments give direct evidence of the presence of fast relaxation processes in the contacts, the conductance of which is determined by electron scattering on the two-level systems typical of amorphous metals. We have shown that the spectral feature in the conductance of Ni_xNb_{1-x} point contacts at low energies remains practically unchanged when the second-harmonic signal is measured at a frequency of 9.5 GHz. This attests to fast electron–TLS scattering, with a characteristic time $\tau \ll 10^{-10}$ s.

However, the mechanism giving rise to this feature in the point-contact spectrum remains an open question. Further clarification is needed to determine whether the parameters of this feature, like the dynamics of the interaction of the conduction electrons with the TLSs, are described by a model of two-channel nonmagnetic Kondo scattering or by some other alternative mechanisms (see, e.g., Refs. 21 and 22). In principle, it is possible to have interference of different scattering mechanisms. In addition, the contribution from the interaction of the TLSs with phonons, usually neglected in theoretical treatments, may prove to be important, especially at large biases across the contact. The elucidation of all of these aspects of the relaxation dynamics of TLSs and a determination of the nature of the residual background in the videodetection experiments will require further experiments with metallic glasses of different compositions and a detailed theoretical analysis of the conductance of point contacts of amorphous metals.

[1)]The high-frequency curves were multiplied by scale coefficients of 0.55 and 0.24 in order to fit them to the low-frequency curves at the extremal points at biases of $+2.5$ and $+3.5$ meV for curves *3* and *4*, respectively.
[2)]The coherence length $\xi = 20$ nm was estimated from the value of the critical field $H_{c1} = 2$ T,[4] and the contact diameter $d = 96$ nm was calculated from its resistance.[13]

[1] J. L. Black, in *Glassy Metals I*, edited by H. J. Guntherodt and H. Beck, Springer-Verlag, New York (1981), p. 167.
[2] R. Harris and J. O. Strom-Olsen, in *Glassy Metals II*, edited by H. J. Guntherodt and H. Beck, Springer-Verlag, New York (1981), p. 325.
[3] R. J. P. Keijsers, O. I. Shklyarevskii, and H. van Kempen, Phys. Rev. Lett. **77**, 3411 (1996).
[4] A. Halbritter, A. Yu. Kolesnihenko, G. Mihály, O. I. Shklyarevskii, and H. van Kempen, Phys. Rev. B **61**, 5846 (2000).
[5] A. Zawadowski, Phys. Rev. Lett. **45**, 211 (1980).
[6] D. L. Cox and A. Zawadowski, Adv. Phys. **47**, 599 (1998).
[7] V. I. Kozub, Fiz. Tverd. Tela (Leningrad) **26**, 1955 (1984) [Sov. Phys. Solid State **26**, 1186 (1984)].
[8] V. I. Kozub and I. O. Kulik, Zh. Éksp. Teor. Fiz. **91**, 2243 (1986) [Sov. Phys. JETP **64**, 1332 (1986)].
[9] O. P. Balkashin, R. J. P. Keijsers, H. van Kempen, Yu. A. Kolesnichenko, and O. I. Shklyarevskii, Phys. Rev. B **58**, 1294 (1998).
[10] O. P. Balkashin, I. K. Yanson, A. Halbritter, and G. Mihály, Solid State Commun. **118**, 623 (2001).
[11] J. R. Tucker, IEEE J. Quantum Electron. **QE−15**, 1234 (1979).

[12] A. N. Omel'yanchuk and I. G. Tuluzov, Fiz. Nizk. Temp. **9**, 284 (1983) [Sov. J. Low Temp. Phys. **9**, 142 (1983)].

[13] I. K. Yanson and A. V. Khotkevich, *Atlas of Point-Contact Spectra and Electron–Phonon Interaction in Metals* [in Russian], Naukova Dumka, Kiev (1986).

[14] O. P. Balkashin and I. I. Kulik, Fiz. Nizk. Temp. **18**, 1357 (1992) [Low Temp. Phys. **18**, 946 (1992)].

[15] O. Laborde, A. Ravex, J. C. Lasajunias, and O. Bethoux, J. Low Temp. Phys. **56**, 461 (1984).

[16] O. P. Balkashin, I. K. Yanson, V. S. Solov'ev, and A. Yu. Krasnogorov, Zh. Tekh. Fiz. **52**, 811 (1982) [Sov. Phys. Tech. Phys. **27**, 572 (1982)].

[17] R. W. van der Heijden, PhD Thesis, Nijmegen (1982).

[18] I. O. Kulik, Fiz. Nizk. Temp. **11**, 516 (1985) [Sov. J. Low Temp. Phys. **11**, 516 (1985)].

[19] O. P. Balkashin, I. K. Yanson, and Yu. A. Pilipenko, Fiz. Nizk. Temp. **13**, 222 (1987) [Sov. J. Low Temp. Phys. **13**, 222 (1987)].

[20] W. L. Johnson, in *Glassy Metals II*, edited by H. J. Guntherodt and H. Beck, Springer-Verlag, New York (1981), p. 191.

[21] V. I. Kozub and A. M. Rudin, Phys. Rev. B **55**, 259 (1997).

[22] I. L. Aleiner, B. L. Altshuler, Y. M. Galperin, and T. A. Shutenko, Phys. Rev. Lett. **86**, 2629 (2001).

Translated by Steve Torstveit

QUANTUM EFFECTS IN SEMICONDUCTORS AND DIELECTRICS

Manifestation of toroidal excitations in the polariton spectrum of an insulator at its boundary with a metal in an electric field

I. E. Chupis*

B. Verkin Institute for Low Temperature Physics and Engineering National Academy of Sciences of Ukraine, pr. Lenina 47, 61103 Kharkov, Ukraine

A study is made of the influence of toroidal excitations on the spectrum of surface polaritons of an insulator at its boundary with an ideal metal in a static electric field perpendicular to the contact surface. It is shown that the toroidal polariton mode can be radiative and have normal or anomalous dispersion. A distinguishing feature of the toroidal polariton mode in comparison with an electric-dipole mode is that it crosses the light line, i.e., it can be resonantly excited by an electromagnetic wave propagating along the contact surface. This feature means that it is possible to identify a toroidal polariton mode in the spectrum by varying the angle of incidence of the electromagnetic wave. © *2001 American Institute of Physics.*
[DOI: 10.1063/1.1430847]

INTRODUCTION

It is known that surface polaritons do not exist in an insulator at a boundary with an ideal metal because of the so-called metallic quenching effect (see, e.g., Ref. 1). However, this forbiddenness is lifted in the presence of a static electric or magnetic field with a certain direction.[2,3] In the presence of static fields the bulk polariton excitations become surface ones, i.e., an expulsion of the field of the electromagnetic wave from the volume of the crystal to its surface occurs. This phenomenon is a result of the magnetoelectric (ME) effect, which consists in the appearance of an electric (magnetic) moment proportional to the alternating magnetic (electric) field of an electromagnetic wave and to the value of the applied static field. This effect is characterized by an off-diagonal component of the ME susceptibility, which is known[4] to signify the presence of a toroidal moment in the crystal. Apparently, the solenoidal toroidal states that arise are the cause of the expulsion of the field of an electromagnetic wave from the volume of an insulator to its surface. Therefore, it is of interest to take into account the characteristic toroidal excitations in the spectrum of surface polaritons of an insulator interfacing with a metal.

Toroidal moments are a third (together with the electric and magnetic) family of electromagnetic multipoles.[5] The toroidal moment vector **T** is the vector dual to the antisymmetric component of the ME tensor.[4] A toroidal moment may be due to the orbital motion of an electron in a metal or to excitonic excitations in a semiconductor.[6] In an insulator the existence of a toroidal moment may be due to the presence of a multisublattice spin structure. In that case the toroidal moment of the unit cell is given by the expression[7]

$$\mathbf{T} = \frac{\mu_0}{2} \sum_{\alpha} [\mathbf{r}_{\alpha} \times \mathbf{S}_{\alpha}], \tag{1}$$

where μ_0 is the Bohr magneton, $\mathbf{S}_{\alpha}$ and $\mathbf{r}_{\alpha}$ are the spin

moment and the radius vector of ion α in the unit cell of the crystal, measured from the center of the cell, and the summation is over all ions of the unit cell. The simplest example of a system with a spontaneous toroidal moment is a two-sublattice antiferromagnet, for which spontaneous electric polarization and magnetization are absent.

Excitations of the toroidal moment and toroidal polaritons in the absence of spontaneous electric, magnetic, and toroidal ordering in the crystal were studied in Refs. 8 and 9. It was noted that toroidal excitations are manifested in the infrared spectrum as unusual temperature dependence of the dielectric loss in TlGaSe$_2$ (Ref. 8).

In the present study we investigate the influence of characteristic toroidal excitations on the surface polariton spectrum of an insulator at its boundary with an ideal metal in the presence of a static electric field. It is assumed that the insulator has no electric, magnetic, or toroidal spontaneous ordering.

LAGRANGIAN AND SUSCEPTIBILITIES

It was shown in Ref. 8 that toroidal excitations are active in the IR region of the spectrum, where the electric-dipole excitations are also found. Therefore, the Lagrangian of the crystal should include not only terms containing the toroidal moment density **T** and its time derivative $\dot{\mathbf{T}}$ but also terms containing the electric polarization **P** and $\dot{\mathbf{P}}$.[9] The Lagrangian of a unit volume of a cubic crystal in a static electric field $\mathbf{E}_0$ and in alternating electric **e** and magnetic **h** fields is written in the form

$$L = \frac{\mu}{2}\dot{T} - \frac{a}{2}T^2 + \frac{f}{2}\dot{P}^2 - \frac{\kappa}{2}P^2 + (\mathbf{E}_0 + \mathbf{e})\cdot\mathbf{P} + \lambda_e\dot{\mathbf{T}}\cdot\mathbf{e}$$
$$+ \xi\mathbf{P}\cdot[\dot{\mathbf{P}}\times\mathbf{h}] + \lambda\,\mathbf{T}\cdot[\mathbf{E}\times\mathbf{h}] + \gamma\mathbf{T}\cdot[\mathbf{P}\times\mathbf{h}] + \gamma_0\dot{\mathbf{T}}\cdot\mathbf{P}. \tag{2}$$

The Lagrangian (2) contains the toroidal (the term with coefficient μ) and electric-dipole (the term with coefficient f) kinetic energies, the potential energies of the subsystems, and their interaction energies (the last two terms). We have not included spatial dispersion in the Lagrangian, as we are assuming the excitations of the moments are long-wavelength ($a_c k \ll 1$, where a_c is the lattice constant and k is the wave vector), nor dissipation, the features of which in the presence of a toroidal moment were studied in Ref. 8.

The relation between the phenomenological coefficients μ, a, λ, and λ_e with the microscopic parameters for the model of an excitonic insulator was considered in Ref. 9. Let us estimate the order of several of the parameters in (2) for an insulator in which the toroidal moment is due to a non-uniform distribution of spins in the unit cell (1).

The spin–orbit interaction energy of the magnetic moment of an ion with the effective magnetic field created by the motion of an ion with velocity $\mathbf{v}$ in the crystalline field $\mathbf{E}$ is written in the form

$$E_{sl} = \frac{1}{c}\mathbf{M}\cdot[\mathbf{E}\times\mathbf{v}], \tag{3}$$

where c is the speed of light. The displacement $\mathbf{r}$ of an ion with positive charge q in the field $\mathbf{E}$ corresponds to an electric polarization $\mathbf{P} = q\mathbf{r}V_c^{-1} = \chi\mathbf{E}$, where χ is the dielectric susceptibility and V_c is the volume of the unit cell. Hence $E_{sl} \approx -q(c\chi V_c)^{-1}\mathbf{v}\cdot[\mathbf{r}\times\mathbf{M}]$. The displacement of the ion gives rise to a fluctuational toroidal moment with a density $\mathbf{T}\sim[\mathbf{r}\times\mathbf{M}]$. Hence $E_{sl}\sim -q(c\chi V_c)^{-1}\mathbf{v}\cdot\mathbf{T}\sim -c^{-1}\mathbf{T}\cdot\dot{\mathbf{E}}$. Consequently, the constant λ_e in the Lagrangian, which, as we know, is defined to within a total time derivative, can be assumed to be a quantity of order c^{-1}, i.e., $\lambda_e\sim c^{-1}$.

In magnetoelectrics, i.e., in magnets with a linear ME effect, the term with the coefficient λ corresponds to the ME energy density $W_{me} = -\alpha_{ik}E_iH_k$, where α_{ik} is the ME susceptibility tensor. The spontaneous toroidal moment $\mathbf{T}^0$ exists in magnetoelectrics with nonzero antisymmetric components of the tensor α_{ik} and is the vector dual to its antisymmetric part. Therefore $\lambda T_i^0 = \varepsilon_{ikl}\alpha_{kl}$. Assuming that $T^0\sim M_0 a_c$, where M_0 is the magnetic moment density, we obtain the following estimate for the coefficient λ: $\lambda\sim\alpha(M_0 a_c)^{-1}$, where α is the value of the off-diagonal component of the ME susceptibility, and $\lambda > 0$.[9]

The value of the coefficient a in the Lagrangian (2) can be estimated for the simple example of a magnet without a spontaneous toroidal moment. In such a magnet T can be induced by crossed electric and magnetic fields, and its value, as follows from the minimum of the energy with coefficients a and λ, is

$$T_i = \lambda a^{-1}[\mathbf{E}\times\mathbf{H}]_i. \tag{4}$$

Let us consider a unit cell with two equivalent magnetic ions which are located on the X axis and are connected by a center of inversion and have the same equilibrium spins along the magnetic easy axis Y. It is easy to see [see Eq. (1)] that such a cell does not have a spontaneous toroidal moment. Now suppose that an electric field is applied to the crystal along the X axis and a magnetic field along the Z axis, perpendicular to the direction of the equilibrium spins. The electric field displaces each ion by a distance Δx, and

the magnetic field causes the spins to deviate from the easy axis by an amount ΔS_z. The unit cell acquires a toroidal moment, directed along the Y axis and proportional to the product $\Delta x \Delta S_z$ (it is easy to check that there is no toroidal moment in the linear approximation). The induced toroidal moment density $T_y = -\Delta x M_z$. For a uniaxial crystal the projection of the magnetic moment on the magnetic field direction is $M_z = H_z/\beta$ (β is the anisotropy constant). The value of the displacement Δx of an ion in the electric field E_x is related to the electric polarization by $P_x = q\Delta x V_c^{-1} = \chi E_x$, and hence $\Delta x = \chi q^{-1}E_x V_c$ and, consequently, $T_y = -\chi V_c(q\beta)^{-1}E_x H_z$. Comparing this expression with Eq. (4), we find that $\lambda a^{-1} = \chi V_c(q\beta)^{-1}$. Hence, by using the estimate of λ given above and the fact that $M_0 = \mu_{\mathrm{eff}}V_c^{-1}$, we obtain

$$a\sim\frac{q\alpha\beta}{\mu_{\mathrm{eff}}a_c\chi}. \tag{5}$$

Now let us assume that the static electric field $\mathbf{E}_0$ is directed along the Z axis. The response of the system to the electric and magnetic fields is described by the dielectric, magnetic, and ME susceptibilities $\chi_{ik}^{em} = \partial P_i/\partial h_k$ and $\chi_{ik}^{me} = \partial m_i/\partial e_k$. In the absence of damping one has $\chi_{ik}^{em} = (\chi_{ki}^{me})^*$. The electric displacement $\mathbf{d}$ and magnetic induction $\mathbf{b}$ are defined by the standard expressions

$$d_i = \varepsilon_{ik}e_k + 4\pi\chi_{ik}^{em}h_k, \quad b_i = \mu_{ik}h_k + 4\pi\chi_{ik}^{me}e_k.$$

Solving Lagrange's equations for $\mathbf{T}$ and $\mathbf{P}$, which we assume are proportional to $\exp(i\omega t)$, and using the method of complex amplitudes, we can obtain expressions for the components of the susceptibilities. We will be needing only the expressions for the components ε_{zz} and χ_{xy}^{em}, which are written:

$$\varepsilon_{zz} = \frac{(\Omega_1^2 - \omega^2)(\Omega_2^2 - \omega^2)}{(\omega_1^2 - \omega^2)(\omega_2^2 - \omega^2)}; \quad \chi_{xy}^{em} = -\frac{i\alpha}{4\pi},$$

$$\alpha = \frac{4\pi g_0 E_{0z}\omega(\omega^2 - \tilde{\omega}^2)}{(\omega_1^2 - \omega^2)(\omega_2^2 - \omega^2)};$$

$$\Omega_{1,2}^2 = \frac{1}{2(1-\nu)}\Big[\Omega_0^2 + \omega_T^2 - \nu\omega_P^2 - 8\pi\lambda_e\gamma_0(\mu f)^{-1}$$
$$+ \gamma_0^2(\mu f)^{-1}\mp\{[\Omega_0^2 + \omega_T^2 - \nu\omega_p^2$$
$$- 8\pi\lambda_e\gamma_0(\mu f)^{-1} + \gamma_0^2(\mu f)^{-1}]^2$$
$$- 4(1-\nu)\Omega_0^2\omega_T^2\}^{1/2}\Big]; \tag{6}$$

$$\omega_{1,2}^2 = \frac{1}{2}\Big\{\omega_T^2 + \omega_p^2 + \frac{\gamma_0^2}{f\mu}$$
$$\mp\Big[(\omega_p^2 - \omega_T^2)^2 + \frac{2\gamma_0^2(\omega_p^2 + \omega_T^2)}{f\mu} + \frac{\gamma_0^4}{f^2\mu^2}\Big]^{1/2}\Big\};$$

$$\tilde{\omega}^2 = g^{-1}(\bar{\lambda}\lambda_e\mu^{-1}\bar{\omega}_p^2 + \xi f^{-1}\kappa^{-1}\omega_T^2);$$

$$\bar{\omega}_p^2 = \omega_p^2(1 + \gamma_0\kappa^{-1}\lambda_e^{-1}), \quad \bar{\lambda} = \lambda + \gamma\kappa^{-1};$$

$$g = \bar{\lambda}\lambda_e\mu^{-1} + \xi(f\kappa)^{-1}; \quad \Omega_0^2 = \omega_p^2 + 4\pi f^{-1};$$

$$\omega_p^2 = kf^{-1}; \quad \omega_T^2 = a\mu^{-1}, \quad \nu = 4\pi\lambda_e^2\mu^{-1}, g_0 = q/mc.$$

Here ω_p and ω_T are the frequencies of noninteracting electric-dipole and toroidal excitations, respectively, and ω_1 and ω_2 are the modes with the interaction taken into account. The constant $\xi = V_c/qc$ (Ref. 2) is positive, since q is the ion charge. The constants μ, a, κ, f, and λ are also positive. We shall also assume below that the constant quantity λ_e is positive.[9] The terms with coefficients γ_0 and γ, which describe the interaction of toroidal and electric-dipole excitations, differ from the terms with coefficients λ_e and λ, respectively, by having **P** in place of **e**, and it is natural to assume that the coefficients γ and γ_0 are also positive.

SPECTRUM OF SURFACE POLARITONS

Suppose that an insulator which is not in a magnetically ordered state ($\mu_{ik} = \delta_{ik}$) and occupies the half space $Z > 0$ is in contact with an ideal metal ($Z < 0$). A static electric field is directed along the normal to the contact surface, $E_0 = E_{0z}$. A surface electromagnetic wave, propagating along the X axis in the contact plane and interacting with electric-dipole and toroidal excitations of the insulator in the presence of a static electric field, has nonzero field components $e_z, h_y \propto \exp(i\omega t - ikx - k_0 z)$ (Ref. 2).[1)] The dispersion relation for surface polaritons and their penetration depth in the insulator, $\delta = k_0^{-1}$, are given by the expressions[2]

$$k^2 = \frac{\omega^2}{c^2}\varepsilon_{zz}(\omega), \quad \delta = -\frac{c}{\omega\alpha(\omega)}. \tag{7}$$

In the case under discussion, ε_{zz} and α are given by formulas (6). The surface polaritons in the insulator exist only because of the off-diagonal component of the ME susceptibility $\alpha \neq 0$. If $\alpha = 0$, then $\delta = \infty$, i.e., the polaritons are of the bulk type. As we see from Eq. (7), surface polaritons exist only for values

$$\varepsilon_{zz} \geq 0, \quad \alpha < 0 (\delta > 0). \tag{8}$$

Satisfaction of these conditions depends on the values of the constants of the Lagrangian.

Let us estimate the parameter $\nu = 4\pi\lambda_e^2\mu^{-1}$ (see Eq. (6)) in the case when the toroidal moment is given by expression (1). Since $\omega_T^2 \equiv a\mu^{-1}$, we have $\mu^{-1} = \omega_T^2/a$. Using (5) and the fact that $\lambda_e \sim c^{-1}$, we obtain $\nu \sim 4\pi a_c \chi \mu_{\rm eff} \omega_T^2 (qc^2\alpha\beta)^{-1}$. For the values $a_c = 10^{-7}$ cm, $\chi = 1$, $\beta = 1$, $\mu_{\rm eff} = 5\mu_0$, $q = 5 \times 10^{-10}$ cgs esu, $\alpha = 10^{-3}$, and $\omega_T = 10^{13}$ s^{-1}, we obtain $\nu \sim 10^{-8}$. Such a small value is due to the relativistic smallness of the spin–orbit interaction. However, in an excitonic insulator the toroidal energy is due to the Coulomb interactions,[6,9] and the parameter ν is not so small. Since the interaction parameter γ_0 is in any case not greater than λ_e, it follows from the expressions (6) for $\omega_{1,2}$ that the parameter ν is a measure of the interaction of the toroidal and electric-dipole modes.

Analysis of conditions (8) with allowance for the sign of E_0, i.e., the directions of the static electric field in the interior of the insulator ($E_0 > 0$) or along the outer normal ($E_0 < 0$) gives the form of the surface polariton spectra shown in Fig. 1. The solid curves correspond to the modes for a field direction along the outer normal to the insulator, and the dashed curves correspond to the modes for the opposite direction of the field.
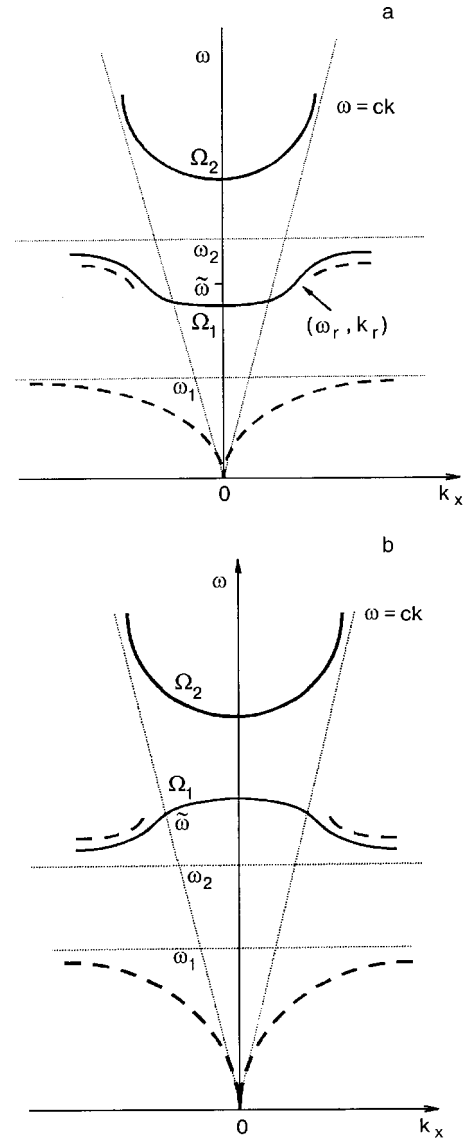
FIG. 1. Spectrum of surface polaritons of an insulator at its boundary with an ideal metal in the case when a static electric field is directed along the outer normal to the insulator (solid curves) and into the insulator (dashed lines): a—different possible relations between the frequencies ω_T and ω_p; b—$\omega_T > \omega_p$.

The spectrum shown by the solid intermediate curve in Fig. 1a exist in the cases

1) $\omega_p > \omega_T$, $\omega_2 < \tilde{\omega} < \bar{\omega}_p$,

2) $\omega_p < \omega_T < \bar{\omega}_p$, $\omega_2 < \tilde{\omega} < \bar{\omega}_p$, $R < A$,

$$R = \nu(\omega_p^2 - \omega_T^2) + \gamma_0(f\mu)^{-1}(8\pi\lambda_e - \gamma_0),$$

$$A = \gamma_0^2[f\mu(\omega_T^2 - \omega_p^2)]^{-1}. \tag{8a}$$

The intermediate mode in Fig. 1a consists of two parts: the solid curve in the frequency interval $[\Omega_1, \tilde{\omega}]$ and the dashed curve in the interval $[\tilde{\omega}, \omega_2]$, in the following cases:

1) $\omega_p > \omega_T$, $\max(\Omega_1, \omega_T) < \tilde{\omega} < \omega_2$;

2) $\omega_p < \omega_T < \bar{\omega}_p$, $\omega_T < \bar{\omega} < \omega_2$, $R < 0$;

3) $\omega_p < \omega_T < \bar{\omega}_p$, $\Omega_1 < \tilde{\omega} < \omega_2$, $0 < R < A$;

4) $\bar{\omega}_p < \omega_T < \Omega_2$, $\Omega_1 < j\tilde{\omega} < \omega_T$, $R < 0$. $\qquad$ (9)

The intermediate mode in Fig. 1a is entirely that corresponding to the dashed curve ($\tilde{\omega} < \Omega_1$) if

1) $\omega_p > \omega_T$, $\omega_T < \Omega_1$, $\omega_T < \tilde{\omega} < \Omega_1$;

2) $\omega_p < \omega_T < \bar{\omega}_p$, $\omega_T < \tilde{\omega} < \Omega_1$, $0 < R < A$;

3) $\bar{\omega}_p < \omega_T < \Omega_2$, $\bar{\omega}_p < \tilde{\omega} < \Omega_1$, $R < 0$;

4) $\bar{\omega}_p < \omega_T < \Omega_2$, $\bar{\omega}_p < \tilde{\omega} < \omega_T$, $0 < R < A$. $\qquad$ (10)

The spectrum in Fig. 1b (the solid intermediate curve) corresponds to the parameters

1) $\omega_p < \omega_T < \bar{\omega}_p$, $\omega_T < j\tilde{\omega} < \omega_p$, $R > A$;

2) $\bar{\omega}_p < \omega_T < \Omega_2$, $\bar{\omega}_p < \tilde{\omega} < \omega_T$, $R > A$. $\qquad$ (11)

The intermediate mode in Fig. 1b consists of a solid curve for frequencies in the interval $[\tilde{\omega}, \Omega_1]$ and the dashed curve in the frequency interval $[\omega_2, \tilde{\omega}]$, if $\omega_p < \omega_T < \bar{\omega}_p$, $\omega_2 < \tilde{\omega} < \Omega_1$, $R > A$.

If, however, $\omega_p < \omega_T < \bar{\omega}_p$, $\Omega_1 < \tilde{\omega} < \bar{\omega}_p$, $R > A$, then the intermediate mode in Fig. 1b is that shown by the dashed curve.

Analysis of the spectrum is done for values of the toroidal frequency $\omega_T < \Omega_2$, with $\Omega_2 \approx \Omega_0$. If $\omega_T < \omega_p$, then the lower branch ω_1 is the frequency of predominantly toroidal excitations, and ω_2 is predominantly electric-dipole. For $\omega_T > \omega_p$, on the contrary, ω_2 is the mode of toroidal excitations and ω_1 that of electric-dipole. In all cases the upper mode with frequencies greater than Ω_2 is electric-dipole, while the mode with frequencies near Ω_1 is toroidal. Figure 1b corresponds to values $\omega_T > \omega_p$, and Fig. 1a to various cases [see Eqs. (8)–(10)].

In all cases the toroidal excitations are manifested in the existence of an intermediate mode with normal (Fig. 1a) or anomalous (Fig. 1b) dispersion. This mode, like the upper mode, is radiative. However, if the upper (electric-dipole) mode can be resonantly excited only for oblique incidence of the electromagnetic wave (to satisfy conservation of quasi-momentum), then the toroidal mode interacts resonantly with the electromagnetic wave both for oblique and for tangential (parallel to the surface) incidence of the light. The toroidal mode crosses the light line at the point where $\varepsilon_{zz} = 1$, $k_r = \omega_r/c$. From Eq. (6) we find the resonance frequency ω_r:

$$\omega_r^2 = \frac{1}{2 f \lambda_e} [2\lambda_e \gamma_0 - \mu + \kappa \lambda_e^2$$

$$+ \sqrt{(\mu - 2\lambda_e \gamma_0 - \kappa \lambda_e^2)^2 + 4 f \mu \lambda_e^2 \omega_T^2}]. \qquad (12)$$

Since $\mu \gg \lambda_e^2$ (see the estimates above), we have $\omega_r \approx \omega_T$. Assuming that the $P - T$ interaction is weak and that the frequencies ω_T and ω_p are not close together, we find from (6) that we have approximately

$$\omega_1^2 \cong \omega_T^2 (1 + A), \quad \omega_2^2 \cong \omega_p^2 (1 - A), \quad \omega_p > \omega_T,$$

$$\Omega_1^2 \cong \omega_T^2 \left(1 + \frac{R}{\Omega_0^2 - \omega_T^2}\right), \quad A \ll 1. \qquad (13)$$

In the case $\omega_p < \omega_T$ the frequency ω_1 in Eq. (13) should be replaced by ω_2.

We see from Eq. (13) that for $\omega_p < \omega_T$ the frequencies Ω_1 and ω_2 are close. Therefore, in the case of anomalous

dispersion of the intermediate toroidal mode (Fig. 1b) its existence interval is small. The existence interval is also small for the intermediate mode in Fig. 1a for $\omega_p < \omega_T$.

If $\omega_T < \omega_p$, however, then the frequencies Ω_1, ω_2, and $\tilde{\omega}$ are not close, and the frequency interval in the which the intermediate mode exists is not small. In the case $E_0 < 0$ toroidal excitations occur in the frequency interval $[\Omega_1, \omega_2]$ for $\omega_2 < \tilde{\omega} < \bar{\omega}_p$ or in the interval $[\tilde{\omega}, \Omega_1]$ if $\Omega_1 < \tilde{\omega} < \omega_2$ ($\omega_T < \Omega_1$) or $\omega_T < \tilde{\omega} < \omega_2$ ($\omega_T > \Omega_1$). In both cases $\tilde{\omega} > \omega_r$, and resonance of toroidal excitations with an electromagnetic wave parallel to the surface is possible. For $\omega_T < \omega_p$ the lower mode ω_1 is also toroidal, but it is not radiative. Excitations of the electric polarization correspond to the upper mode ($\omega \geq \Omega_2$) and to excitations with intermediate mode frequencies near ω_2.

If, however, $\omega_p < \omega_T$, then the intermediate mode is toroidal and the upper and lower modes are electric-dipole.

CONCLUSION

A comparison of the dispersion relations in Fig. 1a and 1b with the spectrum obtained in Ref. 2 permits the following conclusions.

The presence of toroidal excitations preserves the effect in which the polariton branches switch over when the electric field direction is reversed (the solid and dashed curves in the figures).

The toroidal excitations give rise to additional modes in the surface polariton spectrum; these modes have normal or anomalous dispersion, but the latter occurs only for the toroidal mode. Toroidal modes can be radiative, i.e., they can interact resonantly with an electromagnetic wave.

In practice, however, identification of the observed spectral lines is a complicated matter. The results obtained here make it possible to determine the toroidal mode (the intermediate curve in the figures) thanks to its crossing with the light line in an experiment on resonant excitation of surface polaritons. As was shown in Refs. 2 and 3, in the insulator–ideal metal system under consideration here the radiative modes of surface polaritons of the insulator (the upper and intermediate branches of the spectrum) can be studied by their direct resonant interaction with a light wave without recourse to the methods ordinarily used: frustrated total internal reflection, Raman scattering, etc. This possibility is a consequence of the fact that the surface polariton mode in the system considered is found to the left of the light line and, consequently, the wave vector k_x of a polariton with frequency ω is smaller than the wave vector $k = \omega/c$ of a light wave propagating parallel to the surface along the X axis. In the case of oblique incidence of an electromagnetic wave at an angle θ to the normal, so that the quasimomentum along the X axis can be conserved, i.e., for $k_x = (\omega/c)\sin\theta < \omega/c$, the electromagnetic wave can resonantly excite a surface polariton.

The circumstance that the toroidal mode, unlike the electric-dipole modes, crosses the light line means that it can be resonantly excited not only for oblique but also for tangential incidence of the light wave. In an experiment on resonant excitation of surface polaritons the electric-dipole spectral lines should be "quenched" and vanish as the angle of incidence is increased from 0 to 90°. However, the spectral

lines of the toroidal polaritons should remain even for tangential incidence of the light. This circumstance presents an opportunity for discriminating the toroidal polariton from the others.

---

*E-mail: chupis@ilt.kharkov.ua

[1]In our case the z component of the magnetic induction is zero, and therefore the results obtained below are also valid for the contact of an insulator with a superconductor.

---

[1] V. M. Agranovich and D. L. Mills (Eds.), *Surface Polaritons* [North-Holland, Amsterdam (1982); Nauka, Moscow (1985)].

[2] I. E. Chupis and D. A. Mamaluǐ, JETP Lett. **68**, 922 (1998).

[3] I. E. Chupis and D. A. Mamaluy, J. Phys.: Condens. Matter **12**, 1413 (2000).

[4] B. A. Volkov, A. A. Gorbatsevich, and Yu. V. Kopaev, Zh. Éksp. Teor. Fiz. **86**, 1870 (1984) [Sov. Phys. JETP **59**, 1087 (1984)].

[5] V. M. Dubovik and L. A. Tosunyan, Fiz. Élem. Chastits At. Yadra **14**, 1193 (1983) [Sov. J. Part. Nucl. **14**, 504 (1983)].

[6] B. A. Volkov, A. A. Gorbatsevich, Yu. V. Kopaev, and V. V. Tugushev, Zh. Éksp. Teor. Fiz. **81**, 1905 (1981) [Sov. Phys. JETP **54**, 1008 (1981)].

[7] A. A. Gorbatsevich and Yu. V. Kopaev, Ferroelectrics **161**, 321 (1994).

[8] D. G. Sannikov, JETP Lett. **41**, 277 (1985).

[9] Yu. V. Kopaev and V. V. Tugushev, Zh. Éksp. Teor. Fiz. **88**, 2244 (1985) [JETP **61**, 1327 (1985)]; JETP Lett. **41**, 392 (1985).

Translated by Steve Torstveit

LATTICE DYNAMICS

Low-temperature thermal expansion of fullerite C$_{60}$ alloyed with argon and neon

A. N. Aleksandrovskii,* V. G. Gavrilko, V. B. Esel'son, V. G. Manzhelii, B. G. Udovidchenko, and V. P. Maletskiy

B. Verkin Institute for Low Temperature Physics and Engineering of the National Academy of Sciences of Ukraine, 47 Lenin Ave., Kharkov, 61103, Ukraine

B. Sundqvist

Umea University, Department of Experimental Physics, 90187 Umea, Sweden

The linear thermal expansion of compacted fullerite C$_{60}$ alloyed with argon (Ar$_x$C$_{60}$) and neon (Ne$_x$C$_{60}$) are investigated by a dilatometric method. The experimental temperature is 2–12 K. In the same temperature interval the thermal expansion of Ar$_x$C$_{60}$ and Ne$_x$C$_{60}$ are examined after partial desaturation of the gases from fullerite. It is found that Ar and Ne alloying affects the temperature dependence of the thermal expansion coefficient of C$_{60}$ quite appreciably. The libration and translation contributions to the thermal expansion of pure C$_{60}$ are separated. The experimental results on the thermal expansion are used to obtain the Debye temperature of pure C$_{60}$. The effects observed are tentatively interpreted. © *2001 American Institute of Physics.* [DOI: 10.1063/1.1430848]

Previously[1,2] we detected a negative coefficient of linear thermal expansion of polycrystalline and single-crystal C$_{60}$ at helium temperatures. The effect was tentatively attributed to tunneling rotation of the C$_{60}$ molecules. In the orientational glass, which evolves in fullerite below 90 K, the potential barriers U_φ impeding rotation of the molecules can vary within wide limits. The tunneling rotation can be performed only by those molecules for which the U_φ barriers are quite low. Such molecules are referred to below as defects. If the U_φ barriers grow upon a decrease in the crystal volume, the tunneling rotation leads to negative thermal expansion of the crystal.[3,4] The tunneling rotation is also characterized by high absolute values of the Grüneisen coefficient.[3] These are the features that we detected experimentally.[1,2]

The factors that might cause the negative thermal expansion of fullerite C$_{60}$ were analyzed in Refs. 5 and 6. Since the C$_{60}$ molecules have fivefold symmetry axes, the molecules cannot be orientationally ordered completely; hence, certain defects are inevitable at low temperatures. The negative thermal expansion has been explained qualitatively[6] by assuming the coexistence of different orientational domains in the simple cubic lattice of C$_{60}$. The potential relief is much smoother in the interdomain space (domain walls) than inside the domains, and the U_φ barriers impeding rotation of the molecules are much lower in the domain walls. As a result, the molecules in the domain walls (unlike those inside the domains) can remain nearly free rotators down to much lower temperatures.

The aim of this study was to test the assumptions used in Refs. 1 and 2. We investigated the thermal expansion coefficient α of compacted C$_{60}$ alloyed with inert gases at 2–12 K. The alloying gas atoms introduced into the fullerite lattice

were expected to change the U_φ barriers impeding rotation of the neighboring C$_{60}$ molecules. They could thus influence the probability of rotational tunneling of these molecules and the tunneling-induced contribution to the thermal expansion. If the U_φ barrier height and (or) width increase, the total negative thermal expansion $\int \alpha \, dT$ should decrease and shift towards lower temperatures. Let us remember that in the low-temperature phase each C$_{60}$ molecule is associated with two tetrahedral and one octahedral interstitial cavities whose average linear dimensions are about 2.2 Å and 4.2 Å, respectively.[7–9] According to x-ray and neutron diffraction data,[10–13] the Ne and Ar atoms, with gas-kinetic diameters of 2.788 Å and 3.405 Å,[14] respectively, occupy only the octahedral cavities. The studies were carried out using a high-sensitivity capacitance dilatometer.[15] The experimental procedure was described in Ref. 1. The sample was prepared by compacting high-purity (99.99%) C$_{60}$ powder under about 1 kbar at room temperature. The method of preparation of a sample precluded appreciable contents of argon and atmospheric gases in fullerite.[1] The grain sizes were 0.1–0.3 mm. The resulting sample was a cylinder 9 mm high and 10 mm in diameter. The preliminary results were published in Ref. 16.

Ar–ALLOYED FULLERITE

The linear expansion coefficient of the C$_{60}$ sample was first measured before alloying at 2–12 K. The sample was then alloyed with argon at room temperature under atmospheric pressure. The alloying lasted for 460 hours. The alloyed sample was slowly cooled in the alloying gas atmosphere to helium temperatures. Since in the process of cooling and measurement the walls of the measuring cell of
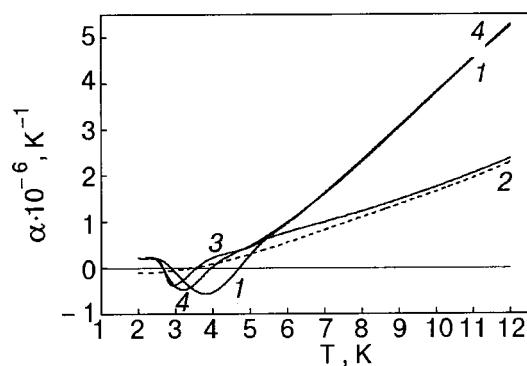
FIG. 1. Temperature dependences of the thermal expansion of compacted fullerite C_{60}: pure fullerite before alloying with Ar (*1*); Ar-alloyed fullerite (*2*); fullerite after evacuation of Ar for 3 days (*3*) and for 45 days (*4*).

FIG. 2. Temperature dependences of the thermal expansion of pure fullerite C_{60}: polycrystalline samples[1] (*1*); single crystal[2] (*2*); polycrystalline samples (*3*) (in this study).

the dilatometer are colder than the sample, the alloying gas becomes condensed on the cell walls (not on the sample) as the temperature falls. Then the thermal expansion coefficient of the Ar-alloyed C_{60} was measured at 2–12. Note that on cooling, the phase transitions of C_{60} occurred in an Ar atmosphere.

Figure 1 shows the measured coefficients before (curve *1*) and after (curve *2*) Ar-alloying. It is seen that the alloying has strongly affected the thermal expansion of C_{60}: the introduction of the alloying gas reduced considerably the positive coefficients and strongly suppressed the negative thermal expansion effect and shifted it towards lower temperatures. To explain the effects observed, it seems natural to assume that the atoms of Ar impurity impede rotation of the C_{60} molecules and thus enhance the noncentral forces acting upon the C_{60} molecules. With the noncentral forces enhanced, the librational frequencies ω_i of the C_{60} molecules should increase, and at $T < h\omega_i/k$ the contribution of librations to the heat capacity and thermal expansion of the crystal should decrease. At 5–12 K the tunneling effects are no longer important. In this temperature range the translational lattice vibrations and the molecular librations are responsible for the thermal expansion. In Refs. 17 and 18 the librational contribution to the heat capacity of C_{60} was described using two librational frequencies, 30 K and 58 K. Thus the above inequality holds for the temperature interval 5–12 K, and the assumed decrease in the librational contribution to the thermal expansion at these temperatures seems to be reasonable. As the noncentral forces increase, the U_{φ} barriers impeding rotation of the molecules also become higher. This diminishes the probability of rotational C_{60} tunneling and the tunneling splitting of the energy levels. As a result, the negative thermal expansion decreases and the region of tunneling effects shifts towards lower temperatures.

We should remember that the librational contribution is made by all C_{60} molecules, while the negative contribution is made only by the molecules which we call "defects."

When the measurement of the thermal expansion coefficient of the alloyed C_{60} sample at low temperatures was completed, the sealed measuring cell with the sample was warmed to room temperature and evacuated to 1 $\times 10^{-3}$ mm Hg. The gas was evacuated at room temperature for 3 days. The thermal expansion of the sample was then investigated again at low temperatures. The results obtained
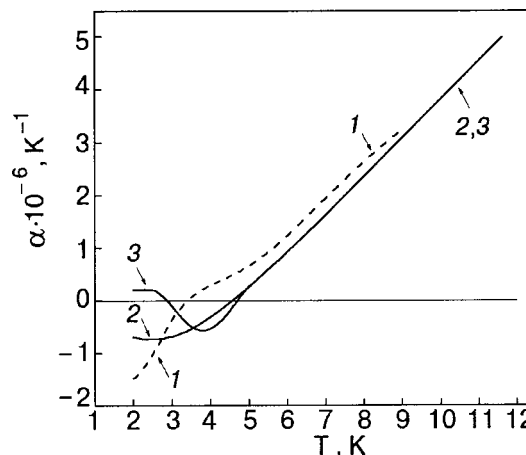
are shown in Fig. 1 (curve *3*). It is seen that the thermal expansion coefficient changes only slightly above 5 K. Below 3.5 K the change is more appreciable: there appears a region of negative thermal expansion with a nonmonotonic temperature dependence $\alpha(T)$. Qualitatively, the dependence is similar to that for the sample before alloying, but the minimum in curve *3* is smaller and shifted towards lower temperatures. Since the temperature dependence of the thermal expansion coefficient of pure C_{60} was not restored after the 3-day gas evacuation, the measuring cell with the sample was warmed again to room temperature and evacuated for 45 days. We then repeated the measurement of the thermal expansion coefficient at low temperatures. The results obtained are shown in Fig. 1 (curve *4*). In contrast to the short-evacuation results, the prolonged evacuation changes the "high-temperature," part ($T > 5$ K) of the dependence $\alpha(T)$ more significantly. After a 48-day evacuation, the coefficients α of the pure and alloyed C_{60} samples practically coincide at $T > 5$ K, whereas their dependences $\alpha(T)$ at $T < 5$ K still differ considerably.

The changes in $\alpha(T)$ after removal of argon from the sample may be explained as follows. The molecules that we call "defects" are inevitably displaced with respect to the lattice sites. As a result, the octahedral voids surrounding such molecules are not identical, and the potential wells that they form for the impurity are different—deeper or shallower than the octahedral potential wells adjacent to most of the C_{60} molecules. At the initial stage of evacuation, the Ar atoms first leave the shallow potential wells near the defects, which causes faster changes in the negative part of $\alpha(T)$. The removal of the Ar atoms from the deeper wells is slower than from most of the crystal volume. That is why at the completing stage, the positive part of $\alpha(T)$ is restored faster at $T > 5$ K.

Note another interesting fact. Figure 2 shows the linear thermal expansion coefficients for a single crystal[2] (curve *2*) and two polycrystalline samples investigated in this study (curve *3*) and in Ref. 1 (curve *1*). At $T > 5$ K the α values of all the samples are close to each other. However, considerable distinctions are observed in the temperature region where the thermal expansion becomes negative. We attribute
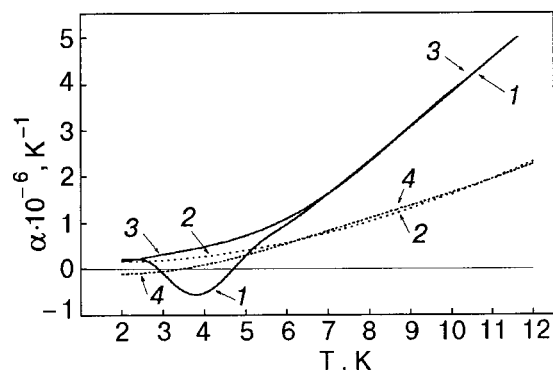
FIG. 3. Linear thermal expansion coefficients of fullerite C_{60} alloying with Ne: pure compacted fullerite before alloying (*1*); compacted fullerite alloyed with Ne (*2*); compacted fullerite after evacuation of Ne (1 day) (*3*); compacted fullerite alloyed with Ar (*4*).

this to different amounts of the ''residual'' impurity whose particles are still present in the deep potential wells near the defects. The negative thermal expansion should therefore be particularly sensitive to the pre-history of the sample.

Ne-ALLOYED FULLERITE

To speed up the saturation (desaturation) of C_{60}, we needed a gas with smaller particles. Our choice was neon. It is known from the literature[10,19] that saturation of C_{60} with Ne proceeds much faster than in the case of Ar: at room temperature it takes no more than 24 hours. To estimate the saturation time of our sample from these data, we need to know the grain sizes in Refs. 10 and 19. In Ref. 20 (the same laboratory as in Ref. 19), the average grain size was $l \sim 0.08$ mm. Since the characteristic time of saturation is $\tau \sim l^2$, it should be $\tau \sim 10^2$ hours in our case. The choice of Ne as an alloying gas is also based on the fact that Ne (and Ar) atoms become localized in the octahedral interstices. At room temperature and atmospheric pressure they occupy 21% of these interstices.[10] Taking into account that in a simple cubic lattice each of C_{60} molecules is surrounded by six octahedral interstices, the 21% occupancy implies that with randomly distributed impurity atoms, about 75% of the C_{60} molecules have Ne atoms nearby.

C_{60} was alloyed with Ne at room temperature under atmospheric pressure for 340 hours by the same procedure as was applied for Ar-alloying. The sample was then cooled in a Ne atmosphere to the temperature of the experiment, and the linear thermal expansion coefficients were measured.

The results obtained are shown in Fig. 3 (dashed curve *2*). For comparison, the same figure shows the thermal expansion coefficient of Ar-alloyed C_{60} (curve *4*). It is seen that above 6 K the curves practically coincide; below 6 K neon influences the thermal expansion coefficient more strongly than Ar does. The behavior of the low-temperature part of curve *2* (see Fig. 3) can be accounted for by a larger amount of Ne in the sample, since Ne dissolves much faster than Ar.

We then removed some quantity of Ne from the sample (24 hours at room temperature) and measured the thermal expansion coefficient again (Fig. 2, curve *3*). It is seen that above 7 K the coefficient came back to its prior-to-alloying values. Below 7 K the distinctions between the coefficients measured before and after alloying even increased.

At the concluding stage of the experiment the removal of Ne from the sample was continued for 45 days at room temperature, and the thermal expansion coefficient was then measured. The results obtained before and after alloying coincided in the whole temperature interval (Fig. 3, curve *1*). We can thus conclude that the C_{60} sample was completely free of neon. Desaturation for the same length of time was not sufficient to remove all argon from the sample.

Of interest are two features exhibited by the linear thermal expansion coefficient of Ne-alloyed C_{60}. First of all, at 6–12 K the $\alpha(T)$ values practically coincide for Ar- and Ne-saturated samples. Let us assume that Ar- and Ne-alloying increases the librational frequencies of the C_{60} molecules to such extent that the contribution of librations to the thermal expansion is negligible up to 12 K. Besides, it is natural to expect that the Ar and Ne impurities have negligible effect on the translational vibration of the lattice and their contribution to the thermal expansion. If this is correct, the thermal expansions of the Ne–C_{60} and Ar–C_{60} solutions and the contribution of the translational vibrations to the thermal expansion of pure C_{60} should all coincide in the 6–12 K region, where the contributions of librations and tunneling to $\alpha(T)$ are not observable. We tried to describe this contribution as

$$\Delta \alpha_{\text{trans}} = \gamma C(T/\Theta_D)/BV,$$

where γ is the Grüneisen coefficient; V is the molar volume of C_{60}; B is the bulk modulus of C_{60}, $C(T/\Theta_D)$ is the Debye heat capacity, and Θ_D is the Debye temperature. The calculation was made using $V = 416.7 \, \text{cm}^3/\text{mol}$ (Ref. 21) and $B = 10.3 \, \text{GPa}$.[22] γ and Θ_D were fitting parameters. The above expression could describe the experimental $\Delta \alpha_{\text{trans}}$ values quite well taking $\gamma = 2.68$ and $\Theta_D = 54$ K. γ is close to the corresponding values for rare-gas solids.[23] In the literature the Θ_D data for C_{60} vary widely. It follows from the analysis of the temperature dependence of heat capacity that $\Theta_D = 37$ K,[18] 50 K,[24,25] 60 K,[26] 80 K,[27] and 188 K.[28] Studies of the elastic properties of single-crystal C_{60} give $\Theta_D = 100$ K.[29] Even if we disregard the very high values $\Theta_0 = 188 \, \text{K}^{28}$ and $\Theta_D = 100$ K, where the error is high,[29] the scatter of the Θ_D values is still wide. The Debye temperatures obtained by the calorimetric method are highly sensitive to the impurities present in the fullerite and the technique employed to separate the contributions to the heat capacity. The Θ_D values obtained from ultrasound velocities are more reliable, since they are mainly determined by the translational vibrations of the lattice and are not very sensitive to impurities. According to the ultrasound data for single-crystal C_{60} at $T = 300$ K, $\Theta_D = 66$ K.[30] In Ref. 21 the data in the literature on ultrasound velocities of polycrystalline C_{60} were analyzed and extrapolated to low temperatures. The Debye temperature thus calculated at $T > 0$ is 55.4 K. This value of Θ_0 is very close to ours. We should, however, remember that in our case Θ_D is closer to its high-temperature limit Θ_∞. For rare-gas solids the difference between Θ_0 and Θ_∞ amounts to 10–12%.[23]

The above consideration suggests that our γ and Θ_D are quite realistic and thus support the assumption that curves *2* and *4* in Fig. 3 describes the contribution of translational vibrations to the thermal expansion coefficient of pure C_{60}.

Proceeding from this assumption, we can expect that the difference between curve *1* and curves *2* and *3* (Fig. 3) at $6-12$ K represents the librational contribution $\Delta\alpha_{\mathrm{lib}}$ to the thermal expansion coefficient of pure C_{60}. $\Delta\alpha_{\mathrm{lib}}$ is well described by the Einstein term with the characteristic Einstein temperature $\Theta_E = 39$ K. This value does not conflict with the above results.[18]

Another feature of the thermal expansion coefficient of the $Ne-C_{60}$ mixture is the increase (instead of the expected decrease) in $\alpha(T)$ at $2-5$ K after a 24-hour evacuation of Ne. The effect may be caused by a nonmonotonic dependence of the changes in $\alpha(T)$ upon the impurity concentration. Further quantitative studies of the concentration dependence of $\alpha(T)$ are called for to obtain more-certain information.

*E-mail: aleksandrovskii@ilt.kharkov.ua

[1] A. N. Aleksandrovskii, V. B. Esel'son, V. G. Manzhelii, A. Soldatov, B. Sundqvist, and B. G. Udovidchenko, Fiz. Nizk. Temp. **23**, 1256 (1997) [Low Temp. Phys. **23**, 943 (1997)].

[2] A. N. Aleksandrovskii, V. B. Esel'son, V. G. Manzhelii, A. Soldatov, B. Sundqvist, and B. G. Udovidchenko, Fiz. Nizk. Temp. **26**, 100 (2000) [Low Temp. Phys. **26**, 75 (2000)].

[3] V. Narayanamurti and R. O. Pohl, Rev. Mod. Phys. **42**, 201 (1970).

[4] Yu. A. Freiman, Fiz. Nizk. Temp. **9**, 657 (1983) [Sov. J. Low Temp. Phys. **9**, 335 (1983)].

[5] V. M. Loktev, Fiz. Nizk. Temp. **25**, 1099 (1999) [Low Temp. Phys. **25**, 823 (1999)].

[6] V. M. Loktev, Yu. G. Pogorelov, and J. N. Khalack, Fiz. Nizk. Temp. **27**, 539 (2001) [Low Temp. Phys. **27**, 397 (2001)].

[7] M. J. Rosseinsky, Mater. Chem. **5**, 1497 (1995).

[8] R. A. Assink, J. E. Schirber, D. A. Loy, B. Morosin, and G. Carlson, J. Mater. Res. **7**, 2136 (1992).

[9] Charles H. Pennington and Victor A. Stenger, Rev. Mod. Phys. **68**, 855 (1996).

[10] B. Morosin, J. D. Jorgenson, Simine Short, G. H. Kwei, and J. E. Schirber, Phys. Rev. B **53**, 1675 (1996).

[11] G. E. Gadd, M. James, S. Moricca, P. J. Evans, and R. L. Davis, Fullerene Sci. Technol. **4**, 853 (1996).

[12] G. E. Gadd, S. J. Kennedy, S. Moricca, C. J. Howard, M. M. Elcombe, P. J. Evans, and M. James, Phys. Rev. B **55**, 14794 (1997).

[13] G. E. Gadd, S. Moricca, S. J. Kennedy, M. M. Elcombe, P. J. Evans, M. Blackford, D. Cassidy, C. J. Howard, P. Prasad, J. V. Hanna, A. Burchwood, and D. Levy, J. Phys. Chem. Solids **58**, 1823 (1997).

[14] V. G. Manzhelii, Yu. A. Freiman, M. I. Klein, and A. A. Maradudin (Eds.), Physics of Cryocrystals, AIP Press, Woodbury, New York (1996).

[15] A. M. Tolkachev, A. N. Aleksandrovskii, and V. I. Kuchnev, Cryogenics **9**, 547 (1975).

[16] A. N. Aleksandrovskii, V. G. Gavrilko, V. B. Esel'son, V. G. Manzhelii, B. Sundqvist, B. G. Udovidchenko, and V. P. Maletskiy, Fiz. Nizk. Temp. **27**, 333 (2001) [Low Temp. Phys. **27**, 245 (2001)].

[17] W. P. Beyermann, M. F. Hundley, J. D. Thompson, F. N. Diederich, and G. Grüner, Phys. Rev. Lett. **68**, 2046 (1992).

[18] W. P. Beyermann, M. F. Hundley, J. D. Thompson, F. N. Diederich, and G. Grüner, Phys. Rev. Lett. **69**, 2737 (1992).

[19] J. E. Schirber, G. H. Kwei, J. D. Jorgensen, R. L. Hitterman, and B. Morosin, Phys. Rev. B **51**, 12014 (1995).

[20] J. E. Schirber, R. A. Assink, G. A. Samara, B. Morosin, and D. Loy, Phys. Rev. B **51**, 15552 (1995).

[21] N. A. Aksenova, A. P. Isakina, A. I. Prokhvatilov, and M. A. Strzhemechny, Fiz. Nizk. Temp. **25**, 964 (1999) [Low Temp. Phys. **25**, 724 (1999)].

[22] B. Sundqvist, O. Anderson, A. Lundin, and A. Soldatov, Solid State Commun. **93**, 109 (1995).

[23] Rare Gas Solids, M. L. Klein, and J. A. Venables (Eds.), Vol. 2, Academic Press, New York (1977).

[24] T. Atake, T. Tanaka, H. K. Kikuchi, K. Saito, S. Suzuki, I. Ikemoto, and Y. Ashiba, Physica C **185−189**, 427 (1992).

[25] T. Atake, T. Tanaka, H. Kawaji, H. K. Kikuchi, K. Saito, S. Suzuki, Y. Ashiba, and I. Ikemoto, Chem. Phys. Lett. **196**, 321 (1992).

[26] B. Sundqvist, Physica B **265**, 208 (1999).

[27] J. R. Olson, K. A. Topp, and R. O. Pohl, Science **259**, 1145 (1993).

[28] E. Grivei, B. Nysten, M. Gassart, A. Demain, and J.-P. Issi, Solid State Commun. **85**, 73 (1993).

[29] S. Hoen, N. G. Chopra, X.-D. Xiang, R. Mostovoy, Jianguo Hou, W. A. Vareka, and A. Zettl, Phys. Rev. B **46**, 12737 (1992).

[30] N. P. Kobelev, R. K. Nikolaev, Ya. M. Soĭfer, and S. S. Khasanov, Fiz. Tverd. Tela (St. Peterburg) **40**, 173 (1998) [Phys. Solid State **40**, 154 (1998)].

Structure, lattice parameters, and thermal expansion anisotropy of C$_{70}$ fullerite

A. P. Isakina, A. I. Prokhvatilov,* M. A. Strzhemechny, and K. A. Yagotintsev

B. Verkin Institute for Low Temperature Physics and Engineering, National Academy of Sciences of Ukraine, pr. Lenina 47, 61103 Kharkov, Ukraine

X-ray diffraction studies of the two low-temperature phases of especially pure polycrystalline C$_{70}$ fullerite are carried out in the temperature range 20–310 K. At room temperature a rhombohedral structure is established, and at $T < 276$ K a monoclinic structure. The volume jump at the low-temperature phase transition is determined to be ~ 8.5 cm^3/mole, or 1.7%. The temperature dependence of the lattice parameters and of the linear and volume thermal expansion coefficients is investigated in the two phases. For both the intermediate and the low-temperature modifications a substantial anisotropy of the thermal deformation of the crystals along individual crystallographic directions is observed. The results are analyzed with the use of previous structural studies. It is shown that in the absence of rotations at low temperatures the lattice is unstable to monoclinic distortions, the estimated sign and order of magnitude of which agree with the observations. © *2001 American Institute of Physics.* [DOI: 10.1063/1.1430849]

INTRODUCTION

Obtaining pure C$_{70}$ fullerite has long been a difficult problem. The presence of impurities, mainly components of the solvent or C$_{60}$ molecules, substantially complicates investigations of the structure, orientational phase transitions, and physical properties of C$_{70}$. Only the recently developed sublimation techniques permit one to obtain rather pure (more than 99.9%) samples of solid C$_{70}$.

The addition of ten carbon atoms to C$_{60}$ leads to significant qualitative changes in the properties of the molecules and the condensed phases formed by them. The molecules lose their nearly spherical icosahedral symmetry *Ih* and take the shape of an ellipsoid of revolution with symmetry D_{5h}. Unlike C$_{60}$, which has only one order–disorder phase transition at 260 K and two cubic phases, in pure C$_{70}$ fullerite one observes two first-order orientational phase transitions in the temperature interval 280–340 K and three equilibrium phases.[1] The presence of two phase transitions in C$_{70}$ and the lower symmetry of the two low-temperature orientationally ordered phases are mainly due to a change in the character and magnitude of the anisotropic intermolecular interaction as a result of the lower of the symmetry of the molecule in comparison with C$_{60}$.

The phase transitions and structure of the phases of C$_{70}$ fullerite have received considerable study and have been the subject of many papers. The results of previous structural studies done on samples of various composition and morphology and prepared by different methods differ strongly from one another. This has prompted us to analyze the rather large volume of structural data to arrive at a reasonable picture of the structural transformations in C$_{70}$ fullerite. Most of the structural data available before the start of our investigations are critically systematized in Table I. The conclusions of our analysis are set forth in the Introduction.

The phase transitions in C$_{70}$ fullerite, especially the high-temperature transition, are extremely sensitive to the presence of impurities, structural defects, and thermal stresses in the crystals, all of which shift these transitions to substantially lower temperatures. The high-temperature phase is orientationally disordered and, depending on the method of preparation and purity of the initial material, can have a close-packed cubic (fcc) or hexagonal (hcp) lattice. The practically equal probability of obtaining one or the other structure is due to the well-known small difference in energy of fcc and hcp lattices, with molecular layer stackings *abcabc* and *abab*, respectively.[4,21–23] For this reason it was for a long time impossible to give a final answer to the question of which of the close-packed structures of the high-temperature phase is stable. Fischer and Heiney[1] note that the fcc structure is more stable for purified, dry, and annealed samples at temperatures above 345 K, and practically none of the papers[1,2,4,10,11,26–28] has reported the observation of a transformation of the structure from the stacking sequence *abcabc* of the close-packed layers to *abab* stacking. At the same time, at high temperatures the transformation of the hcp to the fcc lattice occurs rather easily. These experimental results agree with the conclusions reached from calculations of the structure of C$_{70}$ by the molecular dynamics method.[29] However, there are also papers that point to the opposite conclusions. According to recent data,[23] when C$_{70}$ is evaporated at $T = 650$ K and condensed on a substrate at $T = 550$ K, hexagonal hcp single crystals are obtained, while for evaporation at $T = 450$ K and condensation on a substrate at $T = 300$ K it is predominantly cubic crystals of fcc symmetry that grow. Single crystals of hexagonal symmetry with a parameter ratio c/a close to the ideal (see Table I) have also been obtained at room temperature by growth from solution.[24] These last facts can be regarded as yet another confirmation of the smallness of the energy difference between these close-packed lattices. For this reason, the formation of one structure or the other on crystallization may depend on slight methodological or other experimental nuances. Both the equilibrium cubic fcc phase and the less stable hexagonal hcp phase have a high density of stacking

TABLE I. Studies of the structural characteristics of the crystalline phases of C_{70} fullerite.

No.	Method. Characteristics of the sample	T, K	Type of lattice, symmetry	Lattice parameters, Å	Source
1	X-ray, TEM, synchrotron. Polycrystal, from solution, purity >99%	440	Cubic fcc Hexagonal hcp	$a=15.01$ $a=10.62$, $c=17.31$, $c/a=1.630$	Vaughan *et al.* (1991) [Ref. 2]
2	X-ray. Single crystal, purity not reported	293	Cubic fcc	$a=14.96$	Fleming *et al.* (1991) [Ref. 3] Fisher and Heiney (1993) [Ref. 1]
3	X-ray, TEM. Single crystal, growth from the gas phase, 99.9%	≥293	Cubic fcc Hexagonal hcp-II $P6_3/mmc$	$a=14.96$ $a=10.56$, $c=17.18$, $c/a=1.627$	Verheijen *et al.* (1992) [Ref. 4]
		293	hcp-I $P6_3/mmc$	$a=10.11$, $c=18.58$, $c/a=1.838$	
		220 100	hcp (monoclinic) hcp (monoclinic)	$a=20.04$, $c=18.53$ $a=19.96$, $c=18.51$	
4	Electron microscopy, TEM. Single crystal from solution, >99%	293	Hexagonal hcp $P6_3/mmc$	$a=10.1\pm0.5$, $c=17.0\pm0.8$, $c/a=1.683$	Dravid *et al.* (1992) [Ref. 5]
5	Electron diffraction	300	Hexagonal hcp	$a=10.6\pm0.4$, $c=17.2\pm0.6$, $c/a=1.623$	Tomita *et al.* (1992) [Ref. 6]
	Single-crystal film, <1% C_{60}	104	Hexagonal hcp	$a_{104}/a_{300}=0.96$	
6	Powder x-ray diffraction.	near T_m	Cubic fcc	$a=14.87$	Kawamura *et al.* (1992) [Ref. 7]
	Other fullerenes prior to sublimation less than 4%	295	Rhombohedral	$a_h=9.93$, $c_h=27.31$	
7	X-ray.	293	Cubic fcc	$a_1=14.943(1)$, $a_2=14.898(6)$	Christides *et al.* (1993) [Ref. 8]
	Polycrystal, 98.5% (1.5% C_{60}), sublimation		Rhombohedral	$a=14.96(2)$, $\alpha=85.7(1)°$	
8	X-ray. Polycrystal, sublimation 723 K, deposition 473 K	293	Cubic hcp $Fm3m$	$a=14.89(1)$	Valsakumar *et al.* (1993) [Ref. 9]
	Polycrystal from solution	293	Hexagonal hcp $P6_3/mmc$	$a=10.53(1)$, $c=17.24(1)$, $c/a=1.637$	
9	Electron diffraction and electron microscopy, x-ray.	>337	Cubic fcc	$a=14.60$	van Tendeloo *et al.* (1993) [Ref. 10]
	Sublimation, >99.9%		Hexagonal hcp-II	$a=10.60$, $c=17.30$, $c/a=1.632$	
		<280	hcp-I	$c/a=1.82$	
10	X-ray. Polycrystal, sublimation, 99.9%	440 300	Cubic fcc $Fm3m$ Rhombohedral $R3m$	$a=15.01$ $a_h=10.128\pm0.0005$, $c_h=27.852\pm0.008$	Vaughan *et al.* (1993) [Ref. 11]
		15	Monoclinic $C2$, Cm, $P2_1$, or Pm	$a=9.9318\pm0.0007$, $b=10.0422\pm0.0012$, $c=27.774\pm0.003$, $\gamma=119.637°\pm0.003°$	
11	X-ray. Single crystal	295	Cubic fcc	$a=14.90(4)$	Meingast *et al.* (1993) [Ref. 12]
	Polycrystal, sublimation, purity of initial material >99.5% C_{70}		Cubic fcc + hexagonal hcp	$a=14.851(6)$	
12	X-ray. Polycrystal of C_{70}	290	Cubic fcc	$a=15.08$	Misof *et al.* (1993) [Ref. 13)]
	Polycrystal of C_{70}, irradiated by high-energy heavy ions	290	Cubic fcc→rhombohedral	$a=14.98$, $\alpha=85.6°$	
13	X-ray. Polycrystal, sublimation, 99.9%	293	Rhombohedral	$a=10.958$, $\alpha=55.04°$	Kawamura *et al.* (1994) [Ref. 14]
	$C_{70}+10\% C_{60}$		Cubic fcc + hexagonal hcp	$a=15.01$	
14	X-ray. Polycrystal, sublimation, C_{60} not detected	356	Cubic fcc	$a=14.974$	McGhie *et al.* (1994) [Ref. 15]
		381	Hexagonal hcp	$a=10.614$, $c=17.311$, $c/a=1.631$	
			Cubic fcc Hexagonal hcp	$a=14.980$ $a=10.606$, $c=17.266$, $c/a=1.628$	

TABLE 1. (*Continued.*)

No.	Method. Characteristics of the sample	T, K	Type of lattice, symmetry	Lattice parameters, Å	Source
15	X-ray. Polycrystal, purity not reported	293	Hexagonal hcp-II	$a=10.8$, $c=17.5$, $c/a=1.62$	Mitsuki *et al.* (1994) [Ref. 16]
			Hexagonal hcp-I	$a=10.1$, $c=18.7$, $c/a=1.85$	
16	X-ray. Single crystal	220	Orthorhombic *Pbnm*	$a=b=20.033$, $c=18.53$	van Smaalen *et al.* (1994) [Ref. 17]
17	X-ray. Polycrystalline film	<280 (251)	Deformed hexagonal hcp, analog of rhombohedral[4]	$a=c=19.6$, $b=18.5$	Ramasesha *et al.* (1994) [Ref. 18]
	Sublimation, purity not reported	290–350	Hexagonal hcp-I+hcp-II	$a=b=10.48$, $c=17.5$ ($c/a=1.67$) and $a=b=10.77$, $c=17.64$ ($c/a=1.638$)	
		373	Cubic fcc	$a=14.8$	
18	X-ray. Polycrystal and single crystal, initial purity $C_{70}>99.5\%$	295	Deformed hexagonal hcp-I	$a=10.11(1)$, $c=18.58(5)$, $c/a=1.84$	Meingast *et al.* (1994) [Ref. 19]
		383	Hexagonal hcp-II	$a=10.54(6)$, $c=17.07(7)$, $c/a=1.62$	
19	X-ray. Polycrystal, from solution, impurities <1%	300	Hexagonal hcp	$a=10.55(1)$, $c=17.27(1)$, $c/a=1.637$	Janaki *et al.* (1995) [Ref. 20]
		77	Hexagonal hcp	$a=10.45(1)$, $c=17.21(1)$, $c/a=1.647$	
	Powder, prepared by pulverizing single crystals, 99.99%	300	Rhombohedral	$a_h=10.13(1)$, $c_h=27.77(1)$	
			6% cubic fcc	$a=14.89(1)$	
		10	Monoclinic	$a=10.04$, $b=9.90$, $c=27.77$, $\gamma=119.64°$	
20	X-ray, synchrotron. Single crystal, sublimation, 99.99%	293	Hexagonal hcp	$a=10.104(5)$, $c=18.584(10)$, $c/a=1.839$	Blanc *et al.* (1994, 1996) [Refs. 21,22]
21	X-ray, SEM. Single crystal, sublimation at 923 K, deposition at 823 K	293	Deformed hcp	$a=10.10$, $c=18.55$, $c/a=1.837$	Komori *et al.* (1997) [Ref. 23]
	Sublimation at 723 K deposition at 573 K	293	Cubic hcp Rhombohedral	$a=10.55$ $a=11.03$, $\alpha=54.8°$	
22	X-ray. Polycrystal from solution	300	Hexagonal hcp $P6_3/mmc$	$a=10.593$, $c=17.262$, $c/a=1.629_5$	Ghosh *et al.* (1998) [Ref. 24]
		100	Monoclinic $P2_1/m$	$a=10.99$, $b=16.16$, $c=9.85$, $\beta=107.75°$	
23	Scanning, transmission electron microscopy and electron diffraction of nanoparticles, aerosol reactor method, purity $C_{70}>98\%$	300	Morphology—hexagonal shape of slab, icosahedral and 10-vertex particles;		Pauwels *et al.* (1999) [Ref. 25]
		100, 77	structure—cubic fcc, rhombohedral; large amount of twinning		

faults,[1,4] which have a noticeable influence on the diffraction pattern, phase transitions, and physical properties of the phases. Each of the two types of structure obtained upon crystallization of C_{70} leads to a different channel of phase transitions in the crystals as the temperature is lowered, with three-layer or two-layer stacking of the close-packed layers of molecules.

When the equilibrium fcc phase is cooled to temperatures below 340 K a freezing of the rotational motion of the molecules about the short axes occurs, and their long axes are oriented parallel to one of the body diagonals of the cube. The $Fm3m$ symmetry of the high-temperature cubic lattice is lowered to rhombohedral $R3m$. The stability of the intermediate rhombohedral phase is confirmed by experiments[8,30]

in which an fcc–rhombohedral phase transition is observed under hydrostatic pressure. The rhombohedral phase has also been brought about by irradiating fcc crystals by high-energy heavy ions.[13] When such samples are heated to 400 K the reverse, rhombohedral–fcc, phase transition takes place.

Further lowering of the temperature to $T < 280$ K leads to freezing of rotations around the long axes of the molecules as well. As a result, one observes a transformation of the rhombohedral to a monoclinic phase, the symmetry space group of which has not yet been established. All three phases preserve the basic structural motif of $abcabc$ stacking of close-packed layers along the principal directions of the crystals: along one of the body diagonals $\langle 111 \rangle$ of the cubic cell, along the rhombohedral axis, and along the monoclinic axis.[11] In the intermediate rhombohedral and low-temperature monoclinic phases the orientation of the long axes of the molecules is the same: they are perpendicular to the basal close-packed layers. When the pressure is raised from standard to 17 GPa[31] at room temperature, two more phase transitions are observed, at $P = (2.2 \pm 0.2)$ GPa and $P = (5.52 \pm 0.5)$ GPa, which has been attributed to further changes of the orientational order in C_{70} fullerite. In the case when the fullerite crystallizes in the less stable hexagonal hcp structure, there are again two phase transformations that occur as the temperature is lowered, involving the same sequential freezing out of the rotational degrees of freedom of the molecules about the short and long axes. However, all of these transformations take place on the basis of a structure with two-layer $abab$ stacking, and at the high-temperature transition near 337 K no global symmetry change occurs. The high-temperature and intermediate phases in this case have hexagonal lattices. The phase transition is accompanied only by an abrupt change in the ratio c/a from 1.63 to 1.82 (Ref. 4) as a result of the alignment of the long axes of the molecules along the c axis. As the temperature is lowered further, in the region around ~ 276 K a transition from the hexagonal to a monoclinic phase occurs, in which the rotation around the long axes of the molecules is frozen out. All three phases preserve the two-layer stacking, and the two low-temperature phases preserve the orientation of the long axes of the molecule.

In the high-temperature region a coexistence of the cubic and hexagonal phases is often observed in the initial samples. This circumstance and also the tendency toward substantial supercooling make for the presence of a number of nonequilibrium states at low temperatures in addition to the two stable series. In Ref. 4, five phases were observed: fcc at high temperatures; rhombohedral and ideal hcp-II with a ratio of lattice parameters $c/a = 1.63$; a deformed hcp-I phase with a ratio $c/a = 1.82$ at room temperature, and a monoclinic phase at low temperatures. Similar phases were also observed in Ref. 10, and the possibility of their formation was also shown by the calculations of Ref. 32 on the change in binding energy in C_{70} crystals as a function of the distance between nearest-neighbor molecules. According to the data of Ref. 24, coexistence of the monoclinic and ideal hexagonal phases is observed over a rather wide temperature interval 270–170 K. The transition to the monoclinic structure occurs directly from the ideal hcp phase without going through the intermediate deformed hexagonal phase with the

lattice parameter ratio $c/a = 1.82$. An orientational model of the phase transition is proposed. The very wide coexistence region of the two phases is explained by the creation of significant negative interphase stresses in the samples upon the nucleation and growth of the monoclinic phase. In this regard we note that in C_{60} fullerite the coexistence region of the two cubic phases at the 260 K orientational transition is much smaller,[33,34] not more than a few degrees. In Refs. 6 and 16 the fcc–rhombohedral phase transition was observed at 280 K on cooldown and at 240 K on warmup. It has been noted[1] that the phase transitions in C_{70} are especially sensitive to the rate of cooling but rather insensitive to the rate of heating. In calorimetric studies the rhombohedral–fcc phase transition on heating of the samples almost always occurred at 340 K, while on the reverse temperature path this transition was "frozen" by almost 50 K.

The substantial discrepancy in the data of different studies as to the phase transition temperatures and to the number and structure of the phases, even for studies done on samples of high purity, most likely results from the high sensitivity of the structural characteristics of C_{70} fullerite to the technological and thermal prehistory of the samples, to the value of the volume jumps at phase transitions, and to the character of the anisotropy of the thermal expansion of the phases, which is determined by their symmetry. A clear conception of the influence of the preparation technology on the morphology of the crystallites, their crystallinity, the type of structure and the structural perfection is given by electron-diffraction and electron-microscope studies[25] of nanoparticles of C_{60} and C_{70}.

Until recently, unfortunately, there were no such data on the temperature dependence of the lattice parameters and volumes of the equilibrium phases of C_{70} which could serve as a basis for more-concrete quantitative estimates and conclusions. The available data were limited to the temperature evolution of individual elements of the unit cell (the length of the body diagonal of the cube along $\langle 111 \rangle$, the distance between nearest neighbors in the (110) plane, the total volume of the cell), which were obtained in x-ray studies[8] in the temperature interval 5–470 K. Recently the temperature dependence of the lattice parameters of the monoclinic and hexagonal phases were obtained in the temperature interval 5–300 K.[24] However, from the data presented graphically in those papers it is not only impossible to determine the numerical values of the lattice parameters at individual temperature points or the value of the volume jump at the phase transition for further analysis but it is even impossible to assess the character of the thermal expansion along the different crystallographic directions. Also, and more importantly, those results pertain to the metastable two-layer structures.

The thermal expansion of C_{70} was investigated in Ref. 12 on polycrystalline and single-crystal samples by the method of high-resolution scanning dilatometry. The single-crystal samples had the fcc lattice, while the polycrystalline pressings contained both the fcc and hcp phases. The authors did not present their data on the character and value of the anisotropy of the expansion at the transition of the cubic crystals to the rhombohedral phase. The character of the anisotropy of the thermal expansion of C_{70} single crystals was

investigated in Ref. 19, but the samples had the hexagonal hcp symmetry.

In this paper we present the results of x-ray studies of the structure, lattice parameters, and thermal expansion coefficients of the two equilibrium low-temperature rhombohedral and monoclinic phases of C_{70} fullerite in the temperature interval 20–300 K. We determine the value of the volume jump at the low-temperature phase transition and investigate the anisotropy of the thermal expansion of the monoclinic and rhombohedral phases. We analyze the results in connection with the existing published data.

EXPERIMENTAL TECHNIQUES

We studied polycrystalline samples of C_{70} obtained by sublimation in vacuum. The purity of the samples was 99.98% or better. The x-ray diffractograms of the polycrystalline samples of C_{70} fullerite were obtained in the K_{α} radiation of the copper anode on a DRON-3M diffractometer equipped with a helium cryostat. As an example, in Fig. 1 we show a typical diffractogram for a temperature of 20 K, where there is every physical reason to expect degradation of the quality of the reflections. Diffractograms were taken over the range 20–300 K with a temperature step of 5–10 K, with the temperature stabilized at each point to within ± 0.05 K during the recording of the diffractograms over a time of ~ 0.5 h. The samples were C_{70} fullerite powder deposited in a thin layer (<1 mm) with the use of Ramsay vacuum grease on a flat copper substrate of the cryostat chamber, which was connected through a thermal switch to a helium vessel. The film of Ramsay grease held the powder sample on the vertical substrate and provided reliable thermal contact. It remained amorphous on cooling to the lowest temperatures and did not introduce any features in the diffraction pattern obtained from the fullerite. To obtain reliable data on the structure and lattice parameters of the low-temperature and intermediate phases at individual temperature points we took diffractograms over a wide interval of reflection angles 2Θ from $10°$ to $60–70°$. The lattice parameters were then calculated and averaged by the least-squares method using the entire set of experimental reflections. The change of the lattice parameters with temperature in the intervals between the chosen points was obtained from an analysis of the temperature dependence of the most characteristic and intense reflections for each of the phases, with their subsequent "tying in" to the values obtained at reference points. The error
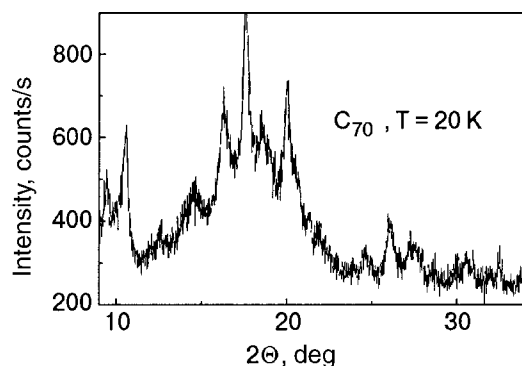

FIG. 1. X-ray diffractogram for C_{70} at $T=20$ K.

of determination of the lattice parameters was $\pm 0.02\%$. The temperature dependence of the lattice parameters and volumes made it possible to determine the volume jump at the low-temperature phase transition and also to calculate the coefficients of linear and volume thermal expansion of the low-temperature monoclinic and rhombohedral phases of C_{70} fullerite. The coefficients of linear and volume thermal expansion were obtained by differentiating the averaged temperature dependence of the lattice parameters and volumes. The error of their determination varied with increasing temperature, from 15–10% at $T<100$ K down to 5% in the rest of the region studied, where a relatively stronger temperature dependence of the quantities to be analyzed is observed.

RESULTS AND DISCUSSION

Our analysis of the diffractograms obtained for C_{70} fullerite showed that at room temperature the overwhelming majority of the x-ray reflections observed correspond to the rhombohedral lattice with parameters $a=10.083$ Å, $c=27.508$ Å in the hexagonal axes. However, in addition to the rhombohedral phase, the samples contained a small (up to 5%) amount of crystallites of hexagonal symmetry.

At temperatures $T<280$ K a lowering of the symmetry of the crystals occurs. Practically all of the reflections are satisfactorily indexed by choosing a monoclinic cell with the parameters $a=10.045$ Å, $b=9.936$ Å, $c=27.779$ Å, and $\gamma=119.63°$. It follows from a comparison of the diffractograms and the parameters of the rhombohedral and monoclinic cells that the phase transition deforms the initial lattice only a small amount and alters the diffraction pattern only slightly. A typical diffractogram of the low-temperature phase of C_{70} is presented in Fig. 1. The mismatch of the molecular (fivefold axis) and lattice (sixfold axis) symmetries in the basal plane leads to a slight monoclinic deformation of the lattice in the basal plane in the low-temperature phase. As a result of this type of deformation, the parameters a and b of the initial cell become unequal, and the angle between them deviates slightly from $120°$. Here, of course, the close-packed layers lose their hexagonal symmetry. This question is discussed in more detail in the Appendix. Similar transformation of the rhombohedral structure to the monoclinic occurs in other molecular crystals as well, in particular, in solid oxygen at the low-temperature phase transformation.[35]

X-ray studies of C_{70} fullerite in the interval 20–310 K have yielded the temperature dependence of the lattice parameters and of the molecular volumes and densities of the two low-temperature phases. From the averaged temperature dependence for each of these quantities we determined the coefficients of linear and volume thermal expansion. The temperature dependence of the lattice parameters of the intermediate rhombohedral phase α and of the low-temperature monoclinic phase α is presented in Figs. 2 and 3 and in Table II. The values obtained for the parameters at individual temperatures in the two phases are close to those found previously in a number of studies[7,11,20] (see also Table I).

The intermediate phase of C_{70} fullerite exhibited a characteristic substantially anisotropic variation of the lattice parameters with temperature: with increasing temperature the intermolecular distances in the close-packed basal planes in-
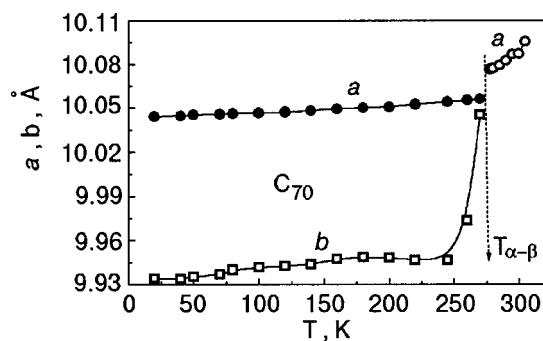
FIG. 2. Temperature dependence of the lattice parameters *a* and *b* of the monoclinic and rhombohedral phases of C_{70} fullerite.

creased intensively, while the interplane distances in the direction perpendicular to the basal planes decreases noticeably. This behavior corresponds to positive and negative thermal expansion coefficients, which are shown in Fig. 4a. Analogous behavior of the thermal expansion of the intermediate phase was found previously in dilatometric studies of hcp single crystals[19] and in an x-ray study.[24] The compression of the cell along the rhombohedral axis with increasing temperature may be a consequence of an increase in the amplitude of librations of the long axes of the C_{70} molecules (or growth of the angle of precession of the molecules around the rhombohedral axis), as a result of which an effective spheridization of the molecules occurs. The releasing of the orientational motion ultimately prepares the way for the transformation of the ordered $R3m$ structure of the intermediate phase to an orientationally disordered cubic lattice of symmetry $Fm3m$, with almost spherically disordered molecules. Studies[19] of hcp single crystals of C_{70} have established that the transition to the disordered phase is nevertheless accompanied by a giant change in the length of the crystals along the c axis. The relative decrease of the length reaches $\Delta L_c / L \simeq 6\%$. The inverse transition on heating is accompanied by the complete restoration of the length of the crystals. Roughly the same order of magnitude was obtained in Refs. 4 and 11 in an estimate of the parameter c in hcp crystals or the body diagonal $\langle 111 \rangle$ in fcc crystals as a result of the alignment of the long axes of the molecules along them. The deformation in the basal plane at the high-
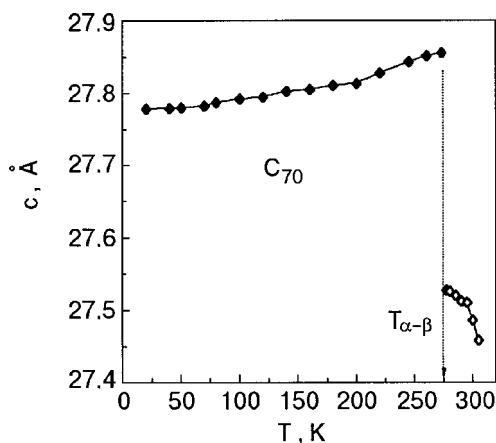

FIG. 3. Temperature dependence of the lattice parameter *c* of the monoclinic and rhombohedral phases of C_{70} fullerite.
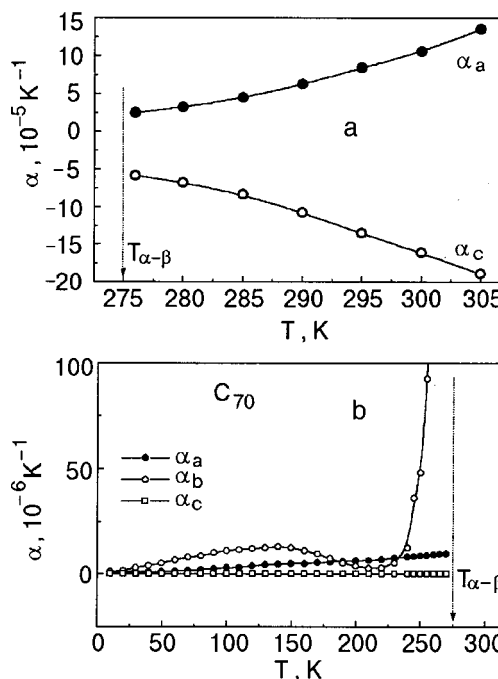

FIG. 4. Temperature dependence of the coefficients of linear thermal expansion of the rhombohedral (a) and monoclinic (b) phases of C_{70} fullerite.

temperature transition is considerably smaller, $\Delta L_a / L \simeq 2.5\%$, and of the opposite sign.[19] The hysteresis of the transition temperature was more than 50 K.

The lattice parameters of the low-temperature monoclinic phase (Figs. 2 and 3) also characteristically exhibit a large anisotropic change with temperature, especially in the close-packed basal plane ab (Fig. 4b). The anisotropy of the expansion is most clearly manifested as the phase transition temperature is approached (Fig. 4b). The parameters a and c are characterized by a positive change with increasing temperature in the entire existence region of the low-temperature phase. At the same time, in the direction of the b axis the positive growth at low temperatures goes to saturation in the region $T > 140$ K, after which there is possibly even a slight compression of the lattice, and then in the immediate vicinity of the phase transition an intense expansion of the lattice occurs (Fig. 4b). Thus, in the low temperature phase of C_{70} fullerite the orientational interaction of the molecules in the basal planes weakens long before the phase transformation, and this weakening promotes the release of the rotational motion of the molecules about their long axes and prepares the way for the transition to the intermediate rhombohedral phase.

When the orientational structure of C_{70} fullerite and our data on the temperature dependence of its lattice parameters in the two phases are compared with the existing data for cryocrystals,[35] a clear analogy is seen between the behavior of this substance and solid oxygen in the region of the low-temperature phase transition. At first glance this seems surprising, since the physical nature of the phase transitions in the substances being compared are quite different. In solid oxygen the low-temperature transformation is due to ordering of the magnetic moments of the molecules and to the formation of a quasi-two-dimensional antiferromagnetic phase on the basis of the monoclinic lattice. In the substance

TABLE II. Lattice parameters a, b, c, γ, molar volumes V, density ρ, and coefficients of linear α_a, α_b, α_c and volume β thermal expansion of C_{70} fullerite at various temperatures.

T, K	a	b	c	γ, deg	V, cm³/mole	ρ, g/cm³	α_a	α_b	α_c	β
		Å						10^{-6}, K⁻¹		
					α-phase					
20	10.045	9.936	27.779	119.63	483.79	1.737_9	—	—	—	—
30	10.045	9.936	27.780	119.63	483.82	1.737_8	0.9	3.1	0.11	4.2
40	10.045	9.937	27.780	119.63	483.85	1.737_7	0.9	4.3	0.12	5.3
50	10.045	9.937	27.781	119.63	483.87	1.737_6	0.9	5.2	0.11	6.4
60	10.045	9.938	27.782	119.63	483.94	1.737_4	1.3	6.5	0.12	7.9
70	10.046	9.938	27.783	119.63	483.99	1.737_2	1.6	0.8	0.12	9.7
80	10.046	9.939	27.783	119.63	484.06	1.737_0	2.1	8.5	0.13	10.3
90	10.046	9.940	27.784	119.63	484.12	1.736_7	2.5	10.4	0.15	12.5
100	10.046	9.941	27.785	119.63	484.20	1.736_4	2.9	11.6	0.17	13.2
110	10.047	9.942	27.787	119.63	484.33	1.736_0	3.2	11.6	0.20	15.8
120	10.047	9.944	27.788	119.63	484.42	1.735_6	3.7	12.2	0.22	16.1
130	10.048	9.945	27.790	119.63	484.54	1.735_2	4.2	12.6	0.23	17.4
140	10.048	9.946	27.792	119.63	484.67	1.734_8	4.6	13.1	0.26	18.1
150	10.049	9.948	27.794	119.63	484.82	1.734_2	4.9	12.6	0.28	18.4
160	10.049	9.949	27.796	119.63	484.90	1.733_9	5.1	11.2	0.29	17.3
170	10.050	9.950	27.799	119.63	485.04	1.733_4	5.4	9.5	0.31	15.6
180	10.050	9.950	27.802	119.63	485.15	1.733_0	5.6	7.4	0.32	13.3
190	10.051	9.950	27.804	119.62	485.24	1.732_7	5.8	5.1	0.32	11.6
200	10.051	9.951	27.806	119.62	485.34	1.732_4	6.2	3.8	0.33	10.4
210	10.052	9.950	27.808	119.62	485.41	1.732_1	6.4	2.7	0.31	9.2
220	10.053	9.950	27.810	119.61	485.50	1.731_8	7.2	2.8	0.34	9.6
230	10.053	9.950	27.813	119.61	485.59	1.731_5	7.6	5.3	0.37	13.2
240	10.054	9.951	27.816	119.60	485.73	1.731_0	8.1	12.6	0.36	23.6
245	10.055	9.952	27.817	119.59	485.83	1.730_6	8.4	36.2	0.38	44.8
250	10.055	9.954	27.819	119.59	486.03	$1,729_9$	8.6	48.2	0.37	67.2
255	10.055	9.956	27.820	119.59	486.19	1.729_3	9.4	92.5	0.41	105.3
260	10.056	9.966	27.822	119.59	486.74	1.727_4	9.2	155.6	0.41	164.5
265	10.056	9.974	27.823	119.58	487.16	1.725_9	9.4	180.5	0.42	190.8
270	10.057	9.982	27.825	119.58	487.65	1.724_1	9.7	260.7	0.41	270.3
274	10.057	9.994	27.826	119.58	488.38	1.721_6	10.5	305.7	0.43	315.5
					β-phase					
276	10.111	—	27.917	120	496.19	1.694_5	26.1	—	57.6	0.4
280	10.112	—	27.911	120	496.17	1.694_5	33.7	—	−67.8	1.3
285	10.114	—	27.900	120	496.18	1.694_4	44.9	—	−83.5	5.4
290	10.116	—	27.888	120	496.20	1.694_3	62.5	—	−107.2	17.3
295	10.120	—	27.870	120	496.26	1.694_2	84.5	—	−135.6	32.6
300	10.125	—	27.850	120	496.36	1.693_9	107.2	—	−160.8	50.5
305	10.131	—	27.855	120	496.51	1.693_4	125.3	—	−189.7	60.2

investigated here, however, both phase transitions are determined solely by the features of the anisotropic intermolecular interaction, which leads to a sequence of different types of orientational ordering of the C_{70} molecules. However, the observed similarity of the orientational structures and also of the temperature dependence of the structural parameters and the thermal expansion coefficients of the α and β phases of C_{70} and O_2 suggests that the character of the anisotropy of

the noncentral intermolecular interaction in the two phases of the substances considered are qualitatively similar. The structural characteristics of the phases of the substances O_2 and C_{70} display an explicit isomorphism, making even stronger hypotheses possible. Specifically, in view of the existing data for solid oxygen,[35–37] one can conjecture that the structure of α-C_{70} is substantially anisotropic and quasi-two-dimensional, with a strong interaction in the basal planes and a markedly weaker interplane interaction. The intermediate phase is analogous to β-O_2 over a rather wide interval of low temperatures. To confirm these ideas it will be necessary to investigate other physical characteristics of C_{70} fullerite which are especially sensitive to anisotropy of the coupling forces and of the crystal structure.

The data obtained here on the temperature dependence of the molar volume and of the coefficient of volume thermal expansion of the low-temperature and intermediate phases of C_{70} fullerite are presented in Figs. 5 and 6. In accord with these results both phases have a positive coefficient of volume expansion in their entire existence region. The α–β phase transition is accompanied by a positive volume jump of 8.5 cm³/mole, or 1.7%, in satisfactory agreement with the value $(\Delta V/V)_{\alpha-\beta} = 1.4\%$ presented in Ref. 19. The total change of the molar volume in the investigated temperature interval 20–310 K is 2.6%. It follows from our analysis of the data of Ref. 8 on the temperature dependence of the lattice volume (see Fig. 5) that $\Delta V/V$ is approximately 2.0% over this same temperature interval. Here, however, it should be kept in mind that Christides *et al.*[8] did not observe an explicit volume jump at the transition to the low-temperature monoclinic phase, which, as was mentioned in that article, arises at temperatures below 200 K, while in the interval 200–340 K the intermediate rhombohedral phase coexists with the supercooled high-temperature cubic fcc phase. As we see in Fig. 5, the difference of the molar volumes of C_{70} according to the data of the two studies (the present study and Ref. 8) at low temperatures is practically equal to the change in volume at the phase transition. This may mean that in Ref. 8 the intermediate phase was supercooled to the very lowest temperatures. Such a situation, which was also observed in Refs. 4, 6, 20, and 25, is mainly determined by the level of stresses emerging in the sample as a result of the large, substantially anisotropic (as was pointed out above) change of the structural parameters of the C_{70} crystals at the high-temperature β–γ phase transition and, possibly, by the presence of impurities. On the other hand, on the basis of the

FIG. 6. Temperature dependence of the coefficients of volume thermal expansion of the low-temperature and intermediate phases of C_{70} fullerite. For comparison, the data for C_{60} from Ref. 40 are shown by the dotted curve.

data of Ref. 8 on the temperature dependence of the distance between nearest-neighbor molecules in the basal plane and along the body diagonal of the pseudorhombohedral cell in the interval 80–490 K, we have estimated the volume jump at the β–γ transition and found, not surprisingly, a smaller volume jump, $(\Delta V/V)_{\beta-\gamma} \simeq 0.5\%$, than at the β–α transition. In this connection it should be noted that the ratio of the volume jumps at the phase transitions is qualitatively correlated with the corresponding ratio of the enthalpies of the phase transitions obtained from calorimetric measurements.[2,38,39] According to Ref. 2, the phase transitions observed at 276 and 337 K have enthalpies of transition equal to 3.5 and 2.7 J/g, while the data of Ref. 38 ($T_c = 280$ and 337 K) give 3.2 and 2.2 J/g, respectively. The presence of even a small amount of impurities in the initial materials from which the C_{70} crystals are grown apparently promotes the initial formation of the hcp phase, with a ratio of lattice parameters c/a close to the ideal value 1.63. As the temperature is subsequently lowered, there is a transition to the deformed hexagonal phase with a ratio $c/a = 1.82$–1.84, which is then observed down to the lowest temperatures or transforms to a two-layer monoclinic phase (see Table I). The molecules in this deformed hexagonal structure, as in the rhombohedral phase, are ordered and oriented with their long axes along the hexagonal axis c.

As to the deep supercooling of the partially ordered intermediate phase observed in a number of studies, wherein the rotation of the molecules about their long axes remains unfrozen, it can be assumed that an orientational glass phase forms in those samples. Apparently, this circumstance is responsible for the slight features observed in Ref. 8 on the temperature dependence of the volume (see Fig. 5) and the intermolecular distances of the rhombohedral cell in the region around 150 K.

Possible evidence of a high degree of disordering of the supercooled phase is the lower density of the β-C_{70} crystals as compared to the completely ordered monoclinic α phase. For example, the density of C_{70} calculated from the data of Ref. 8 at 100 K is equal to 1.686 g/cm³, which is approximately 2% smaller than our value $\rho = 1.736$ g/cm³ (see Table II) and, moreover, is 1.3% smaller than the density of C_{60} at this temperature.[40] At the same time, our results on the density are in good agreement with the data of Ref. 1 and have the expected relation to the density of the light fullerite C_{60}—in the entire investigated temperature interval the den-
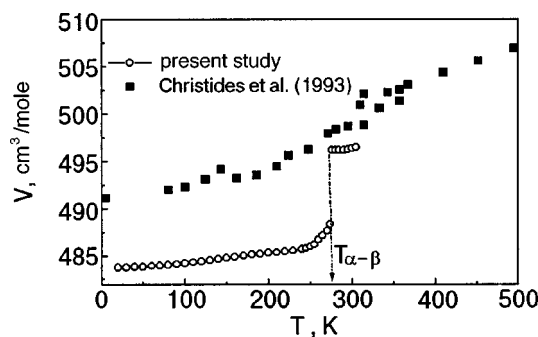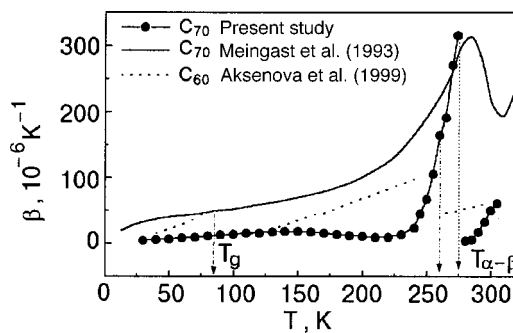

FIG. 5. Temperature dependence of the molar volume V of C_{70} fullerite in the region of the low-temperature and intermediate phases.

sity of C_{70} is systematically a little higher (on average by about 0.6%) than the density of C_{60}.

As we have said, the coefficients of thermal expansion of C_{70} fullerite have been measured previously by dilatometry method on polycrystalline and single-crystal samples.[12,19] Since both phases have a rather low lattice symmetry, and well-faceted single crystals of sufficiently large dimensions have not been obtained (the maximum size of the crystallites is 0.5–1 mm), it is extremely difficult to obtain reliable data to high accuracy with the use of this method. It is possibly for this reason that the measured values have a considerable discrepancy both for single crystals in different experiments and when data for single-crystal and polycrystalline samples are compared. We have made a comparison of our data on the temperature dependence of the coefficients of volume thermal expansion with the results of Ref. 12 for polycrystalline samples (see Fig. 6). This same plot also shows data which we obtained previously for the temperature dependence of the volume thermal expansion of C_{60} fullerite in x-ray diffraction studies on polycrystalline samples.[40] One can see the difference from the dilatometric measurements, in which the values of the coefficients of volume thermal expansion β are higher than our values in both the low-temperature and intermediate phases. The maximum of the dilatometric $\beta(T)$, corresponding to the phase transition point, is shifted significantly to higher temperatures relative to the equilibrium value ~ 275 K. The possible reason for this discrepancy may be the insufficiently small grain size of the polycrystalline samples, precluding reliable averaging and reducing the influence of the anisotropy of the expansion of the low-symmetry crystallites on the results of the dilatometric measurements. It is also possible that internal stresses are playing a role [in Ref. 12 the measurements were made on two-phase (fcc+hcp) polycrystalline samples obtained by pressing a powder at high pressures], the decrease of which with increasing temperature may give rise to a nonanharmonic component of the increase in the sample volume. An apparent indication of the presence of such stresses in the samples[12] is the aforementioned shift of the transition temperature. The temperature dependence of the coefficient of volume thermal expansion of C_{70}, as compared to C_{60} fullerite, has a more pronounced feature as the phase transition region is approached (see Fig. 6), a property which is characteristic of structural orientational phase transitions in pure cryocrystals.[36,37]

APPENDIX

Let us consider the anisotropic part of the interaction of C_{70} molecules in the hexagonal plane. In the simplest case the anisotropic part of the interaction of two C_{70} molecules with allowance for the fivefold symmetry can be written in the form of an "interaction of soft cog wheels":

$$v_{an} = -u_5 \cos 5(\varphi_1 + \varphi_2). \tag{A1}$$

Here u_5 is the amplitude of the interaction; the angles of rotation φ_i are measured from the intermolecular axis, which is taken to be the x axis. If the molecular axis is rotated by an angle Φ, then the anisotropy energy becomes

$$v_{an} = -u_5 \cos[5(\varphi_1 + \varphi_2) - 10\Phi]. \tag{A2}$$
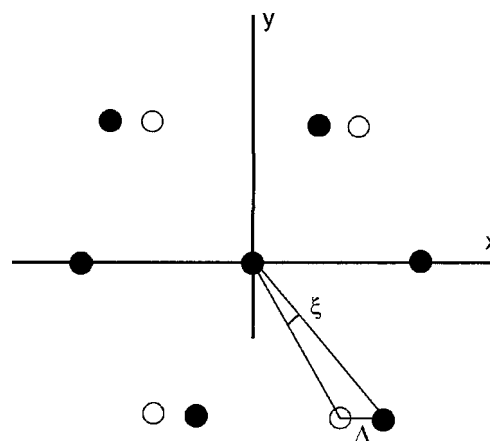

FIG. 7. Hexagonal plane of the rhombohedral or cubic phase, deformed by a monoclinic angular distortion ξ (Δ is the corresponding translational displacement): ●—molecules in the monoclinic phase; ○—in the rhombohedral phase.

An important circumstance is the choice of the number of independent angles φ in the unit cell. Calculations based on atom–atom potentials (of the Lennard-Jones type) between the C atoms of different C_{70} molecules with a minimization of the lattice energy have given either a monoclinic $P2_1/m$ or an orthorhombic $Pbnm$ (Ref. 42) structure with doubling along the b axis (in our setting). However, no such doubling is evidenced by experiment. Thus, if we assume that at the low-temperature structural transition the unit cell is not doubled, then from crystallographic considerations the angles φ of all the molecules in the crystal must be the same. This means that the anisotropic part of the interaction per molecule has the form

$$V_{an} = -\frac{u_5}{2} \sum_n \cos(10\varphi - 10\bar{\Phi}_n), \tag{A3}$$

where the summation is over the six nearest neighbors in the hexagonal plane. If the structure in the basal plane has strictly hexagonal symmetry, then $\bar{\Phi}_n = \pi n/3 (n=0,\ldots,5)$. If we assume that the structure has a monoclinic distortion described by an additional small displacement with respect to the angle ξ (see Fig. 7), then the new angular positions Φ_n in the sum (A3) will take on the following values: $\Phi_0 = 0$; $\Phi_{-3} = \pi$; $\Phi_n = \bar{\Phi}_n + \xi$ ($n=1,2,4,5$). Finally, for the anisotropic part we obtain

$$V_{an} = 4u_5 \sin 5\xi \sin(10\varphi - 5\xi). \tag{A4}$$

From this expression, in particular, it follows that in the framework of the ideal hexagonal symmetry in the plane ($\xi = 0$) the anisotropic interaction is equal to zero independently of the (identical) angle of rotation of the molecules. This indifferent equilibrium position with zero total energy is indicative of substantial frustration, since the minimum sum of the individual intermolecular interactions is equal to $-6u_5$. Second, negative values of ξ should cause a lowering of the energy, limited by the elastic energy, which in general form can be written (per molecule) as

$$V_{el} = \frac{1}{2}G\xi^2, \tag{A5}$$

where G is the specific stiffness coefficient, which can be expressed in terms of the elements of the tensor c_{ij} and in order of magnitude is close to the shear modulus.

Taking the sum of expressions (A4) and (A5) as the resulting energy, one easily finds that the equilibrium conditions $\partial V/\partial \xi = 0$; $\partial V/\partial \varphi = 0$ give the following equations for ξ and φ:

$$\sin 5\xi \cos(10\varphi - 5\xi) = 0; \tag{A6}$$

$$20u_5 \cos 5\xi + G\xi = 0. \tag{A7}$$

The desired solution giving the lowering of the energy is satisfied approximately ($5\xi \leqslant 1$) at the following values of the parameters:

$$\xi \simeq -\frac{20u_5}{G}; \quad \varphi = \frac{\pi}{20} + \frac{\xi}{2}. \tag{A8}$$

Let us estimate the value of the monoclinic distortions. We consider the hexagonal plane perpendicular to the monoclinic axis (see Fig. 7). The nonzero components of the strain tensor in the case of monoclinic distortion are easily expressed in terms of the value of the shift Δ of the molecular rows along the x axis:

$$\frac{\partial u_x}{\partial y} = \frac{2\Delta}{a\sqrt{2}}, \tag{A9}$$

where a is the distance to the nearest neighbor (for an angular displacement $\xi = \sqrt{3}\Delta/2a$). Unfortunately, the elastic constants for the rhombohedral and monoclinic phases are unknown, as are estimates of the rotational barrier u_5. Calculations exist[43] for the high-temperature ($T = 400$ K) cubic phase. Judging from the values of the macroscopic moduli, those calculations overestimate the values. For example, for C_{60} at room temperature the overestimate is by 17% (Ref. 44), and for C_{70} at room temperature it is 68% (Ref. 45). If it is assumed that the energetics in the basal plane in the rhombohedral and cubic phases are not strongly different, then the stiffness coefficient in (A5), after straightforward transformations, can be expressed in terms of the elastic constants c_{ik} for the cubic phase:

$$G = \frac{16}{27}\left[\frac{7}{9}c_{11} + 2c_{12} + \frac{2}{3}c_{44}\right]. \tag{A10}$$

If for u_5 we take the analogous value of u_6 for C_{60}, i.e., $u_5 = 0.33$ meV, then we obtain for the angular shift $\xi = \gamma - 120° = -0.305°$, which agrees in order of magnitude with the experimental value N 0.36–0.37° (see Table I). In view of the crudity of the assumptions and estimates, this agreement can be considered satisfactory. We stress that the conclusions reached here do not rely on a specific form of the molecular interaction but are based on the observable macroscopic characteristics.

*E-mail: prokhvatilov@ilt.kharkov.ua

[1] J. E. Fischer and P. H. Heiney, J. Phys. Chem. Solids **54**, 1725 (1993).
[2] G. B. M. Vaughan, P. A. Heiney, J. E. Fischer, D. E. Luzzi, D. A. Ricketts-Foot, A. R. McGhie, Y.-W. Hui, A. L. Smith, D. E. Cox, W. J. Romanov, B. N. Allen, N. Coustel, J. P. McCauley, and A. B. Smith III, Jr., Science **254**, 1350 (1991).
[3] R. M. Fleming, A. R. Kortan, B. Hessen, T. Siegrist, F. A. Thiel, P. Marsh, R. C. Haddon, R. Tycko, G. Dabbagh, M. L. Kaplan, and A. M. Mujsce, Phys. Rev. B **44**, 888 (1991).
[4] M. A. Verheijen, H. Meekes, G. Meijer, P. Bennema, J. L. de Boer, S. van Smaalen, G. van Tendeloo, S. Amelinckx, S. Muto, and J. van Landuyt, Chem. Phys. **166**, 287 (1992).
[5] V. P. Dravid, X. Lin, H. Zhang, Sh. Liu, and M. M. Kappes, J. Mater. Res. **7**, 2440 (1992).
[6] M. Tomita, T. Hayashi, P. Gaskell, T. Marurio, and T. Tanaka, Appl. Phys. Lett. **61**, 1171 (1992).
[7] H. Kawamura, M. Kobayashi, and Y. Akahama, Solid State Commun. **83**, 563 (1992).
[8] C. Christides, I. M. Thomas, T. J. S. Dennis, and K. Prassides, Europhys. Lett. **22**, 611 (1993).
[9] M. C. Valsakumar, N. Subramanian, M. Yosuf, P. Ch. Sahu, Y. Hariharan, A. Bharathi, V. S. Sastry, J. Janaki, G. V. N. Rao, T. S. Radhakrishnan, and C. S. Sundar, Phys. Rev. B **48**, 9080 (1993).
[10] G. van Tendeloo, S. Amelncks, J. L. de Boer, S. van Smaalen, M. A. Verheijen, H. Meekes, and G. Meijer, Europhys. Lett. **21**, 329 (1993).
[11] G. B. M. Vaughan, P. A. Heiney, D. E. Cox, J. E. Fischer, A. R. McGhie, A. L. Smith, R. M. Stogrin, M. A. Cichy, and A. B. Smith III, Jr., Chem. Phys. **178**, 599 (1993).
[12] C. Meingast, F. Gugenberger, M. Haluska, H. Kuzmany, and G. Roth, Appl. Phys. A: Solids Surf. **56**, 227 (1993).
[13] K. Misof, P. Fratzi, and G. Vogl, Europhys. Lett. **21**, 586 (1993).
[14] H. Kawamura, Y. Akahama, M. Kobayashi, H. Shinohara, and Y. Saito, J. Phys. Soc. Jpn. **63**, 2445 (1994).
[15] A. R. McGhie, J. F. Fisher, P. A. Heiney, P. W. Stephens, R. L. Cappelletti, D. A. Neumann, W. H. Mueller, H. Mohn, and H.-U. ter Meer, Phys. Rev. B **49**, 12614 (1994).
[16] T. Mitsuki, Y. Ono, H. Horiushi, J. Li, N. Kino, K. Kishio, and K. Kitazawa, Jpn. J. Appl. Phys. **33**, 6281 (1994).
[17] S. van Smaalen, V. Petricek, J. L. de Boer, M. Dusek, M. A. Verheijen, and G. Meijer, Chem. Phys. Lett. **223**, 323 (1994).
[18] S. K. Ramasesha, A. K. Singh, R. Seshadri, A. K. Sood, and C. N. R. Rao, Chem. Phys. Lett. **220**, 203 (1994).
[19] C. Meingast, F. Gugenberger, G. Roth, M. Haluska, and H. Kuzmany, Z. Phys. B: Condens. Matter **95**, 67 (1994).
[20] J. Janaki, G. V. N. Rao, V. S. Sastry, H. Hariharan, T. S. Radhakrishnan, C. S. Sundar, A. Bharati, M. C. Valsaku-mar, and N. Subramanian, Solid State Commun. **94**, 37 (1995).
[21] E. Blanc, H.-B. Burgi, R. Restori, D. Schwarzenbach, P. Stellberg, and P. Venugopalan, Europhys. Lett. **27**, 359 (1994).
[22] E. Blanc, H.-B. Burgi, R. Restori, D. Schwarzenbach, and Ph. Oshsenbein, Europhys. Lett. **33**, 205 (1996).
[23] R. Komori, T. Nagaosa, T. Hatae, and Y. Miyamoto, Jpn. J. Appl. Phys. **36**, 5600 (1997).
[24] G. Ghosh, V. S. Sastry, C. S. Sundar, and T. S. Radhak-rishnan, Solid State Commun. **105**, 247 (1998).
[25] B. Pauwels, D. Bernaerts, S. Amelincks, G. Van Tendeloo, J. Joutsensaari, and E. I. Kauppinen, Cryst. Growth **200**, 126 (1999).
[26] G. B. M. Vaughan, P. A. Heiney, D. E. Cox, A. R. McGhie, D. R. Jones, R. M. Stogrin, M. A. Cichy, and A. B. Smith III, Jr., Chem. Phys. **168**, 185 (1992).
[27] S. Muto, G. van Tendeloo, and S. Amelncks, Philos. Mag. **67**, 443 (1993).
[28] M. A. Green, M. Kurmoo, P. Day, and K. Kikkuchi, J. Chem. Soc. Chem. Commun. **20**, 1676 (1992).
[29] M. Sprik, A. Cheng, and M. L. Klein, Phys. Rev. Lett. **69**, 1660 (1992).
[30] H. Kawamura, M. Kobayashi, Y. Akahama, H. Shinohara, H. Sato, and Y. Saito, Solid State Commun. **83**, 563 (1992).
[31] A. A. Maksimov, K. P. Meletov, Yu. A. Osip'yan, I. I. Tartakovskiĭ, Yu. V. Artemov, and M. A. Nudel'man, JETP Lett. **57**, 816 (1993).
[32] D.-H. Oh and Y. H. Lee, Phys. Rev. Lett. **75**, 4230 (1995).
[33] S. V. Lubenets, V. D. Natsik, L. S. Fomenko, A. P. Isakina, A. I. Prokhvatilov, M. A. Strzhemechnyĭ, and N. A. Aksenova, Fiz. Nizk. Temp. **23**, 338 (1997) [Low Temp. Phys. **23**, 251 (1997)].
[34] P. Wochner, X. Xiong, P. C. Chow, and S. C. Moss, Phys. Rev. B **55**, 5678 (1997).
[35] I. N. Krupskiĭ, A. I. Prokhvatilov, Yu. A. Freĭman, and A. I. Erenburg, Fiz.

Nizk. Temp. **5**, 271 (1979) [Sov. J. Low Temp. Phys. **5**, 130 (1979)].

[36] V. G. Manzhelii, A. I. Prokhvatilov, V. V. Gavrilko, and A. P. Isakina, *Structure and Thermodynamic Properties of Cryocrystals*, Begell House Inc., New York (1998).

[37] B. I. Verkin and A. F. Prikhot'ko (eds.), *Cryocrystals* [in Russian], Naukova Dumka, Kiev (1983).

[38] E. Grivei, B. Nysten, M. Cassart, J.-P. Issi, C. Fabre, and A. Rassat, Phys. Rev. B **47**, 1705 (1993).

[39] J. Sworakowski, K. Palewska, and M. Bertault, Chem. Phys. Lett. **220**, 197 (1993).

[40] N. A. Aksenova, A. P. Isakina, A. I. Prokhvatilov, and M. A. Strzhemechnyĭ, Fiz. Nizk. Temp. **25**, 964 (1999) [Low Temp. Phys. **25**, 724 (1999)].

[41] B. J. Nelissen, P. H. M. van Loosdrecht, M. A. Verheijen, A. van der Avoird, and G. Meijer, Chem. Phys. Lett. **207**, 343 (1993).

[42] D. F. Agterberg, W. Que, and M. B. Walker, Chem. Phys. Lett. **213**, 207 (1993).

[43] W. Sekkal, H. Aourag, and M. Certier, Comput. Mater. Sci. **9**, 295 (1998).

[44] N. P. Kobelev, R. K. Nikolaev, Ya. M. Soĭfer, and S. S. Khasanov, Fiz. Tverd. Tela (St. Petersburg) **40**, 173 (1998) [Phys. Solid State **40**, 154 (1998)].

[45] A. Lundin, A. Soldatov, and B. Sundqvist, Mat. Res. Soc. Symp. Proc. **359**, 555 (1995).

Translated by Steve Torstveit

LOW-TEMPERATURE PHYSICS OF PLASTICITY AND STRENGTH

Kinetics of the creep deformation jump stimulated by the superconducting transition in β-tin

V. P. Soldatov,* V. D. Natsik, and G. I. Kirichenko

B. Verkin Institute for Low Temperature Physics and Engineering National Academy of Sciences of Ukraine, pr. Lenina 47, 61103 Kharkov, Ukraine

The kinetics of the deformation increment stimulated by the superconducting transition in β-tin is investigated. Experiments are done on single crystals of high purity strained in the transient creep regime at a temperature of 1.6 K. It is found that the creep after the N–S transition occurs in stages, and the features of the strain-rate versus strain curves are analyzed within each stage. An interpretation of the experimental results is proposed, based on a kink mechanism for the motion of dislocations through the Peierls barriers with allowance for the influence of quantum fluctuations and electron drag on the nucleation of kinks. © *2001 American Institute of Physics.* [DOI: 10.1063/1.1430850]

INTRODUCTION

The transition of a metallic superconductor from the normal to the superconducting state (N–S transition) during low-temperature creep is accompanied by a sharp increase of the creep rate and strain.[1,2] This response of the creep to a change of electronic state is one of the manifestations of the plastification effect—the softening of a metal due to a superconducting transition.[3,4] The study of this effect affords a unique opportunity to elucidate the role of the conduction electrons in the processes of low-temperature plasticity in metals.

At the present time the generally accepted point of view is that the first cause of the increased plasticity of metals at an N–S transition is a sharp decrease of the electron drag on the dislocations as a result of the Cooper condensation of conduction electrons. However, a consistent description of the effect must take into account not only the influence of the superconducting transition on the viscous drag on dislocations but also two other important circumstances: the specifics of the dislocation processes occurring under conditions of various types of mechanical testing (creep, active deformation, stress relaxation), and the type and strength of the barriers governing the mobility of dislocations over macroscopic path lengths (Peierls barriers, local impurity barriers, large-scale internal stresses).

Attempts to take into account individual aspects of the complicating circumstances listed above in the theoretical treatment of the plastification effect have led to the construction of several models and mechanisms, differing from one another in the details, for the influence of the conduction electrons on the kinetics of plastic deformation: dynamic,[4–6] quasidynamic,[7–9] thermal-fluctuation,[10] thermoinertial,[11] and quasistatic.[12–14] As a rule, in each of these models the influence of the Cooper condensation of electrons on the kinetics of overcoming the barriers preventing the glide of dislocations is treated in its own way, and the magnitude of the effects caused by this influence is different in each case. In addition, even in the earliest stage of research on the plastification effect, attempts were made to select from this panoply a main model in the framework of which a consistent explanation of the whole set of observed phenomena might be obtained. However, as the experimental data accumulated, it became increasing obvious that for such a complex process as plastic deformation one can hardly expect there to be a universal model. A more realistic situation is that different mechanisms of softening and combinations of these mechanisms come into play as the deformation process unfolds.

For this reason it becomes important to assess experimentally the roles and efficiencies of the proposed softening mechanisms in real deformation processes, and to obtain information about the hierarchy of these processes and their relative role in different stages of plastic flow. This is a particularly topical problem in relation to those metallic superconductors for which the type of barriers resisting the glide of dislocations at low temperatures is known. An example is single-crystal β-tin deformed in the slip system $(100)\langle010\rangle$: in this case the role of these barriers is played by the Peierls potential relief, and plastic deformation takes place by a simple elementary event: the nucleation of kink pairs and their subsequent spreading apart along the dislocation lines.[15,16]

Pure single crystals of β-tin (99.9995%) oriented for predominant slip in the system $(100)\langle010\rangle$ maintain a high plasticity and smooth flow down to a temperature of 0.5 K, making them unique objects for studying the mechanisms of low-temperature deformation in crystals with high Peierls barriers. The combined influence of quantum and thermal fluctuations and also of electron drag on the motion of dislocations through the Peierls barriers in the superconducting and normal states of β-tin under conditions of active deformation has been studied in detail in Ref. 16.

The kinetics of the motion of the dislocations and the

change of the kinetics upon an N–S transition under conditions of low-temperature creep have certain peculiar features, the manifestation of which in tin single crystals of high purity were first observed in Ref. 17. The goal of the present study was to carry out an experimental study and an analysis of the time dependence of the creep deformation "jump" caused by the superconducting transition in single-crystal samples of pure β-tin at a temperature of 1.6 K. It is shown that the observed jumplike growth of the deformation at the N–S transition in pure tin occurs in stages and is due to the occurrence of two successive dislocation processes of a dynamic and of a fluctuational nature.

1. EXPERIMENTAL TECHNIQUES

The single crystals for this study were grown from a 99.9995% pure stock by a modified Bridgman method in batches of 10 from a single bar.[18] They had the shape of double lobes (in the jaws of the strain testing machine) with a working region of rectangular cross section with dimensions of $25 \times 5 \times 1.5$ mm. The longitudinal axis of the sample was along the $\langle 110 \rangle$ direction, ensuring the most favorable conditions for slip in the system $(100)\langle 010 \rangle$.

The samples to be strained were placed inside a superconducting solenoid and were subjected to tensile creep at a temperature of $1.6 \text{ K} < T_c$ ($T_c = 3.72 \text{ K}$ is the temperature of the transition of tin to the superconducting state). The state of the electronic subsystem in the sample was changed by turning on (normal state) or off (superconducting state) the longitudinal magnetic field of the solenoid at a field strength $H > H_c$ ($H_c = 309 \text{ G}$ is the critical field for the destruction of superconductivity).

The deforming stress on the samples was increased in small steps of size $\Delta\tau = 0.1–0.4$ MPa. The strain increment $\Delta\varepsilon(t)$ corresponding to each stress increment was recorded automatically on an ÉPP-09 electronic potentiometer which was connected to a highly sensitive pickup and registered the relative change in the length of the sample with an accuracy of 5×10^{-5}. Simultaneously the deformation signal was sent to an N 370/1 fast XY recorder, where, after additionally amplification and a $2–16\times$ expansion of the time scale, at a rate set by the speed of the carriage of the XY recorder. The latter could be changed in a regular way between the limits $2 \times 10^{-2}–4$ cm/s.

Until the yield point τ_0 was reached, the sample was strained in the normal state. The strain increments corresponding to the load increment applied in that stage ensured an elastic change in the shape of the sample, which corresponded to a specific (Γ-shaped) character of the curves of the strain increment $\Delta\varepsilon(t)$ and to an absence of sensitivity to the N–S transition (see Fig. 1). After the yield point τ_0 was reached, a pronounced transient stage appeared on the creep curves, corresponding to developed plastic flow. At the point when a certain specified strain rate $\dot\varepsilon_N$ was reached on the creep curves in the normal state, the sample was brought to the superconducting state. The additional strain $\delta\varepsilon_{NS}(t)$ accompanying this transition was recorded by both a coarse and a sensitive (in the fast-sweep mode) chart recorder (Figs. 2, 3, and 4). The transitions were brought above at different values of the creep rate $\dot\varepsilon_N$ and different degrees of total
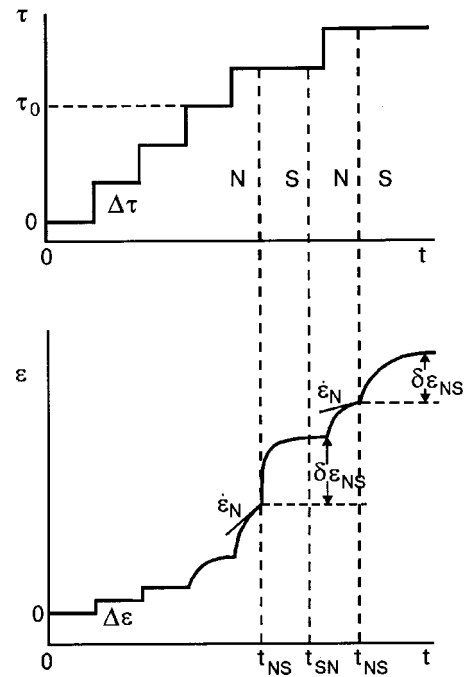

FIG. 1. Diagram of the load $\tau(t)$ and the strain $\varepsilon(t)$ of the samples under conditions of multiple N–S transitions.

strain ε of the sample, and the $\delta\varepsilon_{NS}(t)$ curves thus obtained were subjected to computer processing and analysis.

2. EXPERIMENTAL RESULTS

The influence of the superconducting transition on the transient creep process in the tin samples is illustrated by Fig. 2a. For a qualitative ("coarse") description of the effect one can talk of a sharp (almost instantaneous) increase in the creep rate, $\delta\dot\varepsilon_{NS} = \dot\varepsilon_S - \dot\varepsilon_N$ at the time (t_{NS}) of the N–S tran-
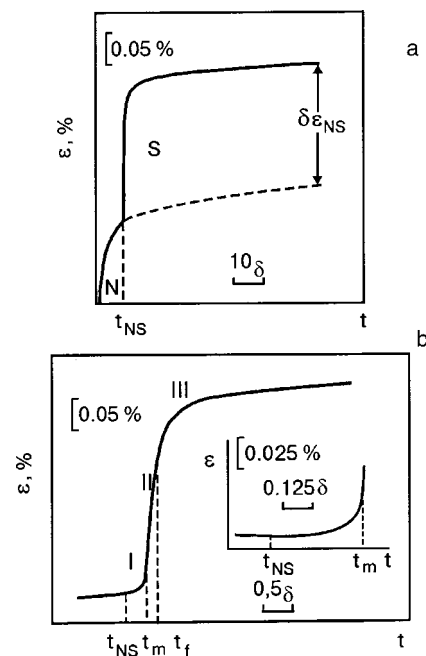

FIG. 2. Influence of a single N–S transition on the creep curve of samples of β-tin: a—strain increment $\delta\varepsilon_{NS}(t)$ in a slow sweep; b—fast sweep of the strain growth at the jump; t_{NS}, t_m, and t_f are the boundaries of the different stages of strain growth.

sition and a subsequent rapid (almost jumplike) strain increase $\delta\varepsilon_{NS}(t)$. However, a rapid sweep of the creep curve $\varepsilon(t)$ reveals the presence of stages in the deformation process after the N–S transition (Fig. 2b). The stages within the strain "jump" $\delta\varepsilon_{NS}(t)$ may be characterized by the following points in time:

t_{NS}—the time of the transition of the sample to the superconducting state, which is automatically fixed by the turning on of the magnetic field;

t_m—the time at which the strain rate in the S state reaches its maximum value $\max\dot{\varepsilon}_S$;

t_f—the time at which the sharp decrease of the creep rate in the S state begins; it corresponds to a change in the character of the time dependence of the creep.

In stage I (from t_{NS} to t_m) the strain occurs with a certain delay relative to the N–S transition, but at the end of this stage the strain occurs at a rapidly increasing rate (see the inset in Fig. 2b). After reaching its maximum value, the creep rate begins to slow, but the degree of slowing is substantially different in the intervals $t_m < t < t_f$ (stage II) and $t > t_f$ (stage III).

It should be noted that the duration of stages I and II depends on the conditions of plastic deformation prior to the N–S transition, e.g., on the value of the creep rate $\dot{\varepsilon}_N$ at the time t_{NS} and the value of the total strain ε accumulated in the sample up until that time. In particular, under certain conditions the duration of each of these stages can individually be so short that the corresponding stage can be regarded as practically absent. The different types of time dependence of $\delta\varepsilon_{NS}(t)$ are presented in Figs. 3 and 4.

Figure 3 shows the fast sweep of the strain increments $\delta\varepsilon_{NS}(t)$ for substantially different values of the creep rate $\dot{\varepsilon}_N$ in the normal state but at close values of the total strain of the sample prior to the transition (the curves were taken in succession). For $\dot{\varepsilon}_N = 2 \times 10^{-4}\,\text{s}^{-1}$ (curve *1*) the delay stage I is practically absent, and a large part of the strain in the jump is accumulated during stage II and only a small fraction in stage III. Decreasing the rate $\dot{\varepsilon}_N$ to $6 \times 10^{-5}\,\text{s}^{-1}$ results in the appearance of a delay, decreases the amount of strain in stage II, and increases the fraction of the strain occurring in stage III (curve *2*). Finally, decreasing $\dot{\varepsilon}_N$ further to 2

FIG. 4. Influence of the total deformation of the sample preceding the N–S transition on the growth kinetics of the creep deformation at the jump: a—near the yield point; b—near the breaking strain.

$\times 10^{-6}\,\text{s}^{-1}$ leads to significant growth of stage I and the practically complete vanishing of stage II.

Figure 4 shows the increments $\delta\varepsilon_{NS}(t)$ at identical values of the rate $\dot{\varepsilon}_N$ but for very different degrees of preliminary strain: near the yield point (Fig. 4a), and at strains close to failure of the sample (Fig. 4b). Increasing the degree of preliminary strain leads to a significant decrease in the value of the jump $\delta\varepsilon_{NS}$ and all of its components, with a noticeable widening of the time interval of the transition stage I.

The results presented here provide grounds for proposing that the kinetics of plastic deformation at the jump induced by the N–S transition is governed by several processes, so that the growth of $\delta\varepsilon_{NS}(t)$ occurs in stages. The role of these processes can vary under the influence of different factors and can cause corresponding changes in the character of the time dependence of the jump $\delta\varepsilon_{NS}(t)$. The observed influence of the rate and degree of preliminary strain on the stages of the jump is apparently a reflection of this circumstance.

3. DISCUSSION OF THE RESULTS

Let us discuss the possible processes that could be responsible for the appearance of the individual stages in the growth of the strain $\delta\varepsilon_{NS}(t)$ after the N–S transition, basing our discussion on the general relationships in the dislocation kinetics of plastic flow of tin and the consequences implied by these relationships.

3.1. First stage

According to Ref. 19, the appearance of the first (transition) stage in the development of the strain increment $\delta\varepsilon_{NS}(t)$ is due to a change in the regime of fluctuational motion of dislocations through the barriers as a result of the sudden change of the electron drag. When the steady regime of dislocation flow is disrupted, the characteristic time for establishment of a new steady regime (i.e., the relaxation time for the translational motion of dislocations) should be equal in order of magnitude to the average time for a dislocation to overcome an individual barrier. The delay time thus determined, $t_d = t_m - t_{NS}$, is a function of the effective stress τ_N^* prior to the change of state of the sample, the strain rate $\dot{\varepsilon}_N$ preceding the N–S transition, and the difference or ratio
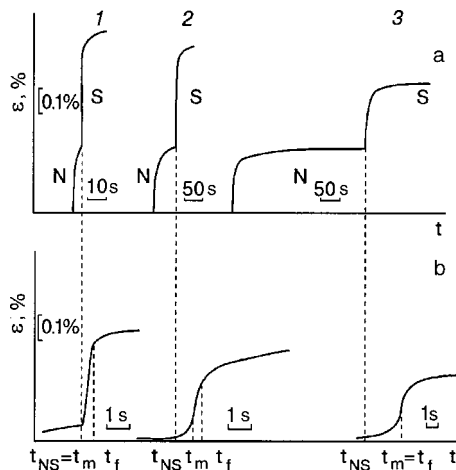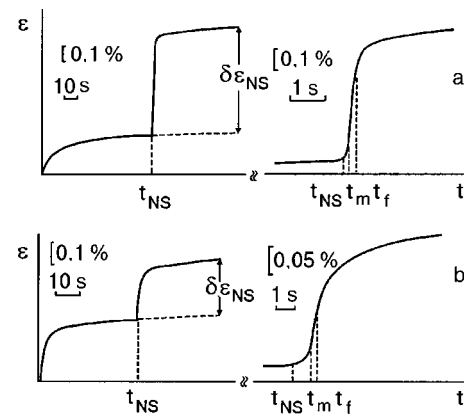

FIG. 3. Influence of the creep rate $\dot{\varepsilon}_N$ preceding the transition of the sample from the normal to the superconducting state, on the kinetics of the strain growth at the jump $\delta\varepsilon_{NS}(t)$: slow (a) and fast (b) sweeps of the jump.

of the coefficients of electron drag on dislocations in the normal and superconducting states, B_N and $B_S = 2B_N[1 + \exp(\Delta/kT)]^{-1}$, where $\Delta = \Delta(T)$ is the energy gap of the superconductor.[1)]

Experimentally the delay of the strain jump was first observed in a study of the softening effect in lead and indium single crystals in Refs. 20 and 21. It was shown in Ref. 21 that the behavior of this parameter is well described by the theory of the delay developed in Ref. 19. It is natural to assume that in the case of tin as well, the presence of the first stage on the $\delta\varepsilon_{NS}(t)$ curve can be attributed to the occurrence of a transient process during which the ensemble of mobile dislocations undergoes a transition from the steady regime of dislocation motion in the normal state to a steady regime in the superconducting state. We use this assumption for interpreting the delay phenomenon observed in the present study.

The rate of plastic deformation of a pure (impurity-free) single crystal of β-tin is governed by the Peierls potential relief, and the plastic flow occurs through processes of nucleation, dynamic spreading, and annihilation of kink pairs on the dislocations.[15,16] The action of the kink mechanism results in displacement of the dislocation line from one trough of the Peierls relief to another under the influence of an effective stress $\tau^* = \tau - \tau_i(\varepsilon)$; here τ is the deforming stress, and $\tau_i(\varepsilon)$ is the characteristic value of the internal stresses, which grows with increasing plastic deformation ε. In this case the role of the relaxation time for the translational motion of dislocations is played by the average time for a dislocation line to pass through an individual barrier of the Peierls relief.

Under the conditions of the extremely low crystal temperature $T = 1.6$ K realized in our experiments, creep occurs under the influence of effective stresses τ^* having values of the order of the Peierls stress τ_P, and the nucleation of kink pairs on the dislocations is governed predominantly by quantum fluctuations (the quantum-mechanical tunneling effect), while the influence of thermal activation is weak (practically negligible). The average steady velocity V of the dislocations is given as a function of the effective stress τ^* in this case by the expression[16]

$$V(\tau^*) = a\left(\frac{\nu_0 \nu_k}{b}\right)^{1/2} \exp\left[-\frac{Q_0}{2s_0}\left(\delta_\tau + \delta_\tau^{3/4}\frac{\Theta_B}{\Theta_P}\right)\right],$$

$$\delta_\tau = 1 - \frac{\tau^*}{\tau_P}. \tag{1}$$

Here a and b are the period of the Peierls relief and the magnitude of the Burgers vector of the dislocation, respectively, Q_0 is the quasiclassicality parameter for the process of tunnel nucleation of kink pairs, ν_0 is the characteristic frequency of the oscillations of a dislocation in a valley of the Peierls relief, Θ_P and Θ_B are the characteristic temperatures associated with the zero-point oscillations of the dislocations in the valley of the Peierls relief and with the damping of these oscillations by the electron viscosity, respectively, ν_k is the velocity of a dislocation kink along the dislocation line, and $s_0 \approx 0.9$ is a numerical parameter. The argument of the exponential function in (1) is written in the linear approximation in the small parameter Θ_B/Θ_P, which for tin in the

normal state has a value of the order of 0.1 and decreases sharply on transition to the superconducting state.

In Ref. 16 it was also shown that for the steady tunneling motion of a macroscopic flux of dislocations of density ρ in the Peierls relief, the values of the effective stress τ^* and the rate of plastic deformation $\dot\varepsilon = \rho b V(\tau^*)$ are connected by the relations

$$\delta_\tau = \frac{2s_0 A}{Q_0}\left[1 - \left(\frac{Q_0}{2s_0 A}\right)^{1/4}\frac{\Theta_B}{\Theta_P}\right],$$

$$A = \ln\left[\frac{ab\rho}{\dot\varepsilon}\left(\frac{\theta_0 \nu_k}{b}\right)^{1/2}\right]. \tag{2}$$

The following empirical estimates have been obtained[16] for the parameters of the theory which appear in formulas (1) and (2): $Q_0 = 500$, $\Theta_P = 3.3$ K, and in the normal state $\Theta_B = \Theta_{B_N} = 0.4$ K. In addition, we note that the characteristic temperature Θ_B is proportional, and the kink velocity ν_k inversely proportional, to the electron drag coefficient B of the dislocation, and therefore the values of these parameters in the normal ($\Theta_B = \Theta_{B_N}$, $\nu_k = \nu_{kN}$) and superconducting ($\Theta_B = \Theta_{B_S}$, $\nu_k = \nu_{kS}$) states at equal values of the effective stress, $\tau_N^* = \tau_S^*$, are connected by the relations

$$\frac{\Theta_{B_N}}{\Theta_{B_S}} = \frac{\nu_{kS}}{\nu_{kN}} = \frac{1 + \exp(\Delta/kT)}{2}. \tag{3}$$

Following the ideas set forth above, we shall take for the delay time t_d the average time for the motion of a dislocation between valleys of the Peierls relief, $t_d = a/V$, in the superconducting state ($\Theta_B = \Theta_{B_S}$, $\nu_k = \nu_{kS}$) under the influence of an effective stress τ_N^* which has been established at the time t_{NS}. The values of the parameter $\delta_\tau = \delta_{\tau N}$ corresponding to the value τ_N^* are determined by formulas (2) with the set values $\Theta_B = \Theta_{B_N}$, $\nu_k = \nu_{kN}$, and $\dot\varepsilon = \dot\varepsilon_N$. Thus we obtain from formula (1) the following expression for the delay time:

$$t_d = \left(\frac{b}{\nu_0 \nu_{kS}}\right)^{1/2}\exp\left[\frac{Q_0}{2s_0}\left(\delta_{\tau N} + \delta_{\tau N}^{3/4}\frac{\Theta_{B_S}}{\Theta_P}\right)\right]. \tag{4}$$

Since $\Theta_{B_S} \ll \Theta_{B_N} \ll \Theta_P$, for estimating the value of $\delta_{\tau N}$ from formula (2) and the argument of the exponential function in formula (4), we can neglect the contribution from electron drag. In this approximation $Q_0\delta_{\tau N} = 2s_0 A_N$, and we obtain the following simple expression for the delay time, giving its dependence on the strain rate $\dot\varepsilon_N$ and the dislocation density ρ:

$$t_d = \frac{ab\rho}{\dot\varepsilon_N}\left(\frac{\nu_{kN}}{\nu_{kS}}\right)^{1/2} = ab\left[\frac{1 + \exp(\Delta/kT)}{2}\right]^{-1/2}\frac{\rho}{\dot\varepsilon_N}. \tag{5}$$

Formula (5) gives a qualitative estimate for the delay time and explains the two features observed in the experiments:

—the inverse proportionality of t_d to $\dot\varepsilon_N$ explains the increase of the duration of the delay stage I as the creep rate $\dot\varepsilon_N$ prior to the N–S transition is decreased;

—the increase in the duration of stage I at high degrees of deformation can be interpreted as a consequence of the growth of the dislocation density ρ.

3.2. Second and third stages

The experiment shows that stage II of the increment $\delta\varepsilon_{NS}(t)$ of the creep deformation after the superconducting transition is manifested most clearly at rather high creep rates $\dot\varepsilon_N$, when stage I becomes negligible. Thus the values of $\dot\varepsilon_N$ correspond to values of the effective stress τ_N^* which are extremely close to the value of the Peierls stress τ_P. It is natural to assume that under these conditions the substantial increase in the velocity of individual dislocations as a result of the N–S transition will destroy the stability of the tunneling regime of dislocation flow and transfer a substantial fraction of the dislocations into the regime of dynamic above-barrier flow. This "breakoff" of the tunneling flow at the N–S transition is promoted by two factors: the substantial nonuniformity of the internal stresses τ_i in the volume of the sample, as a result of which in individual regions $\tau^* = \tau - \tau_i \gtrsim \tau_P$ and the dislocations move in the dynamic regime even before the N–S transition; inertial effects, the role of which increases strongly in the superconducting state.[22]

Thus the existence of stage II, with large values of the creep rate $\delta\dot\varepsilon_{NS}$, at large $\dot\varepsilon_N$ may be the result of a realization, over a certain time interval $t_f - t_m$, of a regime of high-velocity above-barrier motion of the dislocation flux. However, this time interval should have a finite length, since, as a result of the strain hardening the internal stresses increase as the deformation increases, leading to a decrease of the effective stress and to an increase in the dislocation flux in the tunneling flow regime again (stage III for $t > t_f$).

For comparison of the ideas set forth above with the experimental data, it is necessary to consider separately the time dependence of the creep deformation $\delta\varepsilon_{NS}(T)$ for the regimes of tunneling and dynamic motion of the dislocations. In the regime of tunneling motion the dependence of the average velocity $V(\tau^*)$ of the dislocations on the effective stress is given by relation (1), while for the dynamic regime this dependence has the form

$$V(\tau^*) = \frac{b\tau^*}{B}. \tag{6}$$

It is well known that an analytical description of the process of low-temperature creep $\varepsilon(t)$ reduces to the solution of the basic kinetic equation of dislocation plasticity,

$$\dot\varepsilon = \rho b V[\tau - \tau_i(\varepsilon)], \tag{7}$$

in which $\tau_i(\varepsilon)$ is expressed in the linear approximation

$$\tau_i(\varepsilon) = \tau_{i0} + \kappa\varepsilon. \tag{8}$$

Here κ is the hardening coefficient, and τ_{i0} is the value of the internal stresses corresponding to the start of the creep curve.

The creep due to the dynamic motion of dislocations, according to relations (6)–(8), is described by the equation

$$\dot\varepsilon(t) = \frac{\rho b^2 \tau_0^*}{B} - \frac{\rho b^2 \kappa}{B}\varepsilon(t), \quad \tau_0^* = \tau - \tau_{i0}. \tag{9}$$

In this same approximation we obtain the following equation from relations (1), (2), (7), and (8) for the regime of tunneling creep:

$$\ln\varepsilon(t) = \ln\left\{ \frac{\rho a \sqrt{b\,v_0 v_k}}{\exp[(Q_0/2s_0)(\delta_{\tau 0} + \delta_{\tau 0}^{3/4}\Theta_B/\Theta_P)]} \right\}$$

$$- \frac{\kappa Q_0}{2s_0 \tau_P}\varepsilon(t), \quad \delta_{\tau 0} = 1 - \frac{\tau_0^*}{\tau_P}. \tag{10}$$
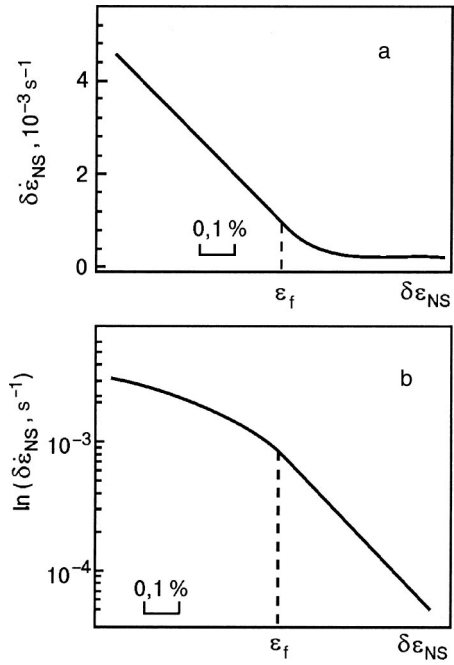

FIG. 5. Experimental curves of $\delta\varepsilon_{NS}(t)$, plotted in the coordinates $\delta\dot\varepsilon_{NS} - \delta\varepsilon_{NS}$ (a) and $\ln(\delta\dot\varepsilon_{NS}) - \delta\varepsilon_{NS}$ (b).

As we have said, stage II on the $\delta\varepsilon_{NS}(t)$ curve is most clearly expressed at rather high values of $\dot\varepsilon_N$, when stage I is practically absent (Fig. 3a). Numerical differentiation of $\delta\varepsilon_{NS}(t)$ in this case leads to the creep curves plotted in Fig. 5 in the coordinates $\delta\dot\varepsilon_{NS} - \delta\varepsilon_{NS}$ and $\ln\delta\dot\varepsilon_{NS} - \delta\varepsilon_{NS}$. Figure 5a shows the two-stage character of the creep curve and the linear relation between the creep rate and the strain in stage II ($t_{NS} < t < t_f$), corresponding to the equation of dynamic creep (9). In Fig. 5b we see that for times $t > t_f$ ($\delta\varepsilon_{NS} > \varepsilon_f$) the logarithm of the creep rate varies in proportional to the strain, and, consequently, in stage III the strain increment is described by the equation of tunneling creep (10).

The results of the above analysis permit the conclusion that the strain increment $\delta\varepsilon_{NS}(t)$ in the second and third stages is due to two successively operating processes:

—dynamic glide of dislocations as a result of the sharp decrease of the electron drag under conditions when $\tau_N^* \to \tau_P$ and the tunneling regime of motion loses stability;

—tunneling glide of dislocations, which is restored as a result of the strain hardening.

The strain increment in stage II is given by the solution of equation (9), and that in stage III by the solution of equation (10). However, in an analytical description of these stages a certain care must be exercised: generally speaking, there are no grounds for assuming that the effective value of the parameters ρ and κ have the same values for the two stages.

We note in concluding this Section that formula (5), which describes the delay time, and Eq. (10), which describes the process of fluctuational creep, were obtained for the limiting case of purely quantum motion of dislocations through Peierls barriers. It is assumed that the mobility of dislocations is determined solely by the tunnel nucleation of kink pairs, while the influence of thermal fluctuations on this process is neglected completely. In this limiting case a tem-

perature dependence of the characteristics of the creep appears only in the superconducting state of the metal owing to the temperature dependence of the coefficient of electron drag on the dislocations, $B_S(T)$. In the present paper this approach is justified by the use of the results of the theory of Ref. 16 for interpreting the experiments done at a temperature $T = 1.6$ K, which is considerably lower than the characteristic quantum temperature $\Theta_P = 3.3$ K. One expects that at higher temperatures the staged character of the creep jump after the N–S transition, $\delta\varepsilon_{NS}(t)$, and the characteristics of the individual stages will manifest a significant temperature sensitivity due not only to the temperature dependence of $B_S(T)$ but also to the growing influence of thermal activation on the process of nucleation of dislocation kinks. The theory developed in Ref. 16 contains all of the necessary prerequisites for describing such a sensitivity.

It should also be noted that the staged character of the creep curve can be observed not only after the stimulating effect of a superconducting transition on the creep but also after the rapid application to the sample of a sufficiently large (in magnitude) additional mechanical load $\Delta\tau$. There is no doubt that the study of the fine details of the low-temperature transient creep curves will yield extremely interesting and rich information about the microscopic mechanisms governing the mobility of dislocations.

The authors propose to continue their investigation of the problems mentioned above in future studies.

4. CONCLUSION

In this study we have obtained new experimental data on the influence of the superconducting transition on the kinetics of plastic deformation of a metal (pure β-tin) under conditions of transient creep. We have shown that the N–S transition at a constant temperature $T = 1.6$ K $< T_c$, brought on by turning on a magnetic field $H > H_c$, leads to a sharp increase in the creep deformation $\delta\varepsilon_{NS}(t)$, and that the "jump" in $\delta\varepsilon_{NS}(t)$ takes place in several stages. In the general case one can distinguish three stages on the $\delta\varepsilon_{NS}(t)$ curve: a delay stage I, a dynamic stage II, and a fluctuational stage III. The duration and differential characteristics of each of these stages depend substantially on the creep rate prior to the N–S transition and on the value of the total plastic deformation of the sample.

The analysis and interpretation of the experimental data were done on the basis of the theoretical results of a previously published paper by the authors.[16] In that paper it was shown that the plastic deformation of pure β-tin at temperatures of the order of 1 K is governed by a kink mechanism of motion of the dislocations in the Peierls relief, and the nucleation of kinks on the dislocations is due to quantum fluctuations—the process of tunneling penetration of short segments of a dislocation line through a single barrier of the Peierls relief. In the framework of the ideas developed in Ref. 16, the individual stages of the creep "jump" $\delta\varepsilon_{NS}(t)$ can be given the following physical interpretation:

—The existence of stage I is due to the finite value of the relaxation time for translational motion of a dislocation flux in the Peierls relief, and the value of the delay time can be regarded as an estimate of the mean time of motion of an individual dislocation through a single barrier of the Peierls relief.

—Stage II is manifested as a result of the disruption of the fluctuational regime of dislocation flow on account a change in the electronic state and the transition of a rather large fraction of the dislocations to the regime of dynamic (above-barrier) motion.

—Stage III is a consequence of the reestablishment of the fluctuational regime of dislocation motion as a result of the influence of the strain hardening on the dislocation mobility.

Thus a detailed study of the time dependence of the creep jump stimulated by a superconducting transition in a metal gives diverse and extremely interesting information about the microscopic mechanisms governing the mobility of dislocations in a metal under conditions of deep cooling, in particular, about the influence of quantum fluctuations and electron viscosity on the motion of dislocations.

*E-mail: vsoldatov@ilt.kharkov.ua

[1])The given explanation of the delay stage, strictly speaking, presupposes that the time of transition of the sample to the superconducting state in the experiment is registered to high accuracy. Otherwise it is possible to have situations in which a certain part of the delay time is the time for expulsion of the magnetic flux from the sample.

[1] I. A. Gindin, B. G. Lazarev, Ya. D. Starodubov, and V. P. Lebedev, Dokl. Akad. Nauk SSSR **188**, 803 (1969) [Sov. Phys. Dokl. **14**, 1011 (1970)].

[2] V. P. Soldatov, V. I. Startsev, and T. I. Vainblat, Phys. Status Solidi B **37**, 47 (1970).

[3] V. I. Startsev, V. Ya. Il'ichev, and V. V. Pustovalov, *Plasticity and Strength of Metals and Alloys at Low Temperatures* [in Russian], Metallurgiya, Moscow (1975).

[4] M. I. Kaganov, V. Ya. Kravchenko, and V. D. Natsik, Usp. Fiz. Nauk **111**, 655 (1973) [Sov. Phys. Usp. **16**, 878 (1974)].

[5] M. I. Kaganov and V. D. Natsik, JETP Lett. **11**, 379 (1970).

[6] G. P. Huffman and N. Louat, Phys. Rev. Lett. **24**, 1055 (1970).

[7] M. Suenaga and J. M. Galligan, Scr. Metall. **4**, 697 (1970).

[8] A. V. Granato, Phys. Rev. Lett. **27**, 660 (1971).

[9] G. Kostorz, Phys. Status Solidi B **58**, 9 (1973).

[10] V. D. Natsik, Zh. Éksp. Teor. Fiz. **61**, 2540 (1971) [Sov. Phys. JETP **34**, 1359 (1972)].

[11] A. I. Landau, Phys. Status Solidi A **61**, 655 (1980).

[12] V. L. Indenbom and Yu. Z. Éstrin, JETP Lett. **17**, 568 (1973).

[13] É. A. Pashitskiĭ and A. M. Gabovich, Fiz. Met. Metalloved. **36**, 186 (1973).

[14] V. E. Miloshenko, A. M. Roshchupkin, and G. V. Shunin, Fiz. Tverd. Tela (St. Petersburg) **19**, 840 (1997) [Phys. Solid State **19**, 485 (1997)].

[15] G. I. Kirichenko, V. D. Natsik, and V. P. Soldatov, Fiz. Met. Metalloved. **63**, 386 (1987).

[16] V. D. Natsik, G. I. Kirichenko, V. V. Pustovalov, V. P. Soldatov, and S. É. Shumilin, Fiz. Nizk. Temp. **22**, 965 (1996) [Low Temp. Phys. **22**, 740 (1996)].

[17] V. P. Soldatov, V. I. Startsev, and G. I. Shklyarevskaya, Fiz. Nizk. Temp. **1**, 1311 (1975) [Sov. J. Low Temp. Phys. **1**, 629 (1975)].

[18] Yu. G. Kazarov, in *Physics of the Condensed State* [in Russian], Kharkov (1973), issue 11, p. 100.

[19] V. D. Natsik, Phys. Status Solidi A **14**, 271 (1972).

[20] I. A. Gindin, B. G. Lazarev, Ya. D. Starodubov, and V. P. Lebedev, Fiz. Met. Metalloved. **29**, 826 (1970).

[21] V. P. Soldatov, V. I. Startsev, T. I. Vainblat, and L. A. Danilenko, Phys. Status Solidi B **53**, 261 (1972).

[22] T. Suzuki and H. Koizumi, Philos. Mag. A **67**, 1153 (1993).

Translated by Steve Torstveit

Low-temperature mechanical hysteresis in superelastic In−Pb alloys

L. S. Fomenko,* V. D. Natsik, and S. V. Lubenets

B. Verkin Institute for Low Temperature Physics and Engineering, National Academy of Sciences of Ukraine, pr. Lenina 47, 61103 Kharkov, Ukraine

Mechanical hysteresis caused by pseudotwinning in In–Pb alloys with concentrations of 6, 8, and 11.6 at.% Pb is investigated in the temperature range 1.7–180 K. The parameters of the hysteresis are estimated: the thermodynamic stress τ_T responsible for the reversibility of plastic deformation (superelasticity) and the friction stress τ_f characterizing the resistance exerted by the crystal lattice and its defects to the motion of twin boundaries. It is shown that the parameters of the mechanical hysteresis are determined by athermal processes: the fraction of the sample that has gone into the twin (or, on unloading, to the parent) orientation depends solely on the value of the applied stress. With increasing lead concentration the value of τ_T increases and τ_f decreases. One of the main conditions for the appearance of superelasticity is the inequality $\tau_T > \tau_f$. The hardening of superelastic alloys under cyclic loading is investigated (up to 300 cycles). In alloys with 8 at.% Pb the cyclic loading leads to a slight expansion of the hysteresis loop. For the alloy with 6 at.% Pb there is typically a strong distortion of the hysteresis loop, with the appearance of a transition-hardening part with a large coefficient of work hardening. An analytical description of the cyclic deformation diagrams of a superelastic alloy is proposed. © *2001 American Institute of Physics.* [DOI: 10.1063/1.1430851]

1. INTRODUCTION

In our previous studies[1,2] we found that single crystals of In–Pb alloys containing 6 and 8 at.% Pb at temperatures $T \lesssim 180$ K manifest the property of superelasticity, i.e., reversibility of large plastic deformations. It was established that the superelasticity effect in In–Pb alloys is unmistakably due to twinning and reversible motion of the boundaries of plane-parallel twin layers in them.

A preliminary study of diffuse x-ray scattering indicates that these alloys are locally ordered solid solutions: a short-range order of the clusterization type is formed in them. As was shown by Cahn,[3] twinning in ordered alloys, which occurs on systems characteristic for the disordered state, inevitably leads to the formation of pseudotwins having a crystal lattice structure different from that of the matrix. As a result, the chemical potential of a pseudotwin is higher than that of the matrix, and their difference determines the driving force—the thermodynamic stress τ_T that brings about the reverse process, untwinning, when the crystal load is removed.

The motion of twin boundaries both during twinning and during untwinning is resisted by a friction force due to potential barriers created by the crystal lattice and its defects. On loading, the external stress τ is directed so as to overcome the thermodynamic stress τ_T and the friction stress τ_f. During unloading, the reverse motion of the twin boundaries occurs under the influence of the thermodynamic stress, which counteracts the friction stress and the external stress. It follows that the stresses for the onset of twinning τ_t and untwinning τ_u can be written in the form[4,5]

$$\tau_t = \tau_T + \tau_f, \tag{1}$$

$$\tau_u = \tau_T - \tau_f. \tag{2}$$

Relations (1) and (2) can be applied to describe the twinning and untwinning processes occurring in the absence of hardening. Figure 1 shows a diagram of an idealized hysteresis loop. Such loops arise in rather perfect crystals of highly concentrated In–Pb alloys, whereas for the majority of materials, closed mechanical hysteresis loops are observed only under conditions of a sign-varying load.[6]

The loop illustrated in Fig. 1 reflects the situation that when the crystal stress reaches the value $\tau_T + \tau_f$ a simultaneous rearrangement of the structure of the entire single crystal to the twin structure occurs. This corresponds to a value of the shear strain equal to the twin shear $\gamma_{max} = s \approx 0.15$ for In and the solid solutions under discussion. The reverse process (recovery of the initial dimensions of the
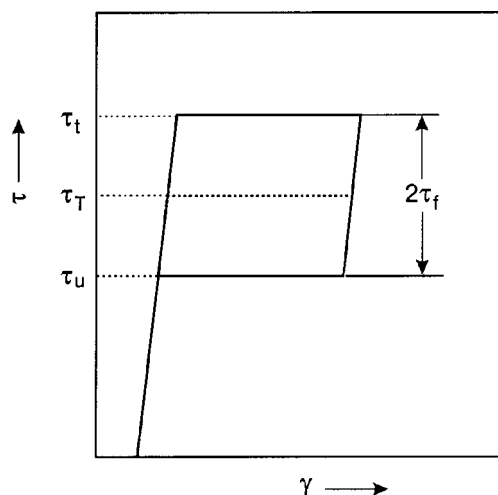

FIG. 1. Diagram of an idealized load versus strain loop for a superelastic crystal.

sample) consists in the rearrangement of the twin structure to the parent structure and occurs when the external load reduces the value $\tau_T - \tau_f$. In order for a hysteresis loop close to the idealized loop to be realized, the atomic structure and distribution of lattice defects in the sample must be extremely uniform. Under real conditions a sample is always to some degree nonuniform, so that there is a distribution of values of the parameters τ_T and τ_f. In addition, hardening processes can arise in the sample during its deformation as new lattice defects are formed. As a result of the deformation the twinning of the sample will come about in a certain interval of stresses. Nevertheless, relations (1) and (2) can be used to find approximate values of the microscopic parameters τ_T and τ_f (Refs. 4 and 5).

According to (2), the reverse motion of the twin boundaries during unloading can occur only under the inequality

$$\tau_T > \tau_f. \tag{3}$$

Apparently, it is condition (3) that is the criterion for the appearance of the superelasticity effect in many alloys. At present there is a known set of twinning alloys having some degree of order or other in the distribution of the different kinds of atoms, but only a few of them exhibit the superelastic deformation effect due to reversible twinning.[7]

It is known that the solubility limit of lead in indium is around 12 at.%. It has been shown previously[2] that the superelasticity effect is not observed in crystals of the alloy In–3.5 at.% Pb, and their plastic deformation is completely irreversible. It is therefore of interest to expand the interval of lead concentrations in the alloy In–Pb within the solubility limits and to analyze in more detail the conditions under which inequality (3) holds and the superelasticity effect is manifested. In this paper we report a comprehensive study of the deformation properties of this alloy for four values of the Pb concentration: 3.5, 6, 8, and 11.6 at.%. For each alloy the values of τ_T and τ_f are obtained, and the influence of temperature and strain rate on them is investigated. It is shown that superelastic deformation in In–Pb crystals is governed by athermal processes. The superelasticity effect vanishes in crystals of the alloy with 3.5 at.% Pb, and for the more concentrated alloys it is suppressed with increasing temperature $T > 180$ K; in both cases this corresponds to the approximate equality of τ_T and τ_f.

It is also of interest to investigate the behavior of the parameters τ_T and τ_f upon the hardening of the alloys as a result of their cyclic loading. It is found that hardening leads to an increase of the average value of the parameter τ_f and to the appearance of dispersion in its distribution in the samples; this is a consequence of growth of the number of lattice defects (dislocations) and enhancement of the nonuniformity of their distribution over the sample.

The results of this study are compared to the data in the literature obtained in studies of elastic twinning and of superelasticity due to the formation of a stress-induced martensite.

2. EXPERIMENTAL TECHNIQUES

The experiments were done on single-crystal samples of In–Pb alloys with lead concentrations of 3.5, 6, 8, and 11.6 at.%. The method used to grow the single crystals and pre-

pare the samples was described in detail in Ref. 8. Samples with dimensions of $5 \times 5 \times 15$ mm were strained by compression along the [001] axis at a shear strain rate in the twinning system in the range $\dot{\gamma} = 10^{-5} - 10^{-2}$ s^{-1} at temperatures in the range 1.7–300 K on a strain testing machine of the MRK-1 design at the B. Verkin Institute for Low Temperature Physics and Engineering, National Academy of Sciences of Ukraine, Kharkov. The strain curves were recorded simultaneously on two chart recorders: on a KSP-4 in load versus loading time coordinates, and on a PDP-4 as load versus displacement of the rod of the strain testing machine.

The inelastic deformation of the crystals occurred exclusively by twinning. All four of the twinning systems $\{101\}$ $\langle 101 \rangle$ were equally loaded, but usually one or two systems were actively operating. Some of the samples were subjected to multiple twinning (up to $n = 100 - 300$ loading–unloading cycles). The cyclic loading was done at $T = 77$ K at a velocity of the rod of the strain testing machine $\dot{h} = 1$ mm/min (h is the height of the sample), which corresponds to an average rate of shear $\dot{\gamma} = 2.2 \times 10^{-3}$ s^{-1}. The sample was deformed in each cycle for a given time $t_0 =$ const, after which the total elastic strain and twinning deformation $\gamma_0 = 2\dot{h}t_0/h$ did not exceed one-half of the maximum strain $(2/3)\gamma_{max}$ (for geometric reasons, one-third of the height h of the sample in the end regions did not participate in the plastic shear).

The friction stress τ_f was calculated as one-half of the quotient obtained by dividing the area of the hysteresis loop by the final strain; this provided an averaging of τ_f over the sample. The thermodynamic stress τ_T was determined as the difference between the stress at the onset of twinning and the friction stress. To obtain the dependence of the parameters τ_T and τ_f on the lead concentration, we chose samples whose hysteresis loops were closest to ideal. Twinning in those samples was brought about through the motion of free twin boundaries not having intersections with twins of other systems or with the ends of the sample in contact with the supporting surfaces of the strain testing machine. The hardening coefficient in the given crystals had extremely low values, indicating that the samples were quite uniform.

3. EXPERIMENTAL RESULTS AND DISCUSSION

3.1. Estimate of the parameters of the mechanical hysteresis and their dependence on the lead concentration and experimental conditions

Shape of the hysteresis loops. Figure 2a shows a nearly ideal hysteresis loop for one of the highly perfect lead samples with 8 at.% Pb at $T = 77$ K, on the basis of which we determined the parameters τ_T and τ_f. For the given sample $\tau_T = 0.62$ MPa and $\tau_f = 0.06$ MPa, so that inequality (3) holds.

The friction stress is a structure-sensitive quantity. It is the greater the lower the perfection of the initial structure of the sample, and it increases with increasing density of deformation defects. It is possible that the friction stress also depends on the temperature and strain rate.[9] Figure 2b shows a hysteresis loop for another alloy sample with the same concentration, but less perfect in respect to its initial defect structure. The value of the stress τ_T did not change, but the friction stress τ_f increased substantially: $\tau_T = 0.62$ MPa and
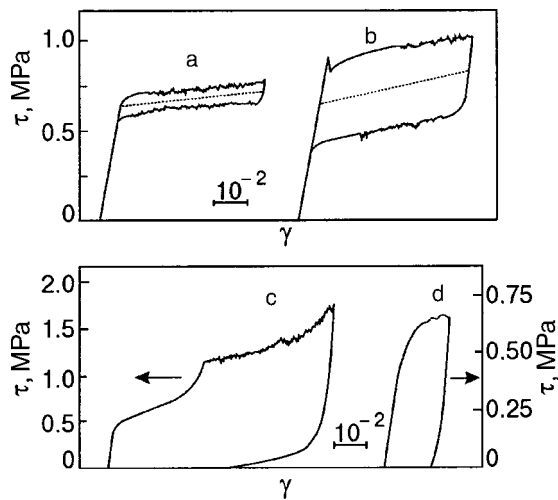
FIG. 2. Strain curves for crystals of In–Pb alloys: a,b—In–8 at.% Pb, $T=77$ K; c,d—In–6 at.% Pb, $T=150$ and 225 K, respectively.

FIG. 3. Temperature dependence of the stresses τ_t, τ_u, τ_T, and τ_f, all normalized by the shear modulus in the twinning system, for crystals of the alloy In–8 at.% Pb.

$\tau_f=0.22$ MPa. Nevertheless, inequality (3) holds for this sample, too, so that the deformation remains completely reversible.

Figure 2c shows an example of a hysteresis loop with a partially reversible deformation for a sample of the alloy In–6 at.% Pb which was subjected to multiple cyclic deformation. In the closed cycle the plastic deformation was of the order of 6%, and the residual deformation was of the order of 4%. As a result of the cyclic deformation the area of the hysteresis loop (i.e., the friction stress) increased strongly, and the shape of the loop was distorted. The large fraction of irreversible deformation indicates the violation of inequality (3). The total recovery of the dimensions of the sample in this case is possible only if the sign of the external load is changed, in which case the external load should have an absolute value equal to the difference of the friction stress and the thermodynamic stress.[1)]

Influence of temperature. Figure 3 shows the temperature dependence of the stress (normalized by the shear modulus) for the onset of twinning and untwinning for the In–8 at.% Pb alloy.[2] The values of τ_t and τ_u were measured on the same sample by multiple loading and unloading at different temperatures. We see that for $T\lesssim180$ K the nucleation of twins and their emergence from the crystal is determined by factors which are insensitive to the testing temperature. Figure 3 also shows the values of τ_T and τ_f calculated with the use of relations (1) and (2). The insensitivity of the stresses τ_t and τ_u to temperature is equivalent to the absence of temperature dependence in the quantities to be calculated, τ_T and τ_f. For the alloys In–11.6 at.% Pb and In–6 at.% Pb[2] the values of the stresses τ_t and τ_u at $T\lesssim180$ K are also independent of the testing temperature.

As we have said, the superelastic behavior of In–Pb alloys is observed only for $T\lesssim180$ K. At higher temperatures $\gtrsim225$ K the twins remain in the crystal even after the load is removed, so that all of the deformation introduced in the crystal is irreversible (see Fig. 2d). The suppression of the superelasticity effect at higher temperatures is due to the activation of diffusion processes, which promote the restoration of the equilibrium local atomic order that has been disrupted by the twinning shear: this results in a sharp decline in the
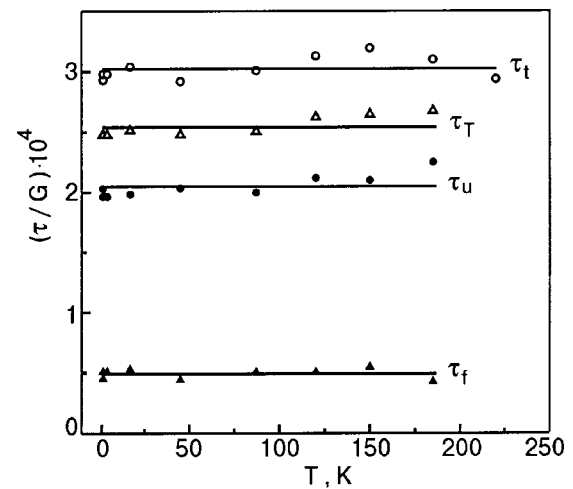
thermodynamic stress τ_T with increasing temperature and increasing hold time of the sample under load.[12]

In terms of the character of the influence of temperature on the thermodynamic stress τ_T, the superelasticity due to pseudotwinning is markedly different from the superelasticity due to the formation of a stress-induced martensite. In the latter case the stress of formation of the martensite and the matrix phase in the martensite and, hence, τ_T depend linearly on temperature and go to zero at the temperatures at which the direct and inverse martensitic transformations begin.[13] The constancy of τ_T in In–Pb alloys for $T\lesssim180$ K indicates that the phenomenon studied here does not belong to the class of ordinary martensitic transformations: the pseudotwinning discussed here is a special form of martensitic transformation, which occurs only under an external load and cannot be caused by a change in temperature.

Influence of the strain rate. The jumplike change in the strain rate in the interval $10^{-5}\,\mathrm{s}^{-1}<\dot\gamma<10^{-2}\,\mathrm{s}^{-1}$ during the deformation of samples of superelastic In–Pb alloys at $T\lesssim180$ K is not noticeably reflected on the τ–γ strain curve: neither the jumps nor the kinks characteristic for deformation by slip are observed on it. The parameters τ_t, τ_u, τ_T, and τ_f of the hysteresis loops likewise are insensitive to the strain rate. This finding agrees with the absence of temperature dependence of these parameters, with the presence of only an instantaneous creep during stepwise loading of the sample, and with the absence of stress relaxation when the strain testing machine is turned off.[2] The absence of rate dependence of the parameter τ_f means that the resistance to twinning deformation at low rates is of the nature of dry friction.

It is only in the region of their superelastic behavior, i.e., for $T\lesssim180$ K, that the strain rate does not have a noticeable influence on the deformation parameters of In–Pb alloys. For temperatures at which diffusion processes are activated, the strain rate can play a critical role in the appearance of the superelasticity effect. For example, by going to shock loading, in which case the sample is found in the loaded state for $\sim30\,\mu$s, it has been possible to observe the superelastic deformation at room temperature.[12] The reason is that even at high temperature there is insufficient time during the brief

loading for the equilibrium atomic order, disrupted by twinning, to be restored in the twin.

Influence of the lead concentration. The parameters of the mechanical hysteresis were found for alloys of three concentrations: 6, 8, and 11.6 at.% Pb; these data are presented in Fig. 4. We see that the thermodynamic stress increases linearly with increasing Pb concentration, while the friction stress decreases. For the alloy with 3.5 at.% Pb the thermodynamic stress was found by extrapolation of the $\tau_T(c)$ curve to the region of low concentrations (Fig. 4), while the friction stress τ_f was determined as the difference between the stress at the onset of twinning and τ_T. It was found that for superelastic In–Pb alloys with 6, 8, and 11.6 at.% Pb inequality (3) is well satisfied, especially for the alloys with 8 and 11.6 at.% Pb. With decreasing lead concentration the ratio between these two stresses decreases on account of a decrease in τ_T and an increase in τ_f. Finally, for the alloy with 3.5 at.% Pb there is approximately equality of τ_T and τ_f, and that leads to suppression of the superelasticity effect.

Nature of the athermality of the low-temperature superelastic deformation in In–Pb alloys. The thermodynamic stress generated by the disruption of the equilibrium atomic order in the presence of a twinning shear in a locally ordered In–Pb alloy is uniquely determined by the degree of this order, which, as is shown by both theory and experiment,[14] depends on the temperature. However, for many alloys the degree of short-range order remains unchanged over a wide range of temperature.[15] In the case of In–Pb alloys the temperature independence of the thermodynamic stress may indicate either that the equilibrium order parameter is independent of temperature or that the diffusion processes are frozen out. Below a certain temperature the diffusional relaxation time of the order parameter can turn out to be longer than the characteristic laboratory time, and a "frozen" order, established at higher temperatures, will be manifested in the low-temperature region.

In the absence of thermodynamic stress τ_T the friction stress τ_f will play the role of the yield stress for the twinned crystal. The friction stress may be represented as the sum of two components: an athermal component due to the long-range internal stresses, and a temperature-dependent component due to the resistance to the motion of the twin boundary by barriers of an atomic scale—Peierls relief, impurities, etc. It is natural to assume that the main contribution to the athermal component of the friction stress in the initial samples comes from the internal stresses created by perfect growth dislocations. This part of the athermal component of the friction stress can be calculated by the formula[16]

$$\tau_{fd} = \alpha G b \rho^{1/2}, \tag{4}$$

where G is the shear modulus, b is the modulus of the Burgers vector, ρ is the density of growth dislocations, and α is a constant of the order of 0.2, the exact value of which depends on the specifics of the distribution of the dislocations. The stress τ_{fd} can increase substantially during cyclic deformation of a sample, as fresh dislocations arising in the cycling process accumulate in it.

The temperature-dependent component of the friction stress is calculated theoretically for the case when the expansion of the twin layer is governed by the motion of twinning dislocations.[17] The influence of temperature turned out to be different depending on the character of the motion of the twinning dislocations: in the case of high-speed (above-barrier) motion of the boundaries the friction stress increases with increasing temperature in accordance with the temperature dependence of the coefficient of viscous drag on dislocations; in the thermally activated motion of twinning dislocations with extremely low velocities the friction stress to a first approximation varies in proportion to the temperature. Strong temperature dependence of the friction force observed in the case of elastic twinning of perfect calcite crystals with a density of perfect dislocations $\rho \sim 10^2$ cm^{-2} is due to the overcoming of the Peierls potential relief by the twinning dislocations.[9] For fcc crystals the values of the Peierls stress are typically low, whereas for In–Pb crystals, which have close to an fcc lattice, this friction component can apparently be neglected.

The twinning process consists primarily in the nucleation of twinning dislocations and their subsequent motion in the twinning plane. The fact that in the case of In–Pb alloys the friction stress at $T \lesssim 180$ K turns out to be insensitive to temperature variations and the strain rate means that under these conditions the main part of τ_f is the long-range component, and the factor governing the twinning process is the athermal nucleation of twinning dislocations. An estimate of the friction stress in In–Pb alloys according to formula (4) for $\alpha = 0.2$ and the typical density of growth dislocations for these alloys, $\rho \sim 10^7$ cm^{-2}, gives a value close to the measured value ($\tau_{fd} \approx 0.06$ MPa). A contribution of perfect growth dislocations to the friction stress has also been observed[9] in calcite crystals with a high density of perfect dislocations, $\rho \sim 10^4$ cm^{-2}.

Analysis of the curves of $\tau_T(c)$ and $\tau_f(c)$ obtained for the In–Pb alloys affords the possibility of refining the microscopic nature of the parameters under study. The thermodynamic stress τ_T is determined by the degree of ordering of the alloy and for this reason depends on the concentration of the doping element. According to Ref. 18, the degree of short-range order increases linearly with increasing c in a certain interval of concentrations. This finds confirmation in our experiments (Fig. 4) if it is assumed that τ_T is to a first approximation proportional to the degree of local order.
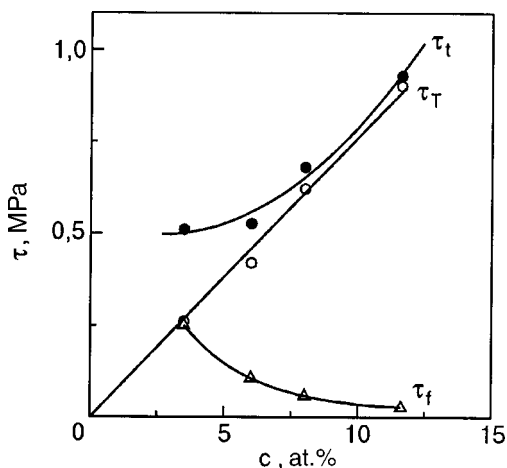

FIG. 4. Concentration dependence of the stresses τ_t, τ_T, and τ_f for In–Pb crystals at a temperature $T = 77$ K.

Moreover, with increasing lead concentration the friction stress τ_f decreases (Fig. 4). This means that impurity defects give an insignificant contribution to the friction stress, but the presence of impurity complexes apparently promotes the nucleation of twinning dislocations.

As to the perfect dislocations, their initial density, and also the density of dislocations arising in the sample during the stage of microdeformation by slip, should decrease with increasing lead concentration together with the increase in the yield stress for deformation by slip. Thus the results obtained argue in favor of the hypothesis of a dislocation nature of the friction force τ_f in the twinning of In–Pb.

3.2. Work hardening in the cyclic deformation of superelastic In–Pb alloys

Figure 5a shows the strain curves observed for a sample of the alloy In–6 at.% Pb in the cyclic deformation by loading and unloading in the regime of a fixed total deformation $\gamma_0 \simeq 1.7\%$. We call attention to the change in the shape of the hysteresis loops as a result of the repeated cycling:

— with increasing number of cycles there is a gradual expansion of the hysteresis loop along the vertical, i.e., an increase of τ_f;

— the stage of easy twinning contracts with each cycle and is shifted to higher stresses, while the work hardening coefficient $\theta = d\tau/d\gamma$ in the stage of easy twinning increases slightly;

— immediately after reaching the yield stress τ_t an intensive development of the work hardening is observed, specifically: before the stage of easy twinning is a transition region where the twinning takes place with a smooth decrease of θ, but here the value of τ_t remains practically independent of the number of cycles;

— the fraction of plastic shear decreases within the limits of the specified deformation;

— the twinning extends all the way to total unloading, and increasing the number of cycles leads to the appearance of a residual deformation.

For crystals of In–8 at.% Pb these changes are small, accumulate slowly, and lead mainly to expansion of the loop: growth of τ_f by approximately 50% after 150 cycles; the loop for the first loading–unloading cycle is shown in Fig. 2a. In the case of the the In–6 at.% Pb crystals we see that even the first loop differs noticeably from the idealized loop (compare Fig. 5a, cycle 1 and Fig. 2): the untwinning in this region of the crystal, which was distorted during twinning in the loading stage, meets with greater resistance.

Let us consider in more detail the transition work hardening. This is the region lying between the initial linear segment corresponding to elastic deformation of the sample and the stage of easy twinning during loading, and also the corresponding part of the loop during unloading. The diagram of the hysteresis loop (Fig. 5b) shows the basic notation used for describing transition hardening: τ_t and τ_u are the stresses at the onset of twinning and untwinning, respectively, γ_t and γ_u are the strains corresponding to these stresses, $0'A$ and $0''B$ are the parts of the loop corresponding to transition work hardening; AC' and BD' are the graphical extrapolations of the transition-hardening segments in the loading and unloading stages [see formulas (13) and (14) below].
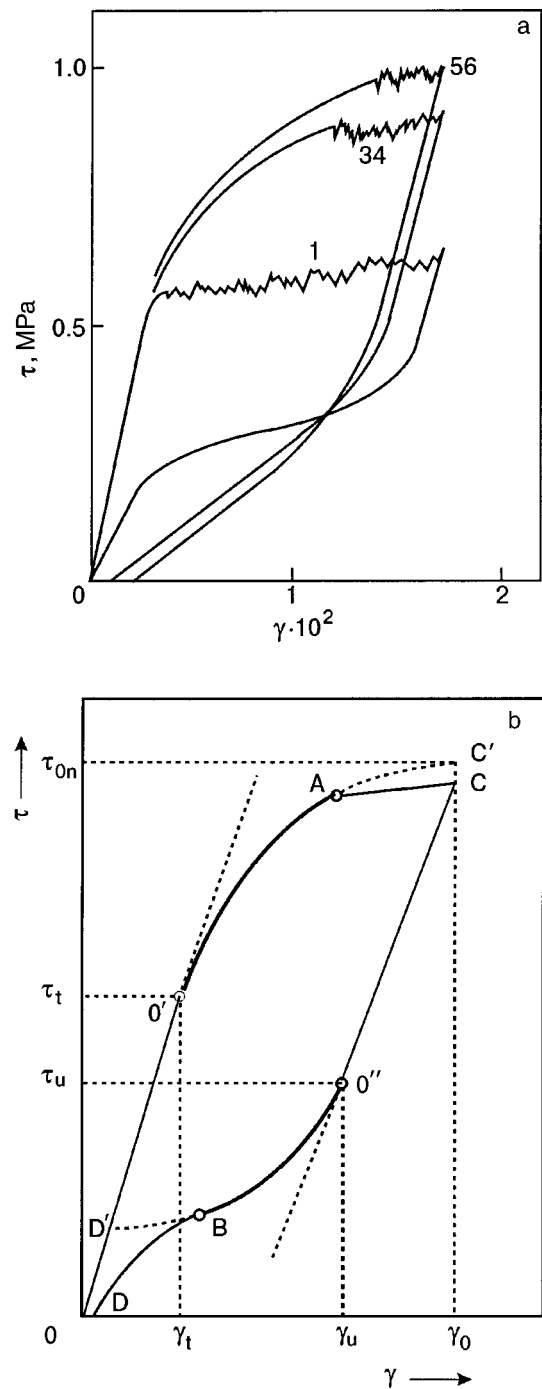

FIG. 5. Strain curves for crystals of the alloy In–6 at.% Pb for loading–unloading cycles at a fixed final deformation $\gamma_0 \simeq 1.7\%$, $T = 77$ K (a); diagram of the strain curve for analysis of the work hardening in the loading (segment $0'A$) and unloading (segment $0''B$) stages; AC is the region of easy twinning; AC and BD' are the graphical extrapolations of the transition-hardening segments (b).

The stresses τ_t and τ_u were determined from the start of the deviation of the strain curve from the linear (elastic) part. It turns out that the values of these stresses are practically independent of the number of the cycle, and only a slight growth of τ_t was observed in the last stages of the cycling: this observation allows us to conclude that the thermodynamic stress τ_T does not change during cycling. The transition hardening is described satisfactorily by a parabolic dependence:

on the loading part

$$\tau - \tau_t = \alpha_t [\gamma - \gamma_e(\tau)]^{1/2}, \tag{5}$$

on the unloading part

$$\tau_u - \tau = \alpha_u \{\gamma_{0p}^{(n)} - [\gamma - \gamma_e(\tau)]\}^{1/2}. \tag{6}$$

Here α_t and α_u are coefficients that depend on the number of the cycle; $\gamma_{0p}^{(n)} = \gamma_0 - \gamma_e(\tau_{0n})$ is the maximum plastic deformation in the nth cycle. For some of the cycles the regions of the hysteresis loops of interest to us have been replotted in the appropriate coordinates (see Fig. 6, where $\tau' = \tau - \tau_t$, $\gamma' = \gamma - \gamma_e(\tau)$, $\tau'' = \tau_u - \tau$, $\gamma'' = \gamma_{0p}^{(n)} - [\gamma - \gamma_e(\tau)]$). In Fig. 6a the deviations from straight lines correspond to the start of easy twinning (point A in Fig. 5b). Figure 7 shows the change in the coefficients α_t and α_u during multiple cycling. We see that the coefficients α_t and α_u in one cycle are close in value and increase with the number of the cycle n according to the law

$$\alpha_t = \alpha_u = \alpha = \beta n^{1/2}, \tag{7}$$

where $\beta = 0.92$ MPa.

The regularities described above in the influence of cyclic deformation on the parameters of the hysteresis loop for the alloy In–6 at.% Pb take place for any In–Pb alloy possessing the properties of superelasticity, but the value of the coefficient β in the empirical formula (7) will vary, together with the parameters τ_T and τ_f, upon changes in the lead concentration.

Let us now discuss these regularities from the standpoint of the existing ideas about the microscopic nature of work hardening of crystalline materials. The term work hardening is generally understood to mean a set of phenomena which lead to the necessity of increasing the deforming stress τ in order to continue deformation at a specified rate $\dot{\gamma} = \text{const}$. An outward sign of hardening is a positive value of the derivative $\theta(\tau) = d\tau(\gamma)/d\gamma > 0$ on the strain diagram. On the microscopic level work hardening is brought about by effects of two types: 1) the accumulation of the defects in the crystal during deformation, which resist slip or twinning; 2) the existence, in the volume of the crystal, of a spectrum of start stresses for the nucleation and propagation of slip or twinning (perfect or twinning dislocations), which leads to a nonuniform distribution of inelastic deformation in the volume of the crystal and to the inclusion of new regions in the deformation process as the deforming stress increases.

To describe effects of the first type one usually uses the Taylor model[19] (growth of the density of individual dislocations) or the Mott model[20] (growth of the density of dislocation pileups). Effects of the second type are realized, e.g., in the stage of microplasticity of single crystals and elastically isotropic polycrystals, and also in the process of macroscopic (to several percent) plastic deformation of polycrystalline materials in the presence of a substantial misorientation of highly anisotropic crystallites (parabolic hardening).[21]

In examining the work hardening of crystals from the standpoint of the ideas set forth above, one should note the existence of certain differences between the slip and twinning deformations. The stopping of slip in local regions of the crystal may be accompanied, as the deforming stress is
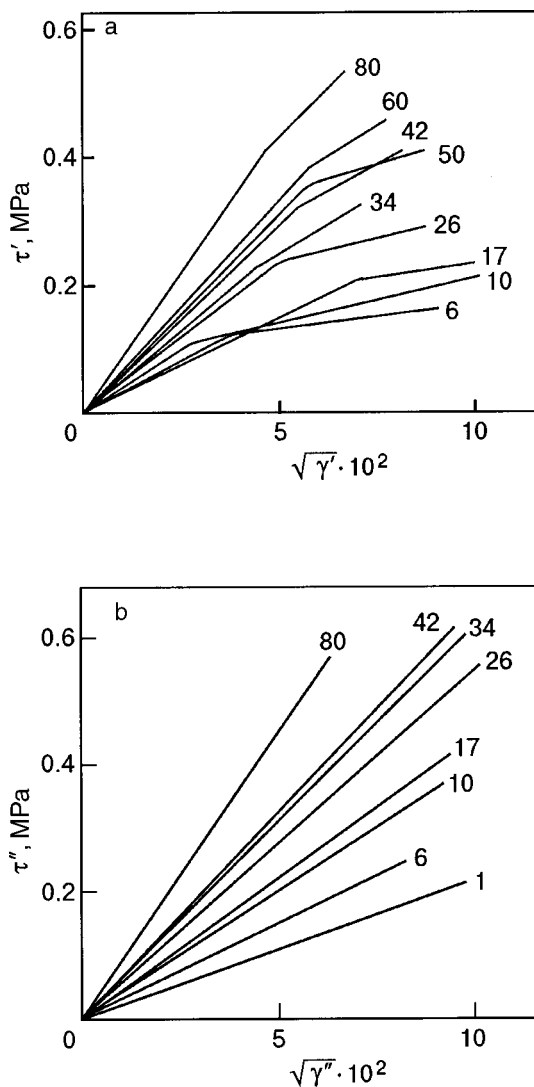

FIG. 6. Parts of the strain curves for different loading–unloading cycles, plotted, in accordance with Eqs. (5) and (6), in the coordinates $\tau' - \sqrt{\gamma'}$ (a) and $\tau'' - \sqrt{\gamma''}$ (b).
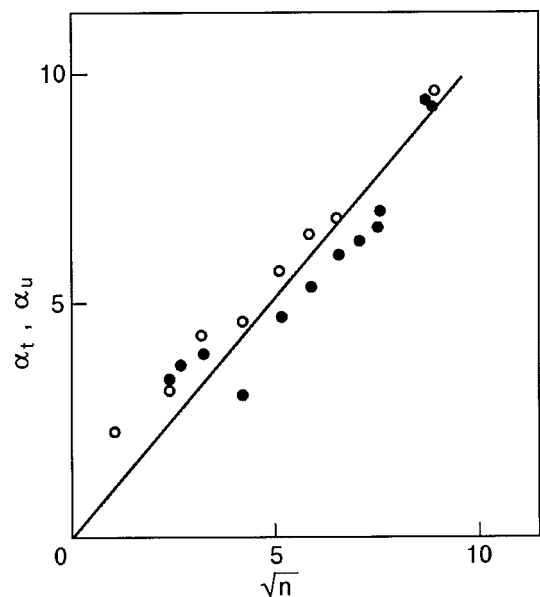
FIG. 7. Dependence of the coefficients α_t ($\bullet$) and α_u ($\circ$) in Eqs. (5) and (6) on the number of the cycle [see Eq. (7)].

increased, not only by the propagation of the slip to other regions but also by its resumption in the hardened regions. In the case of twinning the transition of the deformation process into new regions is a consequence of a specific crystallographic property of the given form of deformation, viz., the fact that it occurs only one time in each crystallographic twinning plane.

In the description of the work hardening due to effects of the second type, one of the main problems is that of modeling or empirically recovering the distribution function for the friction stress resisting the nucleation and propagation of inelastic deformation in a crystalline sample, e.g., the distribution function of sources of dislocations over start stresses.[22] In the case considered here, that of twinning deformations, an important question is whether it is possible to recover this function for a repeatedly deformed crystal from the shape of the hysteresis loop. The initial condition for this is the assumption that twinning takes place during loading by means of the formation and development of a set of twins as a result of the successive selection of regions of the sample corresponding to the nucleation condition.

According to experimental observations, even in the advanced stages of the cyclic deformation, twinning begins at a fixed value of the deforming stress, $\tau \approx \tau_t$. Furthermore, the absence of dependence of the parameters of the strain diagram on the strain rate $\dot{\gamma}$ indicates that the resistance to twinning is of the nature of dry friction. In that case the law of deformation in differential form can be written in the form of the relation

$$d[\gamma - \gamma_e(\tau)] = (\gamma_0 - \gamma_t)\delta(\tau - \tau_T \mp \tau_f)d\tau,$$
$$\gamma_0 - \gamma_t \leqslant s. \tag{8}$$

Here $\gamma_e(\tau)$ is the elastic strain, $\delta(\tau)$ is the Dirac delta function, $\gamma_t = \gamma_e(\tau_t)$, τ_f is the initial absolute value of the dry friction stress, which is the same for all regions of the sample, and the change of its direction when loading is replaced by unloading is taken into account by the "$\mp$" sign ("$-$" for loading and "$+$" for unloading). The integration of (8) leads to the following deformation law for the sample:

$$\gamma(\tau) = \gamma_e(\tau) + (\gamma_0 - \gamma_t)\chi(\tau - \tau_T \mp \tau_f), \quad \gamma_0 - \gamma_t \leqslant s. \tag{9}$$

In this expression the twinning deformation is described by a Heaviside step function: $\chi(\tau) = 0$ for $\tau < 0$, and $\chi(\tau) = 1$ for $\tau > 0$.

Since the parameter τ_T does not change upon cycling, it is natural to assume that the hardening that occurs with increasing number of cycles n is due to the appearance of a deformation-related admixture to the friction stress, $\tilde{\tau}_f$, which is nonuniform over the volume of the sample: $\tau_f = \tau_{f0} + \tilde{\tau}_f$, where τ_{f0} is the value of the friction stress of the initial (undeformed) sample. In such a case the deformation law (9) will be realized only in small locally uniform regions of the sample. For estimating the influence of the disperse admixture $\tilde{\tau}_f$ to the deformation law for the sample as a whole during cycle number n one should introduce a normalized distribution function $f_n(\tilde{\tau}_f)$, having determined the quantity $f_n(\tilde{\tau}_f)d\tilde{\tau}_f$ as the fractional part of the sample in which the admixture to the friction stress by the start of the nth cycle takes a value in the interval $(\tilde{\tau}_f, \tilde{\tau}_f + d\tilde{\tau}_f)$. For the sample in the nth cycle the deformation law averaged with the distribution function $f_n(\tilde{\tau}_f)$ takes the form

$$\gamma^{(n)}(\tau) = \gamma_e(\tau) + [\gamma_0 - \gamma_e(\tau_{0n})]\int_0^\infty \chi(\tau - \tau_T \mp \tau_{0f} \mp \tau')$$
$$\times f_n(\tau')d\tau', \quad [\gamma_0 - \gamma_e(\tau_{0n})] \leqslant s. \tag{10}$$

Relation (10) formally admits the possibility of any absolute values of $\tilde{\tau}_f$ under the normalization condition

$$\int_0^\infty f_n(\tau)d\tau = 1. \tag{11}$$

To achieve agreement of the deformation law (10) with the empirical formulas (5)–(7) and to get a qualitatively correct reflection of the main features of the hysteresis loops during cyclic deformation of superelastic In–Pb alloys (Fig. 5), it is sufficient to use a distribution function $f_n(\tilde{\tau}_f)$ described by the formulas

$$f_n(\tau) = \frac{2\tau}{\tau_n^2}\chi(\tau)\chi(\tau_n - \tau),$$
$$\tau_n = \tau_{0n} - \tau_t = \beta\sqrt{(n-1)[\gamma_0 - \gamma_e(\tau_{0n})]}. \tag{12}$$

It is easy to see that this function satisfies the normalization condition (11) and that for $n = 1$ it goes over to a delta function: $f_1(\tau) = \delta(\tau)$.

We note immediately that the function (12) does not take into account the presence of the segments of easy twinning AC on the hysteresis loops at small values of n (Fig. 5). However, this function correctly describes the hysteresis $\gamma^{(1)}(\tau) = \gamma(\tau)$ in the first cycle $n = 1$, since $\tau_{01} = \tau_t$ and $f_1(\tau) = \delta(\tau)$; consequently, substitution of this function into (10) will lead to the deformation law of a uniform sample (9). It is also important that the distribution function (12) correctly describes the asymptotic form of the hysteresis loops at large values of n, when the segments of easy twinning vanish. Indeed, the substitution of (12) into (10) leads to the equations:

in the loading process

$$\gamma^{(n)}(\tau) = \gamma_e(\tau) + \frac{\chi(\tau - \tau_t)}{(n-1)\beta^2}(\tau - \tau_t)^2; \tag{13}$$

in the unloading process

$$\gamma^{(n)}(\tau) = \gamma_e(\tau) + [\gamma_0 - \gamma_e(\tau_{0n})] - \frac{\chi(\tau_u - \tau)}{(n-1)\beta^2}(\tau_u - \tau)^2. \tag{14}$$

We recall that the parameters of these equations, τ_t and τ_u, are determined by the initial structure of the sample:

$$\tau_t = \tau_T + \tau_{f0}, \quad \tau_u = \tau_T - \tau_{f0}.$$

The last terms on the right-hand sides of equations (13) and (14) describe the twinning and untwinning processes and correspond to the empirical equations (5) and (6), and the coefficient α as a function of the cycle number n takes the form (7). We should mention once again that, of course, the formulas obtained do not describe the stage of easy twinning observed in each deformation cycle but pertain only to the stage of smooth hardening after the onset of twinning and untwinning.

It is important to note that the unloading equation (14) also describes the appearance of a residual deformation at sufficiently large values of the cycle number $n > n_c$, and it also permits finding a relation between the parameters of the alloy and the value of the residual deformation $\gamma^{(n)}(0)$ after the nth cycle and the critical cycle number n_c for the appearance of residual deformation:

$$\gamma^{(n)}(0) = [\gamma_0 - \gamma_e(\gamma_{0n})] - \frac{(\tau_T - \tau_{f0})^2}{(n-1)\beta^2}, \quad n > n_c; \quad (15)$$

$$n_c = \frac{(\tau_T - \tau_{f0})^2}{[\gamma_0 - \gamma_e(\tau_{0n})]\beta^2} + 1. \quad (16)$$

These formulas reflect all the basic regularities of the appearance and development of the residual deformation during cycling of a superelastic alloy; in particular, they describe the complete suppression of the superelasticity effect at large n ($n \to \infty$) and upon the growth of the uniform friction ($\tau_{f0} \to \tau_T$).

4. CONCLUSIONS

1. We have investigated, in the temperature interval 1.7–180 K, the reversible plastic deformation by twinning in single crystals of the alloys In–Pb with different lead concentrations: 3.5, 6, 8, and 11.6 at.% Pb.

2. We have obtained and analyzed the shape of the hysteresis loops corresponding to a loading–unloading cycle and have determined the parameters describing the mechanical hysteresis: the stress τ_t and τ_u for the onset of twinning and untwinning, respectively, the thermodynamic stress τ_T, and the friction stress τ_f. The reversible deformation is governed by athermal processes: the mechanical characteristics τ_T and τ_f in the region of superelasticity are independent of temperature and strain rate.

3. We have shown that the thermodynamic stress responsible for the reversibility of the plastic deformation increases linearly with increasing lead concentration.

4. The friction stress resisting the motion of twin boundaries is mainly due to the dislocation structure of the crystal rather than its impurity structure. Increasing the lead content in the alloy indirectly leads to a lowering of the friction stress through an increase in the yield stress for deformation by slip and, accordingly, to a decrease in the density of growth dislocations.

5. We have shown that the transition from reversible to irreversible twinning as the lead concentration is lowered is due to the fact that the thermodynamic stress and friction stress become equal in magnitude.

6. We have compared our results on the mechanical hysteresis in superelastic In–Pb alloys with published data on the hysteresis in the case of elastic twinning and martensitic transformations. We have analyzed the mechanisms of superelastic deformation in these alloys on that basis.

7. We have proposed an analytical description of the work hardening during cyclic deformation of superelastic In–Pb alloys.

The authors express their gratitude to V. S. Boĭko for numerous helpful discussions of the questions addressed in this paper, and to I. S. Braude for the opportunity to become acquainted with the preliminary x-ray diffraction studies of ordering in In–Pb alloys.

[1] It is interesting to compare the effect described here—the irreversible twinning deformation of In–Pb alloys—with an effect observed[10] at sufficiently low temperatures in calcite—the irreversible change in length of an elastic (wedge-shaped) twin. For $T < 200$ K for shortening of a wedge-shaped thin twin in calcite it is also necessary to apply a stress of the opposite sign to the sample, as a consequence of the strong increase in the friction stress as a result of cooling. We note only that the restoring force in the case of elastic twinning is of a different nature than that for pseudotwinning; specifically, it is due to the surface energy of the twin boundary.[11]

[1] S. V. Lubenets, V. I. Startsev, and L. S. Fomenko, Kristall und Technik **15**, K78 (1980).

[2] S. V. Lubenets, V. I. Startsev, and L. S. Fomenko, Fiz. Met. Metalloved. **52**, 870 (1981).

[3] J. W. Cahn, Acta Metall. **25**, 1021 (1977).

[4] G. F. Bolling and R. H. Richman, Acta Metall. **13**, 709 (1965).

[5] S. V. Lubenets, L. S. Fomenko, and V. I. Startsev, Fiz. Met. Metalloved. **64**, 975 (1987).

[6] B. Wack and A. Tourabi, Arch. Mech. **44**, 621 (1992).

[7] S. V. Lubenets, V. I. Startsev, and L. S. Fomenko, Phys. Status Solidi A **92**, 11 (1985).

[8] S. V. Lubenets, V. I. Startsev, and L. S. Fomenko, Fiz. Met. Metalloved. **39**, 410 (1975).

[9] V. S. Boĭko, R. I. Garber, and A. M. Kosevich, *Reversible Plasticity of Crystals* [in Russian], Nauka, Moscow (1991).

[10] V. S. Boĭko, R. I. Garber, and V. F. Kivshik, Fiz. Tverd. Tela (Leningrad) **12**, 3198 (1970) [Sov. Phys. Solid State **12**, 2584 (1970)].

[11] A. M. Kosevich and V. S. Boĭko, Usp. Fiz. Nauk **104**, 201 (1971).

[12] L. S. Fomenko, S. V. Lubenets, and V. I. Startsev, Scr. Metall. **18**, 535 (1984).

[13] T. A. Schroeder and C. M. Wayman, Acta Metall. **27**, 405 (1979).

[14] M. A. Krivoglaz and A. A. Smirnov, *Theory of Ordered Alloys* [in Russian], Fizmatgiz, Moscow (1958).

[15] V. I. Iveronova and A. A. Katsnel'son, Blizhniĭ poryadok v tverdykh rastvorakh, Nauka, Moscow (1977).

[16] A. Sceger, in *Dislocations and Mechanical Properties of Crystals*, an International Conference held at Lake Placid, New York, September 6–8, 1956; publ. Wiley, New York (1956), pp. 243–329; [Russian trans.], edited by M. V. Klassen-Neklyudova and V. L. Indenbom, Inostrannaya literatura, Moscow (1960), p. 179.

[17] V. S. Boĭko, Fiz. Tverd. Tela (Leningrad) **22**, 1066 (1980) [Sov. Phys. Solid State **22**, 621 (1980)].

[18] W. Pfeiler, Acta Metall. **36**, 2417 (1988).

[19] G. F. Taylor, Proc. R. Soc. London, Ser. A , 145 (1934).

[20] N. F. S. Mott, Philos. Mag. , 43 (1952).

[21] J. Friedel, *Dislocations*, Pergamon Press, Oxford (1964), Mir, Moscow (1967).

[22] V. Z. Bengus, T. P. Kovalenko, and V. A. Kuklev, Dokl. Akad. Nauk **247**, 1372 (1979) [Sov. Phys. Dokl. **24**, 672 (1979)].

Translated by Steve Torstveit

SUPERCONDUCTIVITY, INCLUDING HIGH-TEMPERATURE SUPERCONDUCTIVITY

Calculation of the electromagnetic field radiated by an elastic wave in a type-II superconductor

V. D. Fil*

*B. Verkin Institute for Low Temperature Physics and Engineering, National Academy of Sciences
of Ukraine, pr. Lenina 47, 61103 Kharkov, Ukraine*

Formulas describing the conversion of an elastic wave into an electromagnetic field at the
boundary between a type-II superconductor and the vacuum are obtained which admit passing to
both the limiting cases of the normal and Meissner states. A strategy that would permit
experimental measurement of the dynamical parameters of the vortex lattice is discussed. It is
pointed out that the study of the inertial (Stewart–Tolman) component of the radiated
field is a promising area of research. © *2001 American Institute of Physics.*
[DOI: 10.1063/1.1430841]

The first experiments on the interconversion of elastic
and electromagnetic oscillations (the Hall component) in
type-II superconductors were done in the mid-1970s.[1] The
interpretation of these experiments was based on the intro-
duction of an effective penetration depth for the electromag-
netic field in the mixed state. While undoubtedly correct,
such an approach cannot reveal the physical processes ac-
companying the motion of the vortex lattice under the influ-
ence of a sound wave. With the era of high-T_c superconduc-
tivity came conversion experiments on new superconducting
objects.[2] A theory of the effect, which, although simplified (it
does not describe the transition to the normal state), is for-
mulated in terms of the dynamics of the vortex lattice, was
proposed in Ref. 3. However, the experiments[2] corresponded
to the strong-pinning limit, which, as the theoretical analysis[3]
confirms, is relatively uninformative physically. Therefore, at
first glance one may be left with the impression that studying
the electromagnetic fields accompanying an elastic wave in
type-II superconductors in the mixed state would hardly ex-
tend the vast region of study of the dynamics of vortex lat-
tices. This is actually not the case, and the aim of this paper
is to discuss situations in which conversion measurements
contain rather valuable information. In particular, analysis
shows that in the case of weak or moderate pinning one can
directly recover the characteristics of both the pinning itself
and the dissipative processes accompanying the motion of
the vortex lattice. A necessary condition for this is that one
must measure the phase as well as the modulus of the con-
version coefficient. In addition, it is pointed out that, in ad-
dition to the Hall component, the inertial (Stewart–Tolman)
electromagnetic field can also be of considerable interest.

This paper is devoted to a discussion of the electromag-
netic fields radiated by an elastic wave (EMFREWs). The
given experimental scheme ensures that there are no nonlin-
ear effects present, although the study of such effects would
clearly be of independent interest. In addition, for greater
physical clarity we consider only the case of a transverse

sound wave propagating parallel to the external magnetic
field. Generalization of the relations obtained to cases of
other geometries does not present any difficulty.

As a starting point for our analysis of the EMFREWs in
a type-II superconductor, let us discuss the corresponding
effect in a normal metal. This topic, in its day, was discussed
quite intensively in the literature (see the review and the
references cited in Ref. 4), and we revisit it here for the
following reasons:

1. In the previous papers the inertial component has al-
ways been ignored, since it its rather small. It follows from
our present analysis that it is preferable to study it in com-
paratively low magnetic fields, $H_{c1} < H < 0.1 H_{c2}$.

2. As a rule, the previous discussions have dealt mainly
with the mechanism of the electromagnetic generation of
sound, rather than the inverse effect considered here. Finally,
by virtue of the existence of the reciprocity theorem and the
absence of any nonlinear phenomena in the normal phase,
the final answers should be connected by simple relations,
although the methodological approaches to the solution of
these problems are somewhat different (in particular, this
concerns the boundary conditions imposed on the electro-
magnetic field).

3. Previously attention was devoted mainly to analysis of
effects in the nonlocal limit, while the local regime was con-
sidered to be relatively simple and uninteresting. Practically
all type-II superconductors are ''dirty'' systems which, in the
normal state, lie in the local region at all reasonable measure-
ment frequencies. Nevertheless, the analysis of EMFREWs
in this case raises a number of questions that have not been
answered in the literature, and it is therefore advisable to
discuss them briefly.

1. NORMAL STATE

For specificity we consider a normal metal lying in the
lower half space, with the metal–vacuum interface coincid-
ing with the plane $z = 0$. The thickness of the sample is much

greater than the characteristic lengths of the problem (the electron mean free path l, the sound wavelength λ, and the skin depth δ). The external magnetic field **H** is parallel to the z axis and to the sound wave vector **q**. The displacements **u** in the elastic wave are parallel to the x axis. The transverse dimensions of the sound beam are assumed to be much greater than λ, so that the problem can be reduced to one-dimensional.

The boundary conditions imposed on the electromagnetic field are obtained as follows. The continuity of the tangential components of the electromagnetic field at the metal–vacuum boundary and the uniformity of these fields in the directions transverse to the wave beam in the metal, including the region near the interface, allow us to consider them to be uniform on the other side of the boundary as well, even though the electromagnetic wavelength in vacuum can be many orders of magnitude greater than all the characteristic lengths of the problem. Therefore, near the interface in free space, Maxwell's equations reduce to a one-dimensional wave equation whose unique solution is a plane wave with electric and magnetic components related by

$$E_x = -H_y; \quad E_y = H_x. \tag{1}$$

Combining (1) with the second of Maxwell's equations, we obtain the boundary condition for the EMFREW regime:

$$\frac{d\mathbf{E}}{dz}(0) = -ik_c \mathbf{E}(0); \quad k_c = \omega/c. \tag{2}$$

Of course, Eq. (2) is valid only for the EMFREW regime, while in the regime of electromagnetic sound generation, in addition to the incident electromagnetic wave one must also take into account the reflected wave or, equivalently, employ the concept of surface impedance.

Analysis of the EMFREW problem is based on the solution of a system of two equations: the equation for the electric field, obtained from a combination of Maxwell's equations,

$$\text{curl curl } \mathbf{E} = -\frac{4\pi}{c^2}\frac{dj}{dt} \tag{3}$$

and the kinetic equation for the the nonequilibrium correction ψ to the electron distribution function in the metal in the presence of elastic and magnetic fields,[5]

$$\frac{\partial\psi}{\partial t} + v_z\frac{\partial\psi}{\partial z} + \frac{\partial\psi}{\partial t_1} + \frac{\psi}{\tau}$$
$$= -e\mathbf{v}\left(\mathbf{E} - \frac{m}{e}\ddot{\mathbf{u}} + \frac{1}{c}[\dot{\mathbf{u}}\mathbf{H}]\right) - \Lambda_{ik}\dot{u}_{ik}. \tag{4}$$

The time dependence of all the quantities appearing in Eqs. (3), (4) is written in the form $\propto e^{i\omega t}$. Sources of perturbation of the distribution function on the right-hand side of (4) are: the Maxwellian field **E** (i.e., the field obeying the Maxwell equation (3), which alone can be detected by an electromagnetic antenna); the extraneous fields are the inertial field (the acoustical analog of the Stewart–Tolman effect) $\mathbf{u}_{ST} = -\ddot{\mathbf{u}}m/e = \mathbf{u}\omega^2 m/e$, the induction field $\mathbf{u}_{ind} = (i\omega/c)[\mathbf{u}\times\mathbf{H}]$, and the deformation field $u_{def} = -\Lambda_{ik}\dot{u}_{ik}$ (here $\Lambda_{ik} \equiv \lambda_{ik} - \langle\lambda_{ik}\rangle$ is the deformation potential; the angle brackets denote the average value over the Fermi surface:

$$\langle a\rangle = \frac{2}{(2\pi\hbar)^3}\int\frac{a}{v_F}dS;$$

where v_F is the Fermi velocity). The coordinate t_1 appearing in Eq. (4) is the time of motion along a cyclotron orbit. The total current **j** in (3) is the sum of the ion current ($\mathbf{j}_{ion} = -i\omega ne\mathbf{u}$) and the electron current and is expressed in the standard way in terms of the distribution function:[5]

$$\mathbf{j} = -e\langle\mathbf{v}\psi\rangle. \tag{5}$$

The amplitude and phase of the sound wave incident on the interface are assumed fixed, i.e., independent of **H**. If necessary the experimental data can be corrected by measuring the field dependence of the sound velocity and damping. The coordinate dependence of the amplitude of the incident wave can be written in the form $u_{inc}(z) = u_0 e^{-iqz}$. However, since a wave of the same amplitude is reflected from the surface, $u_{ref}(z) = u_0 e^{iqz}$, we finally get for the elastic field

$$u(z) = u_0\cos qz \tag{6}$$

and the boundary condition on the elastic displacements at the free surface,

$$u'(0) = 0, \tag{7}$$

is satisfied automatically.

In the local limit $l \ll \lambda$, δ and under the condition $\Omega\tau \ll 1$ ($\Omega = eH/mc$ is the cyclotron frequency) it is customary to assume that all the derivatives on the left-hand side of (4) can be neglected. In the free-electron approximation for the geometry under consideration one has $\Lambda_{xz} = -mv_xv_z$, and therefore the deformation contribution to the current in this case vanishes upon the averaging in (5). Under the same assumptions, this contribution also vanishes for the real Fermi surface in the propagation of sound in symmetric directions because of the odd parity of Λ_{xz} with respect to inversion of the sign of the electron momentum. As a result of Eq. (4), formula (5) reduces to Ohm's law,

$$\mathbf{j} = \sigma_0(\mathbf{E} + \mathbf{u}_{ST} + \mathbf{u}_{ind}), \tag{8}$$

where $\sigma_0 = ne^2\tau/m$ is the conductivity in the local limit. Substituting (8) into (3), we obtain

$$\frac{d^2\mathbf{E}}{dz^2} = k_0^2(\mathbf{E} + \mathbf{u}_{ST} + \mathbf{u}_{ind}); \quad k_0^2 = \frac{4\pi i\omega\sigma_0}{c^2} \equiv \frac{2i}{\delta^2}. \tag{9}$$

The solution of equation (9) is a combination of the skin solution $\mathbf{E}_k(z) = \mathbf{E}_k(0)e^{k_0 z}$ (of the two possible values of k_0 the solution chosen is that which vanishes for $z \to -\infty$) and the forced solution ($\mathbf{E}_B(z) = \mathbf{E}_B\cos qz$,) the ratio of these solutions being determined by the boundary conditions imposed on the Maxwellian field (2):

$$-ik_c\mathbf{E}_k - k_0\mathbf{E}_k = ik_c\mathbf{E}_B + \mathbf{E}_B'(0). \tag{10}$$

For a free surface the derivative on the right-hand side of (10) vanishes. Neglecting k_c in comparison with k_0 on the left-hand side of (10), we obtain

$$\mathbf{E}_k = -\frac{ik_c}{k_0}\mathbf{E}_B \ll \mathbf{E}_B,$$

$$\mathbf{E}(0) = \mathbf{E}_B(0) = -\frac{k_0^2}{q^2 + k_0^2}(\mathbf{u}_{ST} + \mathbf{u}_{ind}). \tag{11}$$

Thus the amplitude of the electric field at the interface is essentially that of the forced solution. At the same time, the amplitude of the magnetic component, $|k_0\mathbf{E}_k/ik_c|$ $=|\mathbf{E}_B(0)|$, is completely determined by the skin field. The result (11) (with the $\mathbf{u}_{ST}$ contribution subtracted) comes into play in all problems of interconversion of elastic and electromagnetic fields. However, it was obtained with the use of certain assumptions whose validity is open to question in several regards:

a) For any character of the reflection of electrons from the interface the derivative with respect to coordinate in (4) near the surface is comparable to the departure term, so that the validity of neglecting it is in doubt.

b) Strictly speaking, the interface is not completely free because of the collisions of the electrons with it, i.e., boundary condition (7) is not quite exact, and $\mathbf{E}'_B(0) \neq 0$.

Because the characteristic scales of the wave numbers of the field in the metal ($\sim q$) and k_c are not comparable in order of magnitude, the derivative on the right-hand side of (10), even though small, will give a perceptible contribution. For this same reason the lifting of the symmetry forbiddenness on the deformation contribution to the current when the weak nonlocality is taken into account can also have a noticeable effect.

Below we attempt to discuss the influence of these factors, since, as we said in the Introduction, we have been unable to find direct answers in the literature.

Let us first discuss the question of the degree to which a diffusely scattering boundary can be considered free. The exact boundary condition on the elastic stresses has the form[6]

$$\rho s^2 u'(0) + \langle \Lambda_{ik}\psi(0)\rangle = 0 \tag{12}$$

(ρ is the density of the metal, and s is the speed of sound).

A correct calculation of the average over the Fermi surface in (12) can be done if a model is specified for the surface scattering potential.[7] However, it is clear physically that if the characteristic size of the inhomogeneities (e.g., roughness) of the boundary is comparable to the mean free path, then the distribution function will be practically even with respect to v_z, and there will be no deformation contribution to (12), i.e., $u'(0) = 0$. In the opposite limiting case, assuming the reflection to be purely diffuse, the averaging in (12) should be done only for $v_z > 0$, since $\psi(0) = 0$ for $v_z < 0$. For making estimates in this case one can limit consideration to the leading approximation, setting $\psi(0) = -e\tau\mathbf{v}\cdot(\mathbf{E}+\mathbf{u}_{ST})$ and taking expression (11) for $\mathbf{E}(0)$. As a result, we obtain

$$\frac{u'(0)}{u(0)} = \frac{\omega}{v_F}\frac{s}{v_F}(\omega\tau). \tag{13}$$

Writing $E'_B(0) = E_B(0)[u'(0)/u(0)]$ in (10), we see from (13) that in the local limit the contribution under discussion is negligible, and one can always use the boundary condition $u'(0) = 0$.

We now continue our analysis by using the free-electron model to calculate the corrections to the quantities of interest in the small nonlocality parameters $(ql, k_0 l)$, assuming that the reflection of electrons from the interface is purely diffuse.

By the method of characteristics we reduce (4) to an ordinary differential equation,

$$v_z \frac{d\psi}{dz} + \frac{\psi}{\tau} = -e\mathbf{v}\cdot(\mathbf{E}+\mathbf{u}_{ST}+\mathbf{u}_{\text{ind}}) - i\omega m v_x v_z \frac{du}{dz}, \tag{14}$$

in which the Fermi velocity components orthogonal to $\mathbf{q}$ are dependent on z:

$$v_x = v_\perp \cos\left(\Omega \frac{z}{v_z} - \varphi\right),$$

$$v_y = -v_\perp \sin\left(\Omega \frac{z}{v_z} - \varphi\right), \quad v_\perp = v_F \sin\theta,$$

$$v_z = v_F \cos\theta. \tag{15}$$

Here θ and φ are the polar and azimuthal angles, respectively.

We write the solution of equation (14) in standard form:

$$\psi(z) = C\exp(-z/v_z\tau) + \psi_1(z), \tag{16}$$

where $\psi_1(z)$ is the particular solution of equation (14).

For $v_z > 0$ the requirement that $\psi(z)$ be finite at $z \to -\infty$ gives $C_{v_z>0} = 0$; for $v_z < 0$ we obtain $C_{v_z<0} = -\psi_1(0)$ for a diffuse boundary.

The presence of a rapidly decaying exponential in (16) presupposes that the electric field in the metal also has a rapidly decaying component E_f. Therefore the solution of the system of equations (3), (14) must be self-consistent. Nevertheless, it can be supposed that the contribution of E_f to the formation of $\psi_1(z)$ is small. Qualitatively this assumption can be justified as follows. Relation (11) is an expression of the result of an interference of fields radiated from the penetration depth δ. Under conditions of the normal skin effect ($l \ll \delta$) it is natural to expect that the contribution of E_f to the total field and, hence, to $\psi_1(z)$ will be insignificant.

Proceeding from this assumption, we seek the solution of system (3), (14) by making the substitution

$$\mathbf{E}(z) = \mathbf{E}_k e^{kz} + \mathbf{E}_q \cos qz. \tag{17}$$

As to $\psi_1(z)$, it must also be expanded in the functions (15).

In Eq. (17) k is the skin wave number, which is given by the dispersion relation

$$k_{1,2}^2 = \frac{k_0^2}{1+(\Omega\tau)^2}(1 \pm i\Omega\tau). \tag{18}$$

At this stage we will not make any assumptions as to the value of the parameter $\Omega\tau$, since even in the local limit in fields $H \to H_{c2}$ it can be large. Calculations lead to the expected result: the current in the zeroth approximation in (ql) must be determined by using the conductivity tensor $\hat{\sigma}$, which is well known from the theory of galvanomagnetic phenomena:

$$\mathbf{j} = \hat{\sigma}(\mathbf{E}+\mathbf{u}_{ST}+\mathbf{u}_{\text{ind}}),$$

$$\sigma_{\alpha\beta} = \frac{\sigma_0}{1+(\Omega\tau)^2}a_{\alpha\beta} \equiv \frac{\sigma_0}{1+(\Omega\tau)^2}\begin{pmatrix} 1 & \Omega\tau \\ -\Omega\tau & 1 \end{pmatrix}. \tag{19}$$

The deformation correction to the current has the form

$$\begin{Bmatrix} j_{\Lambda x} \\ j_{\Lambda y} \end{Bmatrix} = \frac{i}{S}\frac{\sigma_0 u_{ST}}{1+(\Omega\tau)^2}\frac{v_F}{s}ql\begin{Bmatrix} (\Omega\tau)^2-1 \\ 2\Omega\tau \end{Bmatrix}. \tag{20}$$

We estimate the diffuse-scattering contribution as follows. Assuming that $\mathbf{E}_k$ and $\mathbf{E}_q$ are known, we calculate $\psi_1(0)$ and then determine the contribution to the current, performing an averaging over half of the Fermi surface ($v_z < 0$) with the weight factor $\exp(-z/v_z\tau)$. This gives rise to a term of the type $\langle v_\perp^2 v_z^n e^{-z/(v_z\tau)}\rangle$ ($n=0,1,2$) on the right-hand side of (3). We seek the field E_f by making the substitution

$$E_f = \langle v_\perp^2 P(v_z) e^{-z/(v_z\tau)}\rangle \tag{21}$$

($P(v_z)$ is a polynomial in v_z to be determined), which leads to a solution of the type $E_f(z) \sim (k_0 l)^2$, which is a negligible quantity in the calculation of $E(z)$. This justifies the assumption made that the contribution of E_f to the formation of $\psi_1(0)$ is insignificant. However, when expression (21) is substituted into the total field, which satisfies boundary condition (10), the derivative dE_f/dz is now linear in $(k_0 l)$, and it must be taken into account in finding $\mathbf{E}_k$. For $z=0$ the integrals (21) are easily evaluated, and the final result can be expressed as follows:

$$\mathbf{E}(0) = \mathbf{E}_0(0) + \mathbf{E}_\Lambda(0) + \mathbf{E}_k(0).$$

The field $\mathbf{E}_0(0)$ of the zeroth approximation has the form

$$E_{0\alpha} = -\frac{k_0^2 q^2}{[1+(\Omega\tau)^2]D} b_{\alpha\beta} E_{u\beta}(0),$$

$$\mathbf{E}_u = \mathbf{u}_{ST} + \mathbf{u}_{ind}, \quad b_{\alpha\beta} = \begin{pmatrix} \dfrac{q^2+k_0^2}{q^2} & \Omega\tau \\ -\Omega\tau & \dfrac{q^2+k_0^2}{q^2} \end{pmatrix}, \tag{22}$$

$$D = \left(q^2 + \frac{k_0^2}{1+(\Omega\tau)^2}\right)^2 + \left(\frac{k_0^2}{1+(\Omega\tau)^2}\right)^2(\Omega\tau)^2.$$

The deformation correction $\mathbf{E}_\Lambda(0)$ looks like

$$\begin{Bmatrix} E_{\Lambda x}(0) \\ E_{\Lambda y(0)} \end{Bmatrix} = -\frac{i}{5}\frac{k_0^2 q^2}{(1+(\Omega\tau)^2)D}\frac{v_F}{s}(ql)E_{ux}(0)$$

$$\times \begin{Bmatrix} 1 - \dfrac{2q^2+k_0^2}{q^2(1+(\Omega\tau)^2)} \\ \Omega\tau\dfrac{2q^2+k_0^2}{q^2(1+(\Omega\tau)^2)} \end{Bmatrix}. \tag{23}$$

When the diffuseness of the boundary is taken into account, one obtains the correction

$$E_{k\alpha}(0) = \frac{3}{32}(k_0 l)\left(\frac{k_0}{k_1}+\frac{k_0}{k_2}\right)a_{\alpha\beta}(E_{0\beta}+E_{u\beta}), \tag{24}$$

which is close to the corresponding result obtained in an analysis of the influence of weak nonlocality on the surface impedance of a metal.[7]

Thus in the leading approximation, as before, the electric field at the interface is determined exclusively by the external fields coupled to the elastic wave, and the skin effect does not contribute to $\mathbf{E}(0)$.

The most significant correction is due to the deformation interaction, which has a more stringent condition for negligibility: $ql < s/v_F$.

Diffuse scattering at the interface gives rise to a skin component of the electric field, the contribution of which can almost always be neglected.

Let us estimate the component j_x of the total current. In the leading approximation it is given by

$$j_x = -\frac{k_0^2 q^2 \sigma_0}{(1+(\Omega\tau)^2)^2 D}\left[\frac{q^2+k_0^2}{q^2}u_{ST} - (\Omega\tau)u_{ind}\right]$$

$$+\frac{\sigma_0}{1+(\Omega\tau)^2}[u_{ST} - (\Omega\tau)u_{ind}]. \tag{25}$$

In weak fields ($\Omega\tau \ll 1$) for $\Omega\tau \ll \omega/\Omega$ the main contribution to the current is given by the inertial component, and $j_x \approx [q^2/(q^2+k_0^2)]i\omega\tau j_{ion} \ll j_{ion}$. In principle it is also possible to have the regime $\omega/\Omega \ll \Omega\tau \ll 1$, in which j_x is now determined by the induction field, remaining small as before ($j_x \approx (\Omega\tau)^2 j_{ion} \ll j_{ion}$). Thus in the low-field limit the electron current always compensates the ion current almost completely (the regime of current neutrality), and the amplitudes of the electron and elastic displacements are equal. The transfer of the corresponding momentum from the lattice to the electrons occurs on account of frequent collisions of the latter with impurities.

In a high field ($\Omega\tau \gg 1$) it follows from (22) and (25) that $j_x \approx j_{ion}$, i.e., the electrons are no longer dragged by the lattice. As a consequence of this, only the H-independent component E_{0x}, due to the flow of uncompensated ion current, remains in Eq. (22), while the E_{0y} component vanishes. Actually, this conclusion may be invalid, and in order to obtain a correct answer one must solve a two(three)-dimensional problem. Indeed, consider a metal slab bounded on both sides in the x direction, with an elastic wave filling the entire cross section. This elastic wave creates a relief of both the ion and electron displacements on the opposite faces of the slab. It might be thought that charge neutrality is ensured in this case by surface currents flowing on the lateral faces. However, if it is taken into account that the elastic strain appears on the end of the slab at some definite time (turn-on), then it is clear that in this case charge neutrality can be ensured only by the flow of electrons from one face of the slab to the other and the corresponding compensation (partial or total) of the ion current in the entire volume. In the case of a sound beam of finite extent in a sample of large cross section, regions of compression (rarefaction) will arise at the boundaries of the beam, and charge neutrality at these boundaries will be ensured by Coulomb forces. The author is unaware of any solution of this problem, and it is therefore unclear whether current neutrality can actually be violated. In any case, there has been no mention in the literature of any observation of the decrease implied by (22) in the efficiency of interconversion of elastic and electromagnetic oscillations in the limit of high magnetic fields.

Let us summarize the analysis of this Section. In the local limit in low fields Eq. (11) gives a rather good description of the induction component of the electromagnetic wave emitted by an elastic wave. As to the inertial component, two remarks are in order:

1. As we have said, the relative smallness of $\mathbf{u}_{ST}$ makes possible a regime in which the main contribution to $E_x(0)$, even in low fields, is given by the induction component.

Moreover, under real experimental conditions, when the dimensions of the receiving antenna are comparable to the transverse dimension of the sound beam, the contribution of $\mathbf{u}_{ind}$ to $E_x(0)$, owing to edge effects, can be decisive even in lower fields. Actually no difficulties arise here, since the fact that $\mathbf{u}_{ind}$ is odd in H always permits one to separate out the contribution of $\mathbf{u}_{ST}$ in pure form by taking the average of the results of measurements for opposite values of the fields.

2. It should be understood that even in the case $ql \sim 10^{-2}$ the contribution of the deformation correction to the inertial component can be quite large. It can be estimated experimentally in the following way. Summing (22) and (23) for $\Omega\tau \ll 1$, we obtain

$$E_x(0) \approx -\frac{k_0^2}{q^2+k_0^2}u_{ST}\left(1-\frac{i}{5}\frac{v_F}{s}ql\right).$$

Let the receiving antenna be oriented at an angle of $45°$ to $\mathbf{u}$ so that both the inertial and Hall components can be received with equal weight. Since the latter, in the leading approximation, has the form

$$E_y(0) = \frac{k_0^2}{q^2+k_0^2}\frac{i\omega}{c}Hu,$$

it is clear that their interference will lead to an asymmetry of the field dependence of the amplitude of the total signal with respect to $H=0$. The value of H about which the amplitude is symmetric determines the value of the deformation correction.

In our further discussion we shall make essential use of current neutrality. For $\Omega\tau \ll 1$ the correctness of this assumption is completely confirmed by the analysis. For $\Omega\tau \gtrsim 1$ there is at present no rigorous proof of the possibility (or impossibility) of realizing such a regime, and we shall therefore restrict the following discussion to the case of $\Omega\tau \ll 1$.

2. MIXED STATE

Unfortunately, at present there is no theoretical scheme, similar to the method of the kinetic equation, that would permit a rigorous calculation of the current in the mixed state. Usually the continuum approximation and the two-fluid model are used. In the continuum approximation the spatially homogeneous magnetic structure of the mixed phase is ignored, and the induction in the sample is assumed equal to the average value of B, which even for a small excess above H_{c1} can be assumed to coincide with the applied field. The equivalent circuit of a superconductor in the two-fluid model is a superconducting and a normal channel connected in parallel. The conductivity of the normal channel is expressed by the standard relation

$$\sigma_s^n = \frac{n_n e^2 \tau}{m},$$

where n_n is the density of the normal component. In the superconducting channel we should replace τ by $(i\omega)^{-1}$ (we have in mind an ac current) and use the density n_s of the superfluid component,

$$\sigma_s^s = \frac{n_s e^2}{mi\omega}.$$

In calculating the total current, which appears in Eq. (3), we must add to it the current generated by the moving vortex lattice and also take into account the specific features of the manifestation of the Hall effect in a superconductor.[8] As a result, Eq. (3) takes the form

$$\frac{d^2\mathbf{E}}{dz^2} = \frac{4\pi i\omega}{c^2}\mathbf{j} = k_s^2\left(\mathbf{E}+\mathbf{u}_{ST}+\frac{i\omega}{c}[\mathbf{t}\times\mathbf{B}]\right)$$
$$+k_{ns}^2\frac{i\omega}{c}[(\mathbf{u}-\mathbf{t})[\mathbf{t}\times\mathbf{B}]\mathbf{B}]. \quad (26)$$

Here we have introduced the notation

$$k_{ns}^2 = \frac{4\pi i\omega\sigma_s^n}{c^2}, \quad k_L^2 = \frac{4\pi i\omega\sigma_s^s}{c^2} \equiv \frac{1}{\delta_L^2}$$

($\delta_L(T,B)$ is the London penetration depth), $k_s^2 = k_{ns}^2 + k_L^2$, and $\mathbf{t}$ is the displacement of the vortex lattice.

Equation (26) is the main result of this paper. Let us give a brief explanation. The Maxwellian field $\mathbf{E}$ and the inertial field $\mathbf{u}_{ST}$ act on both the superconducting and normal channels. In a reference frame moving along with the vortex lattice at velocity $\dot{\mathbf{t}}$ there is a magnetic field $\mathbf{B}$, which in the laboratory frame corresponds to an electric field $\tilde{\mathbf{E}} = (1/c)\times[\mathbf{B}\times\dot{\mathbf{t}}]$. Physically $e\tilde{\mathbf{E}}$ is the momentum lost by the electrons in the motion of the vortex lattice,[9] and therefore the field $\tilde{\mathbf{E}}$ enters Eq. (26) with the opposite sign. In the Hall component [the last term in (26)] in the regime of current neutrality, $(\dot{\mathbf{u}}-\dot{\mathbf{t}})$ is the relative velocity of the electrons and the source of the magnetic field. As was shown in Ref. 8, the Hall current in a superconductor can only be due to normal excitations. The physical meaning of this statement is that in the case of s pairing the energy gap does not permit the Lorentz force to "pull apart" the electrons of a pair in opposite directions. It can be supposed that for a different symmetry of the order parameter the form of the Hall component will be different.

Relation (26) is written without the deformation correction to the current. If it is necessary to take this correction into account, it will look like (23) with k_0^2 replaced by k_{ns}^2.

We rewrite Eq. (26) in the form

$$\frac{d^2\mathbf{E}}{dz^2} = k_s^2(\mathbf{E}+\mathbf{u}_{ST})+k_L^2\frac{i\omega}{c}[\mathbf{t}\times\mathbf{B}]+k_{ns}^2\frac{i\omega}{c}[\mathbf{u}\times\mathbf{B}]. \quad (27)$$

It is clear that Eq. (27) correctly describes the transition to the normal phase [$k_L=0$, $k_s=k_{ns}=k_0$, and Eq. (27) goes over to (9)]. Equation (27) must be supplemented with the equation of motion of the vortex lattice. The latter is acted on by the following forces: electrodynamic, $\mathbf{f}_{ed} = (1/c)[\mathbf{j}\times\mathbf{B}]$, a pinning force $\mathbf{f}_p = \alpha_L(\mathbf{u}-\mathbf{t})$ (α_L is the Labusch "spring" parameter), the frictional force $\mathbf{f}_f$, and the Magnus force.[10] The last of these can be neglected in the regime $\Omega\tau \ll 1$. The force of friction is proportional to the velocity of the vortex lattice relative to the medium creating the friction. The physical nature of the friction is not completely clear at present. It was noted in Ref. 11 that the friction cannot be due to the superfluid component, since in that case it would be completely impossible for an undamped current to flow in the Shubnikov phase. There are two other subsystems that could lead to friction: the lattice and the normal electrons, which are con-

centrated mainly in the cores of the vortices. Since in the current-compensation regime both of these subsystems have velocity $\dot{\mathbf{u}}$, we write the force of friction as $\mathbf{f}_f = i\omega\eta(\mathbf{u}-\mathbf{t})$, unlike the form used in Ref. 3.

If, as usual, we neglect the mass of the vortex, the equation of motion of the lattice will have the form

$$\frac{c}{4\pi i\omega}\left[\frac{d^2\mathbf{E}}{dz^2}\times\mathbf{B}\right]+\alpha^*(\mathbf{u}-\mathbf{t})=0, \tag{28}$$

where $\alpha^*=i\omega\eta+\alpha_L$.

Sometimes instead of the electrodynamic force, Eq. (28) is written in terms of the elastic force accompanying the deformation of the vortex lattice (in our case $C_{44}(d^2\mathbf{t}/dz^2)$, where $C_{44}=B^2/4\pi$ is the bending modulus of the vortex lattice).[3] However, the elastic modulus of the vortex lattice is determined by only that part of the total current which is generated by the deformable vortex lattice itself, and therefore upon such a replacement Eq. (28) should still contain the component of the electrodynamic force generated by the extraneous currents. It is therefore preferable to write the equation of motion of the vortex lattice in the form (28), since all of the currents are automatically taken into account.

The boundary condition on system (27), (28) is the previous condition (2) for the Maxwellian field. In principle the vortex lattice also exerts an additional force on the interface, so that system (27), (28) should be supplemented by a boundary condition expressing the absence of stress on the boundary:

$$\rho s^2\frac{du}{dz}-\alpha^*\int_{-\infty}^{0}(u-t)dz=0. \tag{29}$$

It is readily seen that the corrections due to (29) are of order $B^2/(4\pi\rho s^2)$, and for reasonable fields attainable at the present time they can be neglected, i.e., we can, as before, use the condition $\mathbf{u}'(0)=0$.

The further solution of system (27), (28) with boundary condition (2) does not present any difficulty. The results have the form

$$E_x(0,B)=-u_{ST}\frac{k_s^2}{q^2+k_s^2}\frac{\alpha^*}{\alpha^*+q^2\frac{B^2}{4\pi}\frac{k_L^2}{q^2+k_s^2}}, \tag{30}$$

$$E_y(0,B)=-u_{\mathrm{ind}}\frac{k_s^2}{q^2+k_s^2}\frac{\alpha^*}{\alpha^*+q^2\frac{B^2}{4\pi}\frac{k_L^2}{q^2+k_s^2}}. \tag{31}$$

We emphasize once again that the expressions obtained remain valid upon the transition to the normal state. Furthermore, for $B\leq 0.8H_{c2}$, when $k_s^2\approx k_L^2\gg q^2$, k_{ns}^2, Eq. (31) correlates with the result obtained in Ref. 3 (when allowance is made for the differences in the choice of f_f). The coefficient multiplying q^2 in the last term in (30) and (31) is practically the same as the wave-number-dependent bending modulus of the vortex lattice, C_{44}, obtained in Ref. 12. We also note that the effective penetration depth that follows from the solution of system (27), (28),

$$\lambda_{\mathrm{eff}}^2=\frac{1+k_L^2\frac{B^2}{4\pi\alpha^*}}{k_L^2+k_{ns}^2},$$

agrees exactly with the result obtained in Ref. 13.

Let us briefly discuss the informative power of the EM-FREW method for studying both the Meissner phase and the vortex lattice. We start with the inertial component $E_x(0,0)$. Because of its relatively small size, the question of investigating it, judging from the literature, has not been discussed before. However, an estimate shows that at a sound wave intensity of $\approx 10\,\mathrm{W/cm^2}$ and a frequency of $\approx 50\,\mathrm{MHz}$, $u_{ST}\approx 2\times 10^{-6}\,\mathrm{V/cm}$, which makes it entirely feasible to measure $E_x(0,0)$, and this is confirmed by preliminary experiments done by the author.

Relation (30) is also applicable to the Meissner state. Indeed, for $B\to H_{c1}$, as is shown below, the most slowly varying parameter is α^*, and therefore the last factor in Eq. (30) approaches 1, and the expression obtained for $E_x(0,0)$ in this case agrees with the result that can be obtained from a rigorous approach based on the kinetic equation for $T\ll T_c$ (Ref. 14):

$$E_x(0,0)=-u_{ST}\frac{k_s^2}{q^2+k_s^2}.$$

Thus the change of $E_x(0,0)$ with temperature at the transition through T_c is completely determined by the behavior of $k_s^2(T)$, which evolves from a purely imaginary k_0^2 to a real quantity δ_L^{-2}. Evidently, one always has

$$|k_0^2|\leq\delta_L^{-2}, \tag{32}$$

and therefore below T_c the modulus $|E_x(0,0)|$ increases, while the phase of the signal decreases. At one time, quite a few experiments were being done on the interconversion of elastic and electromagnetic oscillations in the absence of a magnetic bias field in superconductors.[15] However, those experiments were done on highly pure metals, in which the main contribution to $E_x(0,0)$ was from the deformation component, which freezes out at the superconducting transition. The behavior of the inertial component is diametrically opposite. The scale of the variation of $E_x(0,0)$ depends on where q^2 falls in relation to inequality (32). An experiment is not very informative if $q^2\ll|k_0^2|$— both the amplitude and the phase of the signal vary insignificantly on transition through T_c. The most favorable situation is for $|k_0^2|\ll q^2\leq\delta_L^{-2}$, in which case measurements of the inertial component can easily be used to recover the temperature dependence of $\delta_L(T)$, at least to temperatures for which the right-hand side of the latter inequality remains weak.

Let us now turn to the mixed phase. Using the estimate of the coefficient of friction η from Ref. 16, we write α^* in the form

$$\alpha^*=k_0^2\frac{BH_{c2}}{4\pi}+\alpha_L(B). \tag{33}$$

It follows from this equation that for $B\approx H_{c1}$ one has $|\alpha^*|\gg q^2 C_{44}$ for any value of the parameter α_L, and the last factor in Eqs. (30) and (31) does not affect the behavior of the radiated field. Thus in a low field the inertial component is constant, while the induction component appears for H

$>H_{c1}$ and grows linearly with applied field, with a slope $(\omega/c)[k_s^2 u/(q^2+k_s^2)]$. The phases of the two components are shifted relative to the corresponding signals in the normal state by an amount equal to $\arctan q^2\delta^2/2$. For strong pinning ($\alpha_L(B)\gg q^2 C_{44}$, as has been shown experimentally[2]) or $q^2\ll k_0^2$, this type of behavior persists to $B\sim H_{c2}$, when the rapid change of both k_L and $\alpha_L(B)$ comes into play. The information content of an experiment in this case is apparently small. The situation is completely different in the case of peak pinning with the simultaneous satisfaction of the opposite condition, $q^2>k_0^2$. In that case, for $B>B_\eta = (k_0^2/q^2)B_{c2}$ the elastic response of the vortex lattice exceeds the contribution of the force of friction, and the inertial component begins to decrease with increasing B as a consequence of the increase in the effective penetration depth. By measuring the change of the complex quantity $E_x(0,B)$ on the decaying part of the curve, one can recover the behavior of $\eta(B)$ and $\alpha_L(B)$ without making any preliminary assumptions. Here it is extremely important that $E_x(0,B)$ exists for $B=0$ and provides the necessary reference levels for both the amplitude and the phase.

For $B>B_\eta$ the Hall component should increase less rapidly and possibly go to saturation. In principle, the parameters of the vortex lattice should enter $E_x(0,B)$ and $E_y(0,B)$ in an analogous way, and the Hall component can also be used to recover the functions $\eta(B)$ and $\alpha_L(B)$. However, since the induction component vanishes exactly for $B=0$, the lack of a reliable reference level makes it preferable to make measurements of $E_x(0,B)$ at small B. At the same time, in the region of moderately high magnetic fields, in the case $q^2\gg k_0^2$, measurements of $E_x(0,B)$ can turn out to be difficult, and measurements of $E_y(0,B)$ can prove more informative.

When B approaches H_{c2} the evolution of $\mathbf{E}(0,B)$ begins to depend not only on the dynamics of the vortex lattice but also on the behavior of k_L and k_s. Generally speaking, the functional dependences of k_L and k_s near H_{c2} are known[17] and one can hope to recover the behavior of $\eta(B)$ and $\alpha_L(B)$ for $B\to H_{c2}$. In reality, however, the value of H_{c2} is often restricted not by the condition of overlap of the vortex cores, as is assumed in the theory, but by the so-called paramagnetic limit.[18] The functional dependence of k_L and k_{ns} near the paramagnetic limit is not yet known. Nevertheless, measurements of the amplitude and phase of the radiated field near H_{c2} can be used to recover the behavior of $\lambda_{\mathrm{eff}}(B)$.

The author thanks E. V. Bezuglyĭ and V. A. Shklovskiĭ for numerous fruitful discussions.

[*]E-mail: fil@ilt.kharkov.ua

[1] L. A. Vienneau and B. W. Maxfield, Phys. Rev. B **11**, 4339 (1975).

[2] H. Haneda and T. Ishiguro, Physica C **235–240**, 2076 (1994).

[3] D. Dominguez, L. Bulaevskii, B. Ivlev, M. Maley, and A. R. Bishop, Phys. Rev. B **51**, 15649 (1995).

[4] A. N. Vasil'ev and Yu. P. Gaĭdukov, Usp. Fiz. Nauk **141**, 431 (1983) [Sov. Phys. Usp. **26**, 952 (1983)].

[5] V. M. Kontorovich, Zh. Éksp. Teor. Fiz. **45**, 1638 (1963) [Sov. Phys. JETP **18**, 1125 (1964)].

[6] É. A. Kaner, V. L. Fal'ko, and L. P. Sal'nikova, Fiz. Nizk. Temp. **12**, 831 (1986) [Sov. J. Low Temp. Phys. **12**, 471 (1986)].

[7] V. I. Okulov and V. V. Ustinov, Fiz. Met. Metalloved. **41**, 231 (1976).

[8] P. B. Miller, Phys. Rev. **121**, 445 (1961).

[9] Y. B. Kim and M. J. Stephen, in *Superconductivity*, edited by R. D. Parks, New York, M. Dekker (1969), p. 1107.

[10] G. Blatter, M. V. Feigel'man, V. B. Geshkenbein, A. I. Larkin, and V. M. Vinokur, Rev. Mod. Phys. **66**, 1125 (1994).

[11] V. M. Vinokur, V. B. Geshkenbein, M. V. Feigel'man, and G. Blatter, Phys. Rev. Lett. **71**, 1242 (1993).

[12] E. H. Brandt, J. Low Temp. Phys. **26**, 709 (1977).

[13] M. W. Coffey and J. R. Clem, Phys. Rev. B **46**, 11757 (1992).

[14] E. V. Bezuglyĭ, Fiz. Nizk. Temp. **9**, 15 (1983) [Sov. J. Low Temp. Phys. **9**, 6 (1983)].

[15] R. H. Bidgood, M. J. Lee, and E. R. Dobbs, J. Phys. **7**, 1791 (1977).

[16] J. Bardeen and M. J. Stephen, Phys. Rev. **140**, A1197 (1965).

[17] K. Maki, in *Superconductivity*, edited by R. D. Parks, New York, M. Dekker (1969), p. 1035.

[18] A. M. Clogston, Phys. Rev. Lett. **9**, 266 (1962).

Translated by Steve Torstveit